BRNO UNIVERSITY OF TECHNOLOGY
VYSOKÉ UČENÍ TECHNICKÉ V BRNĚ

FACULTY OF MECHANICAL ENGINEERING
FAKULTA STROJNÍHO INŽENÝRSTVÍ

INSTITUTE OF SOLID MECHANICS, MECHATRONICS AND BIOMECHANICS
ÚSTAV MECHANIKY TĚLES, MECHATRONIKY A BIOMECHANIKY

COMPUTATIONAL MODELING OF THE INTERACTION OF FLOWING BLOOD WITH THE ARTERY TUBE WITH THE ATHEROMA
VÝPOČTOVÉ MODELOVÁNÍ INTERAKCE PROUDÍCÍ KRVE S TRUBICÍ TEPNY S ATEROMEM

MASTER'S THESIS
DIPLOMOVÁ PRÁCE

AUTHOR
AUTOR PRÁCE

Bc. Michal Freiwald

SUPERVISOR
VEDOUCÍ PRÁCE

Ing. Pavel Švancara, Ph.D.

BRNO 2021

BRNO UNIVERSITY OF TECHNOLOGY
FACULTY OF MECHANICAL ENGINEERING

Assignment Master's Thesis

Institut:	Institute of Solid Mechanics, Mechatronics and Biomechanics
Student:	**Bc. Michal Freiwald**
Degree programm:	Applied Sciences in Engineering
Branch:	Engineering Mechanics and Biomechanics
Supervisor:	**Ing. Pavel Švancara, Ph.D.**
Academic year:	2020/21

As provided for by the Act No. 111/98 Coll. on higher education institutions and the BUT Study and Examination Regulations, the director of the Institute hereby assigns the following topic of Master's Thesis:

Computational modeling of the interaction of flowing blood with the artery tube with the atheroma

Brief Description:

Rupture of a sclerotic plaque in the carotid artery is one of the common causes of stroke. The analysis of stress–strain states of an atheroma artery thus has great potential for clinical practice. The aim of this work is to create a computational model of the interaction of flowing blood as a non–Newtonian fluid with a flexible artery tube containing an atherosclerotic plaque using the finite element method. Further analyze the influence of selected parameters on arterial stress and deformation.

Master's Thesis goals:

1) Based on the literature, provide a brief overview of current approaches in computational modeling of blood flow in the carotid artery with atheroma.
2) Creation of a geometry model of an idealized carotid artery with an atherosclerotic plaque.
3) Simulation of the interaction of flowing blood with a flexible artery tube containing an atherosclerotic plaque.
4) Analysis of the influence of selected parameters on arterial stress and deformation.

Recommended bibliography:

HOSKINS P. R., P. V. LAWFORD a B. J. DOYLE. Cardiovascular Biomechanics. Springer International Publishing AG, 2017. ISBN 3319464051.

BURŠA, J. Biomechanika srdečně-cévní soustavy. Elektronické studijní opory VUT v Brně.

ZIENKIEWICZ, O.C. a R.L. TAYLOR. The Finite Element Method. Oxford: Butterwoth-Heineman, 2011. ISBN 1856176304.

Deadline for submission Master's Thesis is given by the Schedule of the Academic year 2020/21

In Brno,

L. S.

prof. Ing. Jindřich Petruška, CSc. Director of the Institute	doc. Ing. Jaroslav Katolický, Ph.D. FME dean

FREIWALD, Michal. *Computational modeling of the interaction of flowing blood with the artery tube with the atheroma* [online]. Brno, 2021. Available from: https://www.vutbr.cz/studenti/zav-prace/detail/132762. Master's Thesis. Brno University of Technology, Faculty of Mechanical Engineering, Institute of Solid Mechanics, Mechatronics and Biomechanics. 83 pages. Supervisor Pavel Švancara.

I declare that I have written the thesis *Computational modeling of the interaction of flowing blood with the artery tube with the atheroma* on my own, under the supervision of Ing. Pavel Švancara, Ph.D., using the sources listed in bibliography.

Brno, June 2021 Bc. Michal Freiwald

I would like to express my sincere gratitude towards my supervisor, Ing. Pavel Švancara, Ph.D., for his empathetic approach, frequent consultations, and countless advice on problems regarding fluid-structure interaction theory, during the writing of this thesis.

I would also like to thank my parents for their continuous support and enthusiasm during my university studies, as this thesis would not have been possible without their help.

Bc. Michal Freiwald

Abstract

This master's thesis deals with the interaction between flowing blood and an atherosclerotic carotid artery using a finite element fluid-structure interaction analysis. In the first part, a summarized theoretical background is introduced, consisting of cardiovascular system, blood vessels, corresponding constitutive models, blood rheology, and fluid flow theory. Next, a brief summary of the current state of computational modeling in this area is provided, mainly focusing on structural and fluid-structure interaction analyses, and the types of constitutive models used. Experimental part focuses on the creation of a simplified model of the internal carotid artery with an atherosclerotic plaque, and a corresponding model of blood in this artery. Both models are afterwards used to perform a fluid-structure interaction analysis to understand the consequences of a pulsatile blood flow on the artery wall and atherosclerotic plaque growth; primary characteristics of interest are the first maximum principal stress on the artery wall and its deformation, wall shear stress and its corresponding time-averaged value, and oscillatory shear index. All results are compared across several different analysis types, to assess the differences and impact of a chosen approach. A simplified parametric study is also performed, to determine the impact of the stenosis percentage on resulting characteristics. Lastly, results, limitations of this thesis, and possibilities of further research are discussed.

Keywords

Atherosclerosis, atherosclerotic plaque, internal carotid artery, FSI analysis, finite element method, computational modeling

Rozšířený abstrakt

Předložená diplomová práce se zabývá interakcí proudící krve s tepnou obsahující aterosklerotický plát a veličinami, které jsou pro posuzování těchto patologických dějů klíčové.

Rešeršní část této práce nejprve pojednává o kardiovaskulárním systému jako celku a poté se podrobněji zaobírá cévami a krví, které jsou pro tuto práci nejpodstatnější. Je pojednáno o anatomii, struktuře a detailnějším složení tepen, jakožto i o nemocech, které jsou pro cévy nejvýznačnější. Dále je v práci uveden úvod do teorie konečných deformací, která je základem pro tvorbu konstitutivních modelů, jež tvoří nedílnou součást výpočtového modelování lidských tkání. To je hlavně z toho důvodu, že lidské tkáně jakožto materiál jsou hyperelastické, čímž se vymykají klasickým inženýrským materiálům, a tudíž není možné je popisovat pomocí klasických inženýrských charakteristik. Práce tedy po definování hyperelastického materiálu uvádí přehled konstitutivních modelů, které lze pro popis tohoto chování využít. Z důvodu rozsáhlosti problematiky konstitutivních modelů uvádí práce pouze stručný přehled, který je pro postup zvolený v této práci nutný. Dále se rešeršní část zabývá principem vzniku pulzní tlakové vlny ze srdce, složením krve a popisem nenewtonských kapalin, do kterých krev spadá. Stručně je zde poreferováno o některých charakteristikách, kterými se krev vyznačuje, jako je například viskoelasticita, mez kluzu, nebo pseudoplasticita. Dále je také pojednáno o různých modelech, kterými lze modelování krve matematicky popsat. V poslední části teoretické sekce je stručně pojednáno o teorii proudění a o základních zákonech, které zkoumají pulzační proudění.

Následující kapitola pojednává o současném stavu výpočtového modelování tepen s aterosklerotickým plátem. Jelikož si tato práce dává za cíl řešit tento problém jako interakci tuhé aterosklerotické krční tepny s pulzující krví, je v této části kladen důraz na práce obdobného typu, zejména z hlediska typu řešené tepny a použité výpočtové metody.

Výpočtová část této práce je členěna do několika podsekcí. Nejprve je vytvořen idealizovaný model tepny obsahující aterosklerotický plát, v souladu s rozměry, které udává literatura; analogický je také vytvořen model krve. Oba modely jsou nejprve řešeny separátně, primárně z důvodu velkých nelinearit a problémů s konvergencí výpočtů. Okrajovými podmínkami strukturální analýzy jsou povolené radiální posuvy na koncích modelu, umožňující nafukování, a statický tlak na vnitřní ploše modelu, odpovídající maximálnímu systolickému tlaku krve. Tepna je modelována jako izotropní hyperelastický materiál, pomocí konstitutivního modelu Yeoh, s hodnotami převzatými z literatury. Okrajovými podmínkami fluidní analýzy jsou poté tlaková vlna na jedné straně modelu, a hmotnostní průtok krve na straně druhé. Tyto hodnoty jsou převzaty z literatury a představují dva po sobě jdoucí srdeční cykly. Z důvodu nestability modelů a problémů s konvergencí při interakční analýze obsahují obě okrajové podmínky jistou formu náběhu, která modelu napomáhá v prvotních fázích výpočtů. Chování krve je simulováno pomocí modelu Carreau, s hodnotami převzatými z literatury. Na obou modelech je také provedena citlivostní analýza vlivu hustoty konečnoprvkové sítě na výsledky, tak aby byly hodnocené veličiny co nejméně ovlivněny nepřesně zvolenou sítí. Po nastavení strukturní i fluidní domény jsou oba modely propojeny a řešeny pomocí fluid-structure interaction (FSI) analýzy; nejprve pomocí jednosměrného a posléze pomocí obousměrného řešiče; v tomto případě již tepna není zatížena statickým tlakem, ale přebírá hodnoty z fluidního řešiče. Další část práce je věnována výsledkům, kterými jsou konkrétně: první hlavní napětí na stěně tepny, celková deformace tepny, smykové napětí na stěně (WSS) a jeho zprůměrovaná hodnota přes jeden srdeční cyklus (TAWSS) a oscilační index (OSI). Tyto veličiny jsou zvoleny z důvodu největší relevance v otázce růstu aterosklerotického plátu a ruptury aterosklerotické tepny. Z důvodu nemalého počtu zjednodušení, které jsou v práci diskutovány, je místo porovnání

získaných veličin vůči mezním hodnotám, uvedeným v literatuře, kladen primární důraz na porovnání samostatné strukturální/fluidní analýzy s jednostrannou a oboustrannou FSI analýzou, které jsou výpočtově řádově náročnější. Výsledky ukazují, že rozdíly u všech hledaných veličin jsou při strukturální/fluidní analýze a jednostranné FSI analýze nezanedbatelné oproti oboustranné FSI analýze, která je v práci považována za referenční, jelikož bere v potaz jak ovlivnění stěny tepny krví, tak ovlivnění krve stěnou tepny.

Poslední část práce diskutuje vliv změny velikosti aterosklerotického plátu na hodnoty a rozložení charakteristických veličin. Ačkoliv z důvodů komplexnosti úlohy a časové náročnosti FSI analýz pravděpodobně nelze ze získaných porovnávacích výsledků vyvozovat plně reprezentativní závěry (práce parametrizuje pouze jednu z rozměrových veličin a pouze v několika málo případech), dává parametrická část práce určitou představu o změně daných hledaných veličin v závislosti na růstu aterosklerotického plátu. V závěru jsou diskutovány výsledky práce, její limitace a možnosti dalšího výzkumu v této oblasti.

Klíčová slova

Ateroskleróza, aterosklerotický plát, krční tepna, FSI analýza, metoda konečných prvků, výpočtové modelování

Content

1 Introduction

1.1 Motivation

Heart is one of the most important, if not the most important, organs in the human organism. Its function is to distribute oxygenated blood throughout the human body which is absolutely crucial to its proper functioning. In order to do that, a complex system of arteries and veins spreads across the entire human system, delivering oxygen to every last call that needs it, primarily to create ATP (adenosine triphosphate - a molecule that carries energy). Any damage to this vascular system poses a significant threat to our health, which is why understanding vein and arteria related issues is a subject to research that is beyond necessary.

One of the main risks regarding vascular system function is the build-up of fats, cholesterol, and other substances in the artery wall, creating a plaque which causes restriction to a proper blood flow. As the plaque builds up, it is more and more difficult for blood to maintain its flow in the artery, resulting in increase of generated stresses in the plaque itself. As the plaque grows further, it can either clog the entire artery or burst and drift off to other parts of the body, eventually getting stuck elsewhere; either way, it eventually cuts off a certain part of our body from the much-needed oxygen. If the affected artery happens to supply either the brain or the heart, this cut-off results in either a stroke or a heart attack, both of which pose a serious health risk.

Computational modeling of vessels with atherosclerotic plaque and their interaction with blood is rather difficult. Vessels and atherosclerotic plaques contain several different layers, each of which behaves in a different manner. To properly model them, we have to first acquire experimental data and fit them to some of the known constitutive models. This data is, unfortunately, quite inconsistent, due to the nature of biological tissue; factors such as age, location within the body, or degree of plaque calcification have to be considered. Blood, on the other hand, is a fluid consisting of several different components (the ratio of which also varies), the properties of which change in accordance with temperature, age, or blood flow rate. Properly combining these two elements requires a lot of computational power and even then, is highly patient-specific.

1.2 Problem Formulation and Thesis Objectives

Rupture of atherosclerotic plaque in the carotid artery is one of the most common causes for cerebrovascular accident (CVA, stroke). If we understand all the factors, contributing to the build-up of atherosclerotic plaques, we can successfully predict them, and maybe even find new possible ways to prevent them. This is why performing and improving these types of analyses, finding negligible and high-importance factors, and generalizing result conclusions are today's goals in this field of research.

Problem formulation, resulting from the previous paragraph, is then: ***"Creation of an idealized computational model of a vessel with an atherosclerotic plaque and simulation of the interaction of flowing blood with this flexible artery tube."***

After taking all the elements, related to the aforementioned fluid-structure interaction analysis (FSI), into consideration, the following thesis objectives were determined:

- Research study of the human heart, circulatory system, blood, and vessels with their material models and diseases
- Brief overview of current approaches in computational modeling of blood flow in the carotid artery with atheroma
- Creation of a geometry model of an idealized carotid artery with an atherosclerotic plaque
- Simulation of the interaction of flowing blood with a flexible artery tube containing an atherosclerotic plaque
- Analysis of selected parameters on the influence on arterial stress and deformation

1.3 Substantial Factors and Method Chosen for Solution

In order for the simulation to be realistic, we must first identify the substantial factors which influence the results of an FSI analysis. All the necessary factors will be described in greater detail throughout the thesis, this section contains just a simple overview, and was created based on [1]:

Surroundings of the Component

All vessels are located within the human body and are surrounded by other components. For the purposes of this thesis, though, these will not be considered, and the system will only be represented by the artery tube and blood.

Geometry and Topology of the Component

For the purposes of this thesis, both geometry and topology of the components will be represented by a three-dimensional computer-aided model with idealized parameters.

Mates of the Component

Since this is a fluid-structure interaction analysis, blood, deformed due to the pressure and mass flow applied to it, will interact with the artery wall, and vice versa.

Loads Acting on the Component

Pressure data will be applied on the inlet of the blood model and mass flow data on the outlet, which will deform it and result in generation of stresses in the artery wall.

Properties of the Component

Since vessels contain multiple layers and their materials are rather complex, all layers will be modelled using their individual hyperelastic material models with blood being modelled as a non-Newtonian incompressible fluid.

Method Chosen for Solution

Due to the nature of hyperelastic material models and their interaction nature with non-Newtonian fluids, this problem cannot be solved analytically. Therefore, Finite Element Method (FEM) and Finite Volume Method (FVM) will be applied to solve this problem.

2 Theoretical Part

2.1 Cardiovascular System

Cardiovascular system consists of the heart and blood vessels, and its main purpose is to transport oxygen, nutrients, and byproducts of our metabolism throughout the body. When describing this system, we can distinguish between pulmonary and systemic circulation. Pulmonary circulation is the transportation of de-oxygenated blood from the heart to the lungs, where it is re-saturated prior to being dispersed back into the system. Systemic circulation then represents the movement of blood from the heart through the body to provide the much-needed oxygen and nutrients to wherever necessary [2]. Both of these systems combined can be seen in Figure 1.

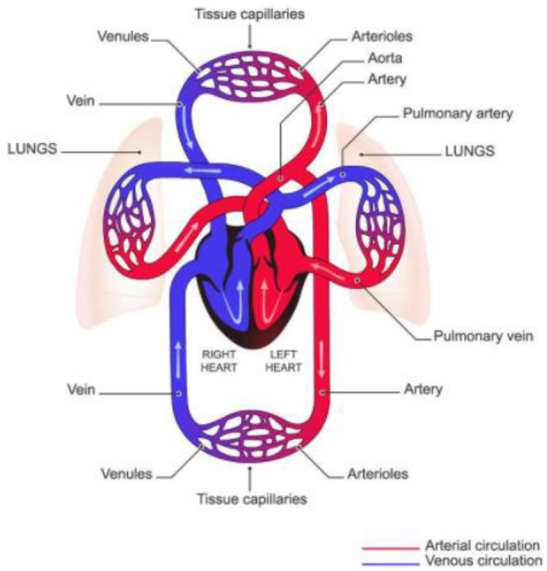

Figure 1 - Cardiovascular system [2]

2.1.1 Heart

Heart (*myocardium*) is a transversely striped muscle organ, and it is the core of our cardiovascular system. It is stored in a double-membraned sac (*pericardium*) consisting of a double-serous (inner) layer and a fibrous (outer) layer, both of them being separated by a subtle layer of pericardial cavity filled with fluid. The purpose of pericardium is to shield heart against other organs and allows for fluid movement of sac surfaces during the heart cycle. Heart is divided into two main parts – left and right, both of which are further separated into atrium and ventricle [3] [4].

Atria are parts of the heart where blood enters it from veins, while atrium further ousts it to ventricles. The walls of atria are thinner than the ones of ventricles, due to lower pressure present in atria. Ventricles then further disperse blood outside the heart, either to lungs to re-saturate, or to the entire system to deliver oxygen. Both atria and ventricles are separated by atrioventricular valves that prevent the backflow of blood [5]. Heart scheme is displayed in Figure 2.

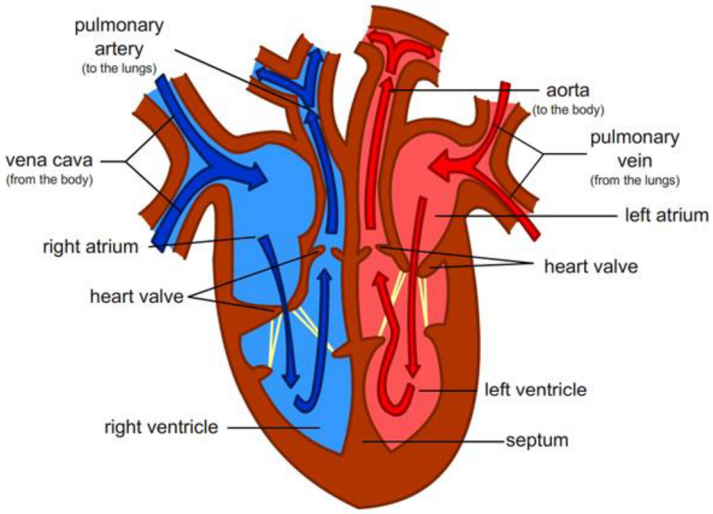

Figure 2 - Heart scheme [67]

2.1.2 Heart Cycle

Heart cycle is a repetitive heart function that can be simplified to a single contraction of the heart muscle (*systole*) and its relaxation (*diastole*). The result of this process is a certain volume of oxygenated blood being forced to the systemic circulation and approximately the same volume of de-oxygenated blood to the pulmonary circulation. During the diastole, atria and ventricles are relaxed and the atrioventricular valves are open. As an impact of this, oxygen-depleted blood from the body enters right atrium, and proceeds to right ventricle via atrioventricular valve. At the same time, oxygenated blood from pulmonary veins enters left atrium, and proceeds to left ventricle via atrioventricular valve. During the systole, the walls of ventricles contract, atrioventricular valves close, and both oxygen-depleted and oxygenated blood is forced out of the heart, either to pulmonary veins to re-oxygenate, or to systemic veins to deliver oxygen [4] [5]. This process is shown in Figure 3.

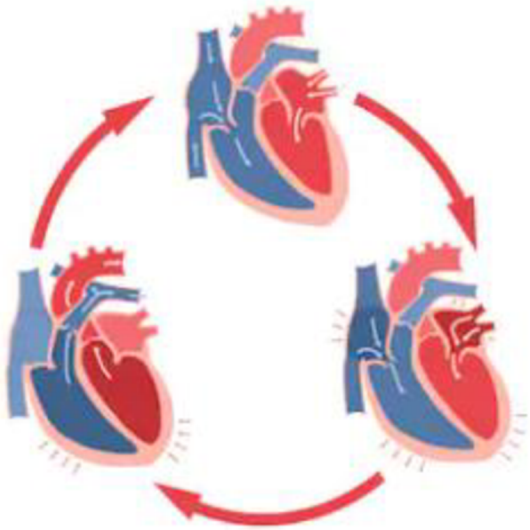

Figure 3 - Heart cycle [67]

2.1.3 Electrical System of the Heart

Electric impulses which cause the systole and diastole to contract are called the Electrical Heart System. It is a specialized part of the heart muscle, the cells of which have the ability to create and propagate impulses, due to special membrane properties of the cells involved, and their resting voltage and action potential. Without these impulses, the heart would be unable to function, and the blood flow would cease [5].

The electrical signal starts in the sinoartial node (SA), which causes atria to contract. As the impulse propagates, it reaches the atrioventricular node (AV). This node then sends the signal to ventricles, causing them to contract, and the whole cycle repeats. Even though all parts of the heart electrical system have the ability to generate impulses, these impulses have slower frequency and are usually suppressed by the main SA signal. Only when the main SA node shows any instabilities do these secondary sources take over to preserve heart function [4] [5] [6]. Detailed scheme of this system is shown in Figure 4.

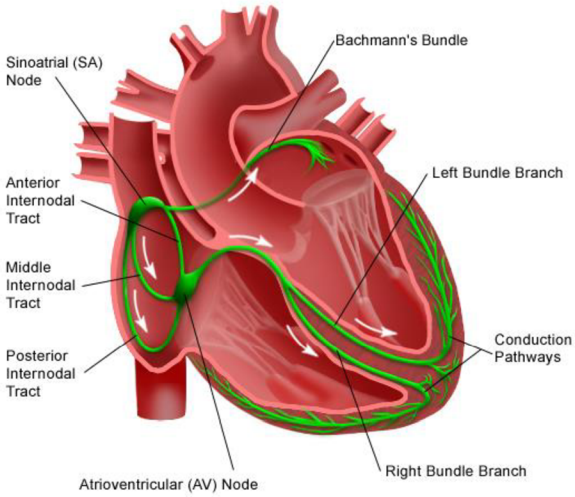

Figure 4 - Electrical Heart System [68]

2.1.4 Electrocardiography (ECG)

One of the most basic cardiology methods, based on scanning the heart muscle activity, is electrocardiography. It allows us to find any imperfections in the heart rhythm, ischemic changes, and other flaws. It is done by attaching several electrodes to the human body and recording individual heart cycles with them. The outcome of this activity is called Electrocardiogram (also ECG), displayed in Figure 5 [5].

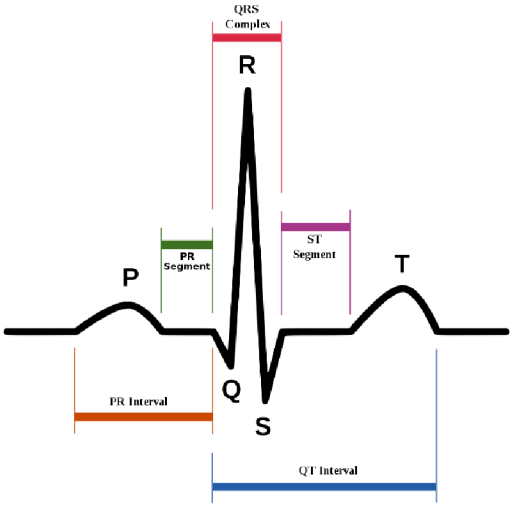

Figure 5 – Electrocardiogram [71]

2.2 Vessels

Blood vessels represent flexible tubes carrying blood, oxygen, and nutrients throughout the human body. Their main division is to arteries, veins, venules, and capillaries. All vessels are well adapted for the physiological purposes they engage in; for example, low-pressure arteries (pulmonary) have thinner walls then the high-pressure ones, so that the highest possible efficiency is achieved in every given sub-system [7] [8]. From this point on, this thesis will primarily focus only on arteries.

2.2.1 Arteries

The main function of arteries is to distribute oxygenated blood from the heart to peripheral parts of the human body. The largest artery, leading from the heart, is called Aorta, and has a radius of approximately 20mm. As we proceed further from the heart, this artery divides itself into smaller peripheral arteries which can be as small as 8-10μm (capillaries) [9]. Another dividing aspect of arteries is their mechanical composition; as a results of the heart physiology, oxygenated blood is leaving it in the form of a spasmodic flow, meaning that the Aorta first has to transform it into a continuous flow. Knowing this, we can divide arteries into elastic-type arteries and muscle-type arteries.

- **Elastic-type arteries** are the arteries closest to the heart. They contain the largest ratio of elastin, meaning that they can properly react to spasmodic flow with appropriate stretching and contracting, which helps absorb some of the flow energy and transform blood into a more continuous flow. Elastic-type arteries can stretch their walls up to 10% [10].
- **Muscle-type arteries** are arteries further from the heart, typically with a diameter of 0,3-1mm. Their walls mainly consist of smooth muscle and can stretch their walls up to 2-3% [10].

2.2.2 Artery Wall

When looking at the structural aspect of vessels (in this case, arteries), their walls mainly consist of three layers: *Tunica intima*, *Tunica media*, and *Tunica adventitia*. This means that the wall itself is a composite material where each of the layers differs both in individual components and their orientation, resulting in an anizotropic behavior of the wall [8]. Cross section of an artery is displayed in Figure 6.

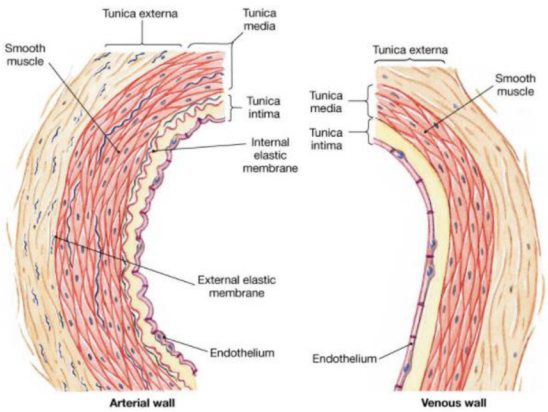

Figure 6 - Artery cross section [69]

2.2.2.1 Tunica Intima

Tunica intima is the innermost layer of blood vessels. It consists of a monolayer of endothelium flat cells, below which there is a sub-endothelium layer of sparse connective tissue with possible elements of smooth muscle. Thin elastic membrane (*elastica interna*) separates it from tunica media. It presents a smooth, non-thrombogenic interface between blood and contents of the arterial wall [11] [9] [8].

2.2.2.2 Tunica Media

Tunica media consists primarily of spiral smooth muscle cells embedded in a plexus of elastin, collagen, and proteoglycans. The closer an artery is to the heart, the more elastin it contains, making it more flexible. Elastin also causes media to carry more loads resulting from blood pulses. It is the thickest layer of the three and is separated from tunica adventitia by another thin elastic membrane (*elastica externa*) [11] [8] [12].

2.2.2.3 Tunica Adventitia

The outermost artery layer consisting of fibroblast and circumferentially oriented collagen. It is thought to serve as a protective sheath that prevents over-distension of media, and it is also where all vessel nerves and vasa vasorum run. Since this is the last layer, it is in direct contact with the surrounding tissue [11] [8].

All three layers can be seen in a histological vein cut in Figure 7, with layers from the top being: tunica intima, tunica media, tunica adventitia.

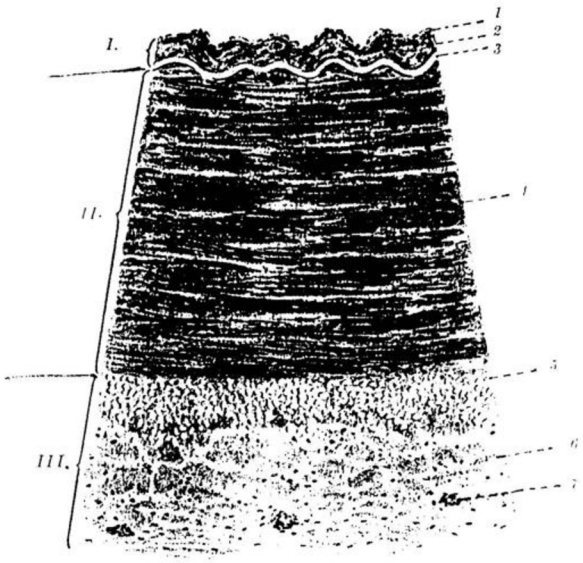

Figure 7 - Artery histological cut [11]

2.2.3 Structural Components of the Artery Wall

Structural components described in Chapters 2.2.1. and 2.2.2. have a great impact on the mechanical properties of such vessels. The components in question are collagen, elastin, and smooth muscle cells.

2.2.3.1 Collagen

Collagen is the most common protein in the human body. There are more than 20 known types of collagen, with type I and III being the most common in the artery wall. It can be found either in the form of multi-layer bundles or as single fibers, and is usually initially entangled within the vessel structure. Young's modulus of the basic collagen component (fibril) is up to $7\ GPa$, while a single collagen fiber (made out of these fibrils) has a Young's modulus of 1100MPa. However, the ductility of collagen can only reach 2-4%. Once straightened, collagen fibers carry most of the load resulting from blood flow in vessels [13] [11].

2.2.3.2 Elastin

Elastic is an elastomeric protein with great ductility (up to 70%) and low stiffness (in contrast to collagen). When a pulse wave passes through the vessel, elastin properties are used to define the shape of the stress-strain curve up until the moment when collagen fibers straighten and take over. As the human body ages, the concentration of elastin in human body decreases, making vessels stiffer. Axial tensile stress-strain dependency, showing the effect of collagen and elastin, is displayed in Figure 8. Both elastin and collagen are mainly located in tunica media [14] [13].

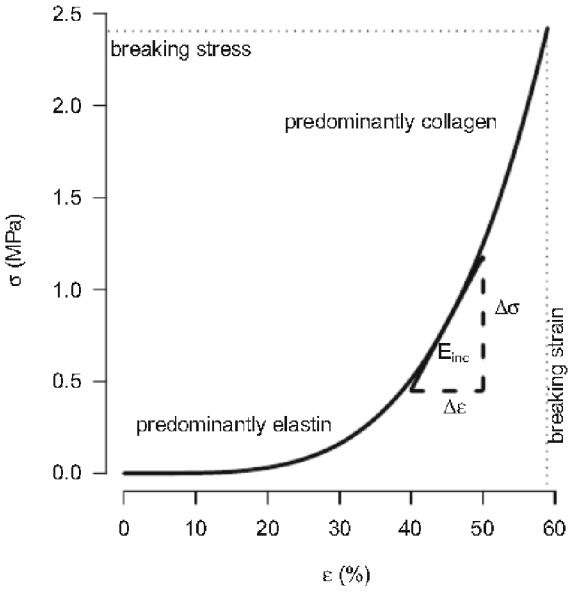

Figure 8 - Arterial wall stress-strain dependency [14]

2.2.3.3 *Smooth Muscle Cells*

Smooth muscle cells (SMC or VSMC) are what generally fills up the space between collagen and elastin. Smooth muscle is capable of contracting and relaxing, thus changing arterial wall stiffness; by 30% in the axial, and 40% in the circumferential direction. The ration of cells throughout the cardiovascular system also differs; the further from the heart vessels are, the more SMC they contain. With elastin depredating (as a result of aging), SMC also play a role in vessel calcification [12] [14]. The distribution of SMC in blood vessels and their shape can be seen in Figure 9.

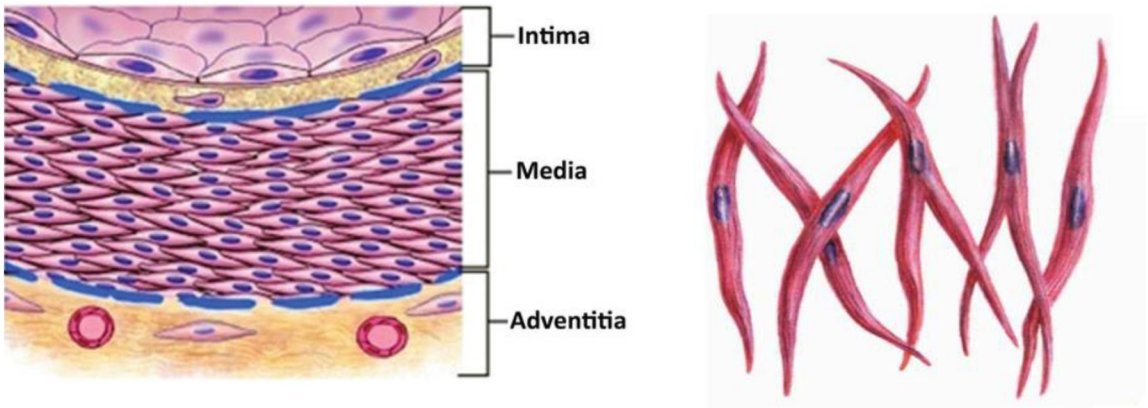

Figure 9 - SMC distribution in vessels, and their shape [12] [11]

2.2.4 Carotid Artery

As stated in the chapter *Thesis Objectives*, we will mainly focus on the carotid artery and its interaction with blood from now on. Carotid arteries, like all other arteries (except for capillaries) consist of three tissue layers: *tunica intima, tunica media, and tunica adventitia*. Common carotid arteries (CCA) are the major blood vessels in the neck, and they supply blood to the brain, neck, and face. We distinguish between two carotid arteries: one on each side of the body [15] [16]. As they progress into the neck, they each branch in bifurcations into two smaller arteries:

- Internal carotid artery (ICA), which supplies blood to the brain
- External carotid artery (ECA), which supplies blood to the face and neck [15]

This thesis will further deal only with an idealized model of the internal carotid artery (ICA), since it is the one supplying the brain. Picture of the carotid artery, its bifurcation, and location within the human body is displayed in Figure 10.

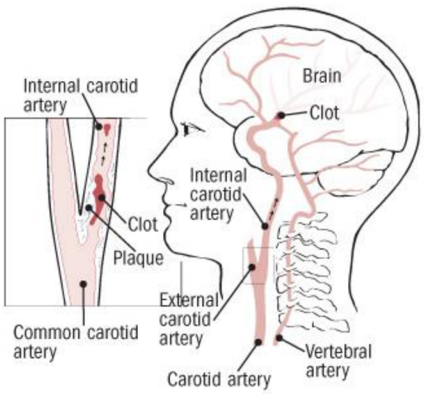

Figure 10 - Location of CCA within the body [16]

2.3 Vascular Diseases

Vascular diseases can be described as conditions which affect the proper functioning of our vessels. We can distinguish between blood vessels which distribute oxygenated and de-oxygenated blood throughout the body, and lymph vessels which make a separate system that rids our body of unwanted cells and liquids. For the purposes of this thesis, we will only further refer to the disorders of blood vessels. There is a variety of blood vessel related diseases and the following sub-chapters contain the most significant ones [17].

2.3.1 Aneurysm

Arterial aneurysm is defined as a focal dilation of a blood vessel with respect to the original artery. An aneurysm as it is, usually poses no imminent threat, and does not show any symptoms. The most common causes for an aneurysm to appear are high blood pressure, atherosclerosis, deep wounds, and infections. As the bulge grows, the vessel wall thickens, and the probability of rupture rises. Should the bulge burst, such events usually lead to life-threatening internal bleeding. The probability of a rupture is mostly influenced by age, smoking, sex, and even ethnicity. The most common types of aneurysms are displayed in Figure 11 [18].

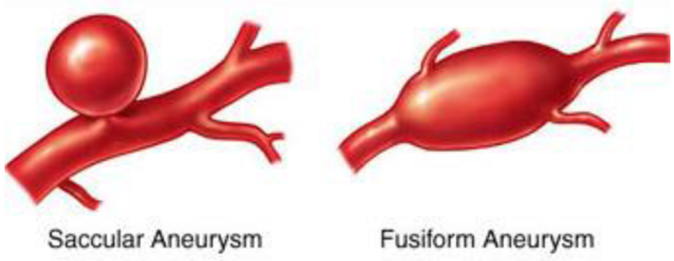

Figure 11 - Typical aneurysm types [74]

2.3.2 Blood Clots

Venous thromboembolism (VTE) stands for the creation of blood clots, and depending on where such an event occurs, we distinguish between deep vein thrombosis (DVT, clot forms in arms and legs) and pulmonary embolism (PE, clot breaks loose and travels to the lungs). The formation of a clot can occur for a number of reasons, with some of the most common being vessel damage (inflammation, atherosclerosis), pregnancy, long bed rest, certain hormones, and/or high blood viscosity. When a clot clogs a particular vessel, such an event can be life-threatening, depending on where that vessel is located [19] [20] [5].

2.3.3 Varicose Veins

Varicose veins are one of the most common disorders in lower limbs are appears in the form of widespread baggy veins. Studies show that close to half of the developed countries population suffers from some form of varicose veins. We distinguish between primary and secondary type. The main cause of primary varicose veins remains unclear, but factors such as smoking, pregnancy, and age make for highly contributing factors. As for secondary varicose veins, they are usually the result of deep vein thrombosis (see previous sub-chapter). Varicose veins can be treated most commonly with a change in lifestyle, or, in more serious cases, with a surgery [21] [22] [5].

2.3.4 Atherosclerosis

Atherosclerosis is a disease which affects large arteries, and it is the primary cause of a heart attack and stroke; it is the underlying cause for close to 30% of all recorded deaths in the world [23].

Atherosclerosis is progressive disease defined by the accumulation of lipids and fibrous elements in large arteries. Damage to the inner artery wall can cause some of the endothelial cells to change their properties and make a small hole in the wall. Over time, substances like cholesterol, fats, and cellular waste can accumulate inside this damaged area. The presence of cholesterol initiates inflammatory response in the surrounding endothelium cells which causes monocytes from the bloodstream to travel to the damaged area. Thanks to the cholesterol present, such monocytes transform to macrophages and later to so called foam cells. Together, these foam cells, along with necrotic core, form a plaque that thickens and hardens over time. In order to reinforce the affected inner arterial wall, smooth muscle cells group together to form a fibrous cap, preventing the plaque from growing. Once the plaque is big enough, though, it can burst and release the plaque into the bloodstream where it can contribute to the formation of a blood clot, preventing blood from flowing and causing a heart attack or a stroke, depending on the affected area. It can also cause rupture in the artery wall which leads to internal bleeding [23] [24] [25].

2.3.4.1 Lesion Initiation in Greater Detail

Fluid shear stress has a great effect on the endothelial cells (EC). When the blood flow is uniform and laminar, EC are ellipsoid in shape and aligned in the direction of flow. When the flow is disturbed and the oscillating shear stress levels are less than 0.4 $[Pa \cdot s]$, EC have polygonal shapes and no particular orientation; these locations are mainly arterial branching and curvatures. These EC properties can also develop with hypercholesterolemia (high level of cholesterol in blood). These areas then show increased permeability to specific molecules, especially low-density lipoprotein cholesterol (LDL-C), allowing them to migrate into the arterial wall. Once in the vessel wall, LDL undergoes a certain modification, more precisely oxidation, lipolysis, proteolysis, and other reactions, allowing macrophages to generate foam cells out of LDL. The initiation process, however, is largely complex and includes other complex molecules and processes, which will further not be discussed in this thesis [24] [25] [26].

2.3.4.2 Atherosclerotic Plaque Structure

As mentioned in the previous sub-chapters, structure of the forming atherosclerotic plague is rather complex and contains various different elements. For the purposes of the simulation in this thesis, we will only distinguish between fibrous cap and the lipid core as a whole. The difference between a healthy artery and one infected with atherosclerotic plaque is displayed in Figure 12.

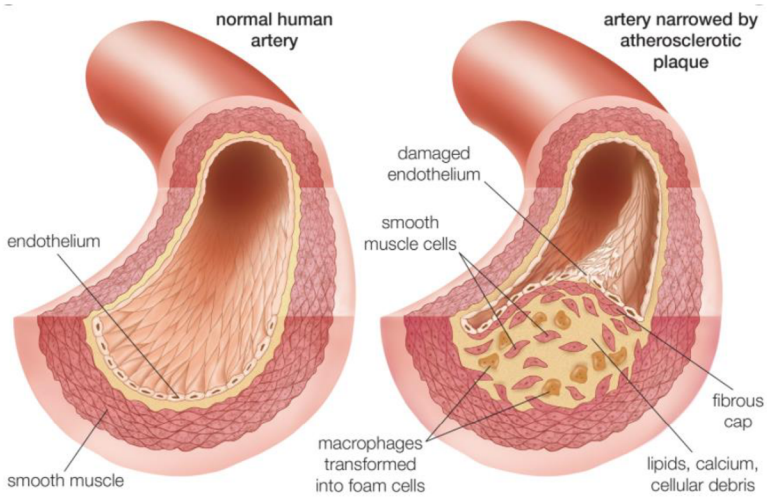

Figure 12 - Healthy artery (left) and infected artery (right) [73]

2.3.4.3 Atherosclerosis Treatment

As of today, medications and surgery can be used to reverse or treat atherosclerosis, but there are also a number of ways to prevent it to a certain level, and also to stop it from getting worse. We can, for example, reduce cholesterol levels or lower blood pressure with lifestyle changes and certain medicaments. If atherosclerosis becomes too severe, it can then be treated for example with angioplasty, endarterectomy, or a bypass. In case of medication, LDL-cholesterol lowering drugs or blood thinners can be used [27].

2.4 Constitutive Models of Biological Tissues

2.4.1 Finite Strain Theory

When dealing with typical construction materials, we assume that their deformations are rather low, more specifically up to 1%. Biological tissue, however, as well as a group of other materials (for example rubber) do not satisfy this criterion and thence cannot be treated similarly. To describe the behavior of these materials, more general strain tensors have to be introduced, the theory of which is called Finite Strain Theory. We distinguish between two basic approaches; Lagrangean (used in the mechanics of solid bodies – independent variable is the undeformed geometry) and Eulerian (used in fluid mechanics – independent variable is the deformed geometry) [28] [29].

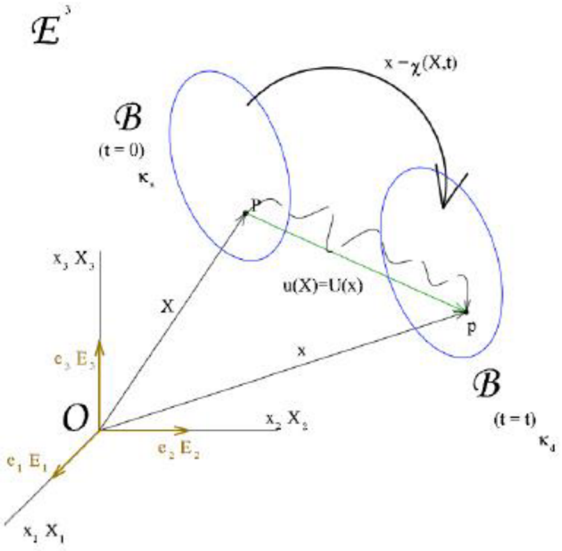

Figure 13 - Finite Strain Theory, taken from [70]

2.4.1.1 Deformation tensors

Although the number of deformation tensors is larger, this thesis will only describe two of them: the deformation gradient tensor and the right Cauchy-Green deformation tensor, since they are necessary for the constitutive models used in this thesis.

2.4.1.1.1 The Deformation Gradient Tensor

This deformation tensor is represented by the symbol ***F*** and it expresses the transformation between current and initial geometry [29]. It consists of proportionate elongations:

$$\lambda_x = \frac{\partial x}{\partial X} \tag{1}$$

$$\lambda_y = \frac{\partial y}{\partial Y} \tag{2}$$

$$\lambda_z = \frac{\partial z}{\partial Z} \tag{3}$$

and is defined as

$$F_{ij} = \frac{\partial x_i}{\partial X_j} \tag{4}$$

with individual elements being the aforementioned proportionate elongations. Deformation gradient tensor in general coordinates can then be written as:

$$\boldsymbol{F}_{ij} = \begin{bmatrix} \frac{\partial x_1}{\partial X_1} & \frac{\partial x_1}{\partial X_2} & \frac{\partial x_1}{\partial X_3} \\ \frac{\partial x_2}{\partial X_1} & \frac{\partial x_2}{\partial X_2} & \frac{\partial x_2}{\partial X_3} \\ \frac{\partial x_3}{\partial X_1} & \frac{\partial x_3}{\partial X_2} & \frac{\partial x_3}{\partial X_3} \end{bmatrix} \tag{5}$$

Deformation gradient tensor carries both the information about deformation and translation, which is why it cannot be used to evaluate strain. By calculating the determinant of this matrix, we can calculate the third invariant of this tensor as

$$J = det(\boldsymbol{F}) = \lambda_1 \lambda_2 \lambda_3 \tag{6}$$

which gives us the proportionate volume change of a given element. The deformation gradient tensor is generally asymmetric which is why two different Cauchy-Green deformation tensors (left and right) exist [28] [29].

2.4.1.1.2 The Cauchy-Green Deformation Tensor (Right)

This definition also works with proportionate elongations and is directly derived from the deformation gradient tensor as:

$$\boldsymbol{C} = \boldsymbol{F}^T \boldsymbol{F} \quad \leftrightarrow \quad C_{ij} = F_{ki} F_{kj} \tag{7}$$

with this tensor's principal coordinates being the proportionate elongations in principal directions squared:

$$\boldsymbol{C} = \begin{pmatrix} \lambda_1^2 & 0 & 0 \\ 0 & \lambda_2^2 & 0 \\ 0 & 0 & \lambda_3^2 \end{pmatrix} \tag{8}$$

The invariants of this tensor can, in the principal coordinate system, be expressed followingly:

$$I_1 = \gamma_1^2 + \gamma_2^2 + \gamma_3^2 \tag{9}$$

$$I_2 = \gamma_1^2 \gamma_2^2 + \gamma_2^2 \gamma_3^2 + \gamma_1^2 \gamma_3^2 \tag{10}$$

$$I_3 = \gamma_1^2 \gamma_2^2 \gamma_3^2 = J^2 \tag{11}$$

Here, J is the third invariant of the deformation gradient tensor. This means that even with the Cauchy-Green deformation tensor, third invariant expresses the change in volume (it is equal to one when volume remains constant). Other known deformation tensors are for example Almansi-Hamel, Green-Lagrange, logarithmic Cauchy, and several others [29] [28].

2.4.1.1.3 Modified Invariants of the Cauchy-Green Deformation Tensor

Modified (sometimes also reduced) invariants are often used in hyperelastic constitutive models to describe the shape component of the strain density function, and they are calculated using modified principal elongations calculated as:

$$\overline{\lambda_p} = J^{-1/3} \cdot \lambda_p \quad (p = 1,2,3) \tag{12}$$

Modified invariants of the right Cauchy-Green deformation tensor are afterward [28] [29]:

$$\overline{I_1} = \bar{\lambda}_1^2 + \bar{\lambda}_2^2 + \bar{\lambda}_3^2 = I_1 \cdot J^{-1/3} \tag{13}$$

$$\overline{I_2} = \bar{\lambda}_1^2\bar{\lambda}_2^2 + \bar{\lambda}_2^2\bar{\lambda}_3^2 + \bar{\lambda}_1^2\bar{\lambda}_3^2 = I_2 \cdot J^{-2/3} \tag{14}$$

2.4.1.2 Stress Tensors

To properly determine the strain energy function, we have to work with mutually equivalent stress and deformation tensors (these are then called energetically conjugated tensors). This is why below we introduce several different stress tensors [29].

2.4.1.2.1 Cauchy Stress Tensor

Cauchy stress tensor (also called Euler's) is defined as true elementary force applied on real (deformed) element area. It often represents true stresses in a structure, it is energetically conjugated with the Almansi deformation tensor, and is formally written as [29]:

$$\sigma_i = \frac{dF_i}{dx_j dx_k} \tag{15}$$

2.4.1.2.2 I. Piola-Kirchhoff Stress Tensor

I. Piola-Kirchhoff stress tensor (also called Lagrange's) is defined as true elementary force applied on the original (undeformed) element area. If often represents engineering stresses, is energetically conjugated with the Green-Lagrange deformation tensor, and is formally written as [29]:

$$\tau_i = \frac{dF_i}{dX_j dX_k} \tag{16}$$

2.4.1.2.3 II. Piola-Kirchhoff Stress Tensor

II. Piola-Kirchhoff stress tensor (also called Kirchhoff's) is defined as elementary force applied on the original (undeformed) element area. This force, however, is changed compared to the true force in same respect as an elementary dimension in the corresponding direction. This dimension is changed following the formula:

$$dx_i = \frac{\partial x_i}{\partial X_i} dX_i \tag{17}$$

and in the same manner when transforming into an undeformed state:

$$dX_i = \frac{\partial X_i}{\partial x_i} dx_i. \tag{18}$$

Elementary force is then transformed accordingly as:

$$dF_{0i} = \frac{\partial X_i}{\partial x_i} dF_i. \tag{19}$$

so that the stress is (and in the first principal direction):

$$S_i = \frac{dF_{0i}}{dX_j dX_k} \rightarrow S_1 = \frac{\frac{\partial X_1}{\partial x_1} dF_1}{dX_2 dX_3} \tag{20}$$

This tensor has no physical meaning but is mainly used because it is symmetrical even for large strains and it is energetically conjugated with the Green-Lagrange deformation tensor [28] [29].

2.4.2 Hyperelastic Materials

Materials are called hyperelastic if there exists an elastic potential function W (strain energy) which is a scalar function of a given strain/deformation tensor and whose partial derivative with respect to a strain component determines the according stress component. This can be expressed for example as:

$$S_{ij} = 2\frac{\partial W}{\partial C_{ij}}, \tag{21}$$

where S_{ij} are components of the II. Piola-Kirchhoff's stress tensor, W is strain energy function related to an undeformed volume, and C_{ij} are components of the right Cauchy-Green deformation tensor [29].

Hyperelastic materials express large deformations, and they return to their original configuration upon relief. Typical hyperelastic materials are rubbers, foams, and biological tissues (in computational modeling). There is a large number of hyperelastic constitutive models, depending on their directional properties, whether or not they respect inner material structure, whether or not they can be compressed, whether or not is their behavior elastic, in accordance with their mathematical formulation, and in accordance with the deformation tensor used [29]. With respect to the goals of this thesis, we will limit ourselves to isotropic, incompressible models, and next sub-chapter will describe some of them.

2.4.2.1 Isotropic Hyperelastic Materials

Isotropic models have the same properties in all directions. Even though this creates a certain inaccuracy, more comprehensive material data are often unavailable, and computations with them are much more time-consuming.

2.4.2.1.1 Neo-Hooke Model

This model assumes that the final molecule chain location during its deformation follows the Gauss distribution. Thence it is the first model to respect the structure of materials (even though only elementary). It defines strain energy as:

$$W = \frac{1}{2} NkT(\lambda_1^2 + \lambda_2^2 + \lambda_3^2 - 3) \tag{22}$$

where:

- N is the number of chains in a volume unit (number of particles) $[-]$
- k is the Boltzmann's constant $(1.38 \cdot 10^{-23}\, JK^{-1})$
- T is thermodynamic temperature $[K]$.

By substituting the constants with G (shear modulus) and proportionate elongations with the first modified Cauchy-Green invariant, we can write this formula as:

$$W = \frac{G}{2}(\bar{I}_1 - 3) \tag{23}$$

This model fails with higher strains which is why more complex models were made based on this one, to compensate for this deficiency; the most known from these is the Arruda-Boyce model [30].

2.4.2.1.2 Mooney-Rivlin Model

Multi-parameter material model which uses the first two modified invariants of the Cauchy-Green deformation tensor. The more complicated model we use (2,5,9 material parameters), the more complex stress-strain curves it can describe [29]. The general model formula is as follows:

$$W = \sum_{i,j-1}^{3} c_{ij}(\bar{I}_1 - 3)^i\,(\bar{I}_2 - 3)^j \tag{24}$$

with c_{ij} being the aforementioned material parameters and $\bar{I}_1$, $\bar{I}_2$ being modified invariants of the Cauchy-Green deformation tensor.

2.4.2.1.3 Arruda-Boyce Model

Compared to all the other isotropic models mentioned in this thesis, Arruda-Boyce model is not fenomenological, but it comes from the material structure, made of entangled chains of elastomer macromolecules. When they straighten, the material becomes tougher (deformation strengthening). A-B model, however, is highly simplified, because the distribution and orientation of these fibers is mostly random. This model is created by developing an infinite series and if we assume that the material is incompressible, its strain energy function can be calculated as:

$$W = G\left[\frac{1}{2}(\bar{I}_1 - 3) + \frac{1}{20\lambda_L^2}(\bar{I}_1^2 - 9) + \frac{1}{1050\lambda_L^4}(\bar{I}_1^3 - 27) + \frac{19}{7000\lambda_L^6}(\bar{I}_1^4 - 81) + \frac{519}{673750\lambda_L^8}\left(\bar{I}_1^5 - 243\right)\right] \tag{25}$$

where:

- λ_L is the limit elongation of a given chain [–]
- G is shear modulus $[MPa]$
- $\bar{I}_1$ is a modified invariant of the Cauchy-Green deformation tensor [–] [29]

2.4.2.1.4 Yeoh Model

Yeoh model originates in the Mooney-Rivlin formulation. Yeoh proved that the increments from the first invariant are higher than those from the second invariant, which is why he proposed the following strain energy function:

$$W = \sum_{i=1}^{5} C_{i0}(\bar{I}_1 - 3)^i \tag{26}$$

which can be developed into (only the first 3 members of the series):

$$W = C_{10}(\bar{I}_1 - 3) + C_{20}(\bar{I}_1 - 3)^2 + C_{30}(\bar{I}_1 - 3)^3 \tag{27}$$

with C_{10}, C_{20}, C_{30} being material parameters [29]. This model is used in this thesis as both, 1, 2, and 3-parameter constitutive model describing behavior of the internal carotid artery.

2.5 Blood

Blood is a medium that transports various substances throughout the human body. It is not a pure liquid, rather than a mixture of red blood cells (erythrocytes), white blood cells (leukocytes), platelets (thrombocytes), and blood plasma (consisting mostly of water). Average human organism contains in between 5 and 6 liters of blood. In terms of mechanics, it is a non-Newtonian fluid, and its flow within the vessels is mostly laminar; its mechanic characteristics will further be discussed in the following chapters [11]. Individual component representation within blood is displayed in Figure 14.

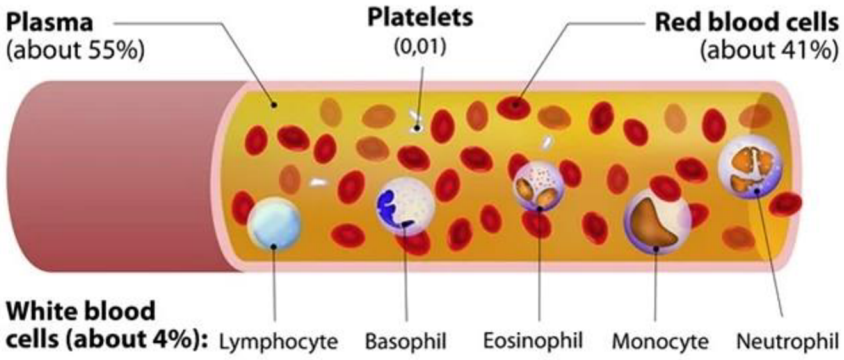

Figure 14 - Individual blood components [72]

2.5.1 Blood Components

As stated earlier, we distinguish between 4 main blood components:

- Red blood cells (Erythrocytes)
  - Nucleus-free cells which contain hemoglobin, whose primary function is to distribute oxygen. They are created in bone marrow and their lifespan is about 120 days. They also make the majority of all blood cells [5].
- White blood cells (Leukocytes)
  - We distinguish between several different types, varying both in function, place of origin, and lifespan. Their general purpose, however, is to defend the organism against infection, and to provide immunity [5].
- Platelets (Thrombocytes)
  - Nucleus-free cells with a lifespan of 8-10 days. Their main purpose is to help in case of hemostasis (blood being outside of body/vessels) where they adhere to the affected vessel walls to prevent more blood from leaking [5].
- Blood plasma
  - Yellow liquid, 90% of which is made out of water, while the rest is made of several different proteins, glucose, and lipids. It plays a vital role in keeping the electrolyte concentration balanced and it protects the human body from infection [5].

2.5.2 Blood Pressure

As the heart contracts and relaxes, blood is sent to the circulatory system, where it loads vessels with a certain pressure. We generally distinguish between systolic and diastolic pressure. Systolic pressure occurs when the heart contracts and pumps oxygen-rich blood into the human body, while diastolic pressure occurs when the heart muscle relaxes. From this, we can also conclude that systolic pressure is always higher than diastolic pressure. The referential values of blood pressure are usually 120/80 mmHg (systolic/diastolic). Blood pressure is normally measured in millimeters of Mercury $[mmHg]$ with a blood pressure monitor or a sphygnomanometer, but since this unit is rather difficult to work with and most programs do not support it, we will further convert this unit to $[kPa]$ using the following conversion [11] [31]:

$$1mmHg = 0.133kPa$$

Blood pressure generally changes as blood proceeds further from the heart, because vessels are pliable and absorb some of it. Since we are dealing with the Internal carotid artery (ICA), we will limit ourselves to a pressure record displayed in Figure 15, describing one pressure waveform (one heart cycle) in the common carotid artery [32].

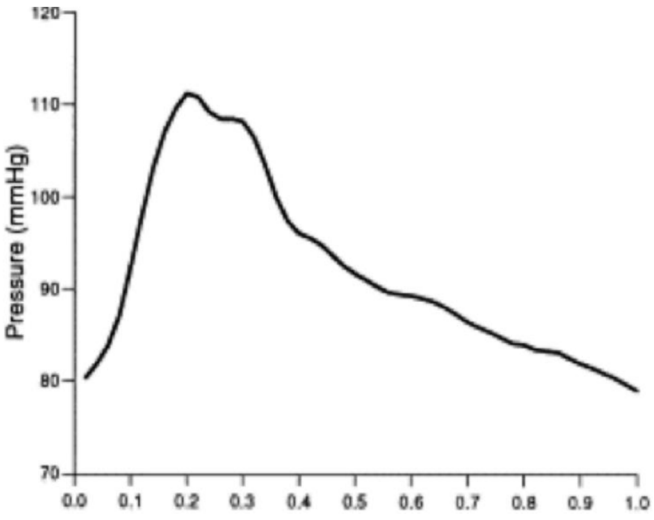

Figure 15 - Pressure waveform in CCA over 1 second [32]

2.6 Non-Newtonian Fluids

Fluids can generally be classified in two different ways; in accordance with their response to externally applied pressure or in accordance with their response to shear stress. The first criterion divides fluids into compressible and incompressible, depending on how the fluid volume element is dependent on its pressure. While gases are compressible, liquids can generally be looked upon as incompressible, since their volume does not quite change upon applying pressure. This is why we further limit ourselves to distinguishing fluids based on their response to shearing [33].

2.6.1 Classification of Fluids

To be able to properly distinguish between Newtonian and non-Newtonian fluids, we must first introduce the term viscosity, because this fluid property defines whether or not a given fluid belongs to a particular category.

General force dF applied on general surface dS has a tangential force component dF_t which introduces shear stress. Using the Newton's law, we can calculate this shear stress on the wall of an elementary prism of height dn as:

$$\tau = \frac{dF_t}{dS} = \eta \frac{dv}{dn} = \eta \dot{\gamma}_{yx} \tag{28}$$

With $\frac{dv}{dn}$ being shear rate $[s^{-1}]$, τ being shear stress $[Pa]$, and η being Newtonian viscosity $[Pa \cdot s]$ [33] [34].

2.6.1.1 Newtonian and Non-Newtonian Fluids

Newtonian fluids can be described as fluids, whose constant of proportionality η $[Pa \cdot s]$ (called Newtonian viscosity) is independent on shear rate ($\dot{\gamma}_{yx}$) and shear stress (τ_{yx}), and depends only on the material, its temperature, and pressure [33].

Non-Newtonian fluids are, on the other hand, defined as fluids with Newtonian viscosity being a function of shear stress and/or shear rate. This group contains emulsions, mixtures of solids and liquids, paints, and many other substances, with blood being one of them. The difference between Newtonian and non-Newtonian fluids can most easily be seen using a rheogram; a graph of shear stress and shear rate dependency [34] [33]. This rheogram is displayed in Figure 16.

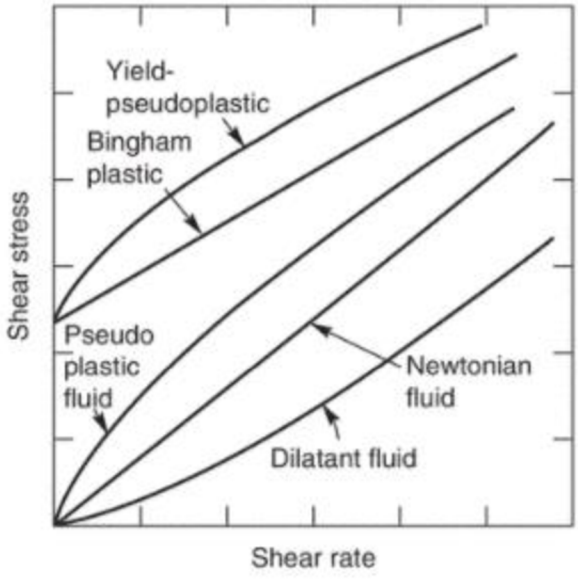

Figure 16 - Fluid rheogram [33]

2.6.2 Blood Rheology

Blood is a complex pseudoplastic non-Newtonian fluid exhibiting viscoelastic behavior, yield stress, and thixotropy (which are all explained later). These properties affect both the functioning of blood and the stresses generated within vessel walls. Blood properties are highly dependent on its flow rate. If it is low, red blood cells form into aggregations which increases blood viscosity. And similarly, if it is high, these aggregations are broken up and viscosity decreases [35] [36]. This dependency can be seen in Figure 17, also considering hematocrit levels (ratio of the volume of red blood cells to the total blood volume).

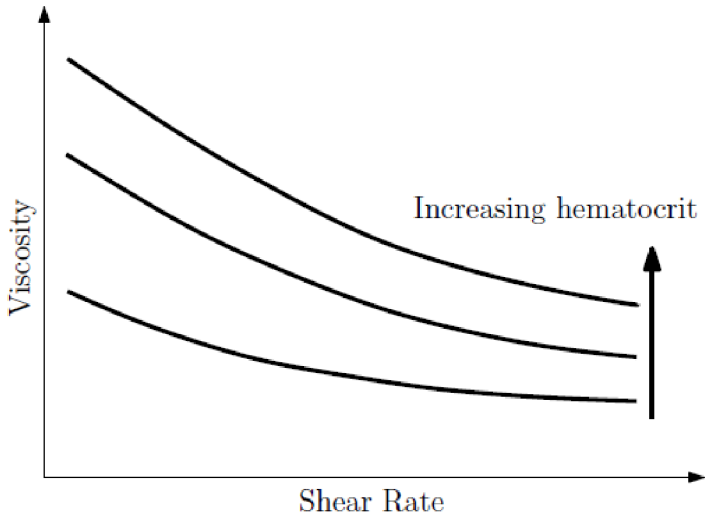

Figure 17 - Human blood viscosity as a function of shear rate [35]

2.6.2.1 Viscoelasticity

Viscoelasticity is a characteristic of materials which exhibit both viscous and elastic behavior, and is defined as the ability of a fluid to accumulate and release energy. Blood is viscoelastic due to the deformability of red blood cells and their ability to create 3D structures (aggregations – Rouleax). It is also influenced by the hyperelastic characteristics of vessel walls. Since blood aggregations are mostly demonstrated at low shear rates, viscoelasticity is mainly pronounced at these regimes of low deformation. Viscoelastic effects are also highly influenced (if not started) by the pulsatile nature of blood flow [35] [37].

Viscoelastic behavior is defined using the Deborah number. This number is expressed as the ratio of time constant λ_r (relaxation time) and characteristic time t_C during which is material deformed. Relaxation time can also be defined as the ratio of viscosity η to Young's modulus E:

$$D_e = \frac{\lambda_r}{t_C}, \quad \lambda_r = \frac{\eta}{E} \tag{29}$$

Using this number, we can calculate what kind of behavior will a given material exhibit. If $D_e \ll 1$, material will be viscous, and by contrast, if $D_e \gg 1$, material will be elastic. If $D_e \sim 1$, fluid (which is the case of blood) will exhibit viscoelastic behavior, which has to be accounted for in numerical simulations [38].

2.6.2.2 Yield stress

Yield stress is the limit stress needed for the blood to start flowing, below which blood acts like a solid. This behavior has a significant impact on the coagulability of blood which can help with healing wounds. It, however, can also contribute to the creation of blood clots (thrombosis) which can pose some serious health risks. Yield stress influence can be neglected in large arteries, since the blood in there flows at higher rates, but it has a significant influence in capillaries where the blood flow rate is much lower [35] [36] [39]. This behavior is displayed in Figure 18.

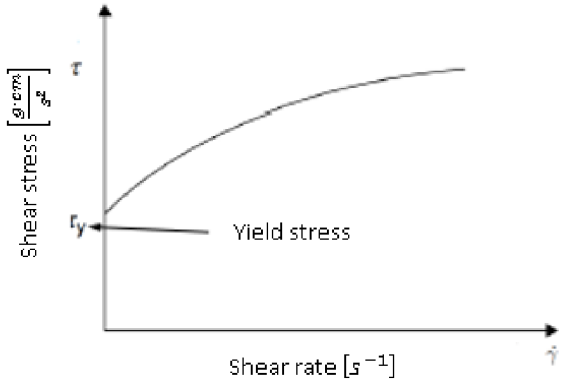

Figure 18 - Shear stress-shear rate blood dependency. Adjusted from [36]

2.6.2.3 Pseudoplasticity

Pseudoplastic (more specifically yield-pseudoplastic, here also called shear thinning) blood behavior can be seen in Figure 16 and Figure 18. To describe this behavior in more detail, such a fluid evinces decrease in viscosity with increasing value of shear stress. As mentioned in subchapter 2.6.2.1, once shear stress increases, red blood cell aggregations split up and consequently decrease blood viscoelasticity [35].

2.6.2.4 Thixotropy

Thixotropy is a time-dependent shear thinning material property. It is a characteristic of some pseudoplastic materials, and it is characterized by large viscosity for initial values of shear stress which, however, then decreases over time. It is a transient attribute which can have a long-term effect on the circulatory system, mainly due to the pulsative nature of blood flow. It is also more distinct with lower shear rates and it is dependent on blood composition [36] [40].

2.6.2.5 *Material Models of Blood*

When dealing with large arteries and high shear rates, it is believed that blood generally acts almost like a Newtonian fluid, and that non-Newtonian properties are only applicable with small arteries. Nevertheless, some physiological and pathological situations cause the non-Newtonian blood properties to have greater influence, which is why these properties are taken into consideration when building the blood material model. Available applicable blood material models are displayed in Figure 19 and the model used in this thesis is Carreau-Yasuda, described in the next subchapter [41] [36].

Model	Equation	Non-Newtonian Properties
Carreau-Yasuda	$\mu = \mu_\infty + \frac{\mu_0 - \mu_\infty}{[1+(\lambda\dot{\gamma})^a]^{\frac{1-n}{a}}}$	shear thinning
Casson	$\tau^{1/2} = (k\dot{\gamma})^{1/2} + \tau_o^{1/2}$	yield stress
Power law	$\tau = k\dot{\gamma}^n$	shear thinning
Cross	$\mu = \mu_\infty + \frac{\mu_0 - \mu_\infty}{1+\lambda\dot{\gamma}^m}$	shear thinning
Herschel-Bulkley	$\tau = k\dot{\gamma}^n + \tau_o$	shear thinning, yield stress
Oldroyd-B	$\boldsymbol{\tau} + \lambda_1 \overset{\nabla}{\boldsymbol{\tau}} = \mu_0 \left(\dot{\boldsymbol{\gamma}} + \lambda_2 \overset{\nabla}{\dot{\boldsymbol{\gamma}}} \right)$	viscoelasticity
Quemada	$\mu = \mu_p \left(1 - \frac{k_0 + k_\infty \sqrt{\dot{\gamma}/\dot{\gamma}_c}}{2\left(1+\sqrt{\dot{\gamma}/\dot{\gamma}_c}\right)} \phi \right)^{-2}$	shear thinning
Yeleswarapu	$\mu = \mu_\infty + (\mu_0 - \mu_\infty) \frac{1+\ln(1+\lambda\dot{\gamma})}{1+\lambda\dot{\gamma}}$	shear thinning
Bingham	$\tau = k\dot{\gamma} + \tau_o$	yield stress
Eyring-Powell	$\mu = \mu_\infty + \frac{(\mu_0 - \mu_\infty)\sinh^{-1}(\lambda\dot{\gamma})}{\lambda\dot{\gamma}}$	shear thinning
Ree-Eyring	$\tau = \tau_c \sinh^{-1}\left(\frac{\mu_0\dot{\gamma}}{\tau_c}\right)$	shear thinning

Figure 19 - Non-Newtonian fluid models [35]

2.6.2.5.1 Carreau-Yasuda Model

The general formulation of the Carreau-Yasuda model is:

$$\eta(\dot{\gamma}) = \eta_\infty + (\eta_0 - \eta_\infty) \cdot [1 + (\lambda\dot{\gamma})^a]^{\frac{n-1}{a}} \tag{30}$$

where:

- η_∞ is the viscosity in high shear $[Pa \cdot s]$
- η_0 is the viscosity in low shear $[Pa \cdot s]$
- λ is a time constant $[s]$
- n is a weight index (Power Law index)
- $\dot{\gamma}$ is shear rate $[s^{-1}]$
- a is an exponent $[-]$

This model complies with the condition of variable viscosity and is used mainly because of the availability of experimental data. Specific values are discussed further in this thesis [36] [42].

2.7 Fluid Flow Theory

2.7.1 Laminar and Turbulent Flow

Fluid flow is generally divided into laminar and turbulent. While we generally understand the nature of both, this transient behavior is still an open research area, and the mechanics are yet to be fully described [43].

Laminar flow is defined as a flow with particles moving in layers, while these particles do not move across the cross section. Turbulent flow is defined as a flow where these particles, apart from moving forward, also move in between different layers, thus creating a turbulence [34]. The basic criterion in determining whether a flow is laminar or turbulent (for blood, in our case) in the Reynolds number, which can be calculated as:

$$Re = \frac{v_s \cdot D \cdot \rho}{\eta} \tag{31}$$

where:

- v_s is flow speed $\left[\frac{m}{s}\right]$
- D is diameter $[m]$
- ρ is density $\left[\frac{kg}{m^3}\right]$
- η is dynamic viscosity $[Pa \cdot s]$
- Re is Reynolds number $[-]$

The critical value of Re varies throughout different sources, but it is always somewhere around $Re_k = 2200 \div 2300$. If the Re value is below this threshold, flow will be laminar. If Re is above this critical value, flow will be turbulent. Both of these flows are displayed in Figure 20 [34].

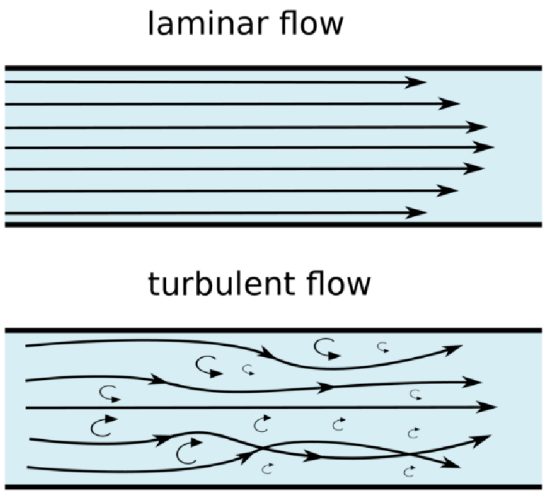

Figure 20 - Laminar and turbulent flow [75]

The only place where the flow is turbulent within the human body is the proximal part of the upward abdominal aorta. The nature of blood flow withing the human body is otherwise laminar, which is why we will further limit ourselves to laminar flow [36].

2.7.2 Poiseuille's Law

When dealing with laminar flow, Poiseuille's law can be used to determine the stationary part of the pulsatile blood flow. This law defines the relationship between pressure drop and fluid flow in a rigid tube (we have to assume stationary laminar flow and invariable viscosity). It also proves that the laminar flow rate of an incompressible fluid along a pipe is proportional to the fourth power of the pipe's radius [36]. The formula is then as follows:

$$Q = \frac{\Delta P \cdot \pi \cdot r_i^4}{8 \cdot \eta \cdot l} \tag{32}$$

where:

- Q is volumetric flow $\left[\frac{m^3}{s}\right]$
- ΔP is the decrease in pressure over the tube length $[Pa]$
- η is dynamic viscosity $[Pa \cdot s]$
- r_i is the tube radius $[m]$
- l is the tube length $[m]$ [36]

2.7.3 Womersley Velocity Profile

As mentioned in the previous subchapter, Poiseuille's law only works for stationary flow. Since blood flow is not stationary but rather pulsatory, this law cannot be applied. This oscillatory flow was analyzed by Womersley (1955) for a laminar flow of an incompressible Newtonian fluid with a single frequency sinusoidal pressure gradient. Since this theory is based on sinusoidal shapes, Fourier analysis has to be applied when applying this theorem to hematocrit [44] [45]. Womersley then formulated formulas for velocity and flow profiles as:

$$v(r,t) = Re\left[\frac{\Delta P}{l} \cdot \frac{1}{i\omega\rho} \cdot \left\{1 - \frac{J_0\left(\alpha \cdot y \cdot i^{\frac{3}{2}}\right)}{J_0\left(\alpha \cdot i^{\frac{3}{2}}\right)}\right\} e^{i\omega t}\right] \tag{33}$$

$$Q(t) = Re\left[\cdot \frac{\pi \cdot r_i^2 \cdot \Delta P}{i\omega\rho l} \cdot \left\{1 - \frac{2J_1\left(\alpha \cdot i^{\frac{3}{2}}\right)}{\alpha \cdot i^{\frac{3}{2}} \cdot J_0\left(\alpha \cdot i^{\frac{3}{2}}\right)}\right\} e^{i\omega t}\right] \tag{34}$$

where:

- $Re[\dots]$ is the real part of a complex function
- i is imaginary unit [–]
- r_i is artery radius $[m]$
- y is distance from the center $[m]$
- $\frac{\Delta P}{l}$ is pressure gradient $\left[\frac{Pa}{m}\right]$
- ρ is blood density $\left[\frac{kg}{m^3}\right]$
- J_0 is a first kind Bessel function of the order zero
- J_1 is a first kind Bessel function of the order one
- $\omega = 2\pi f$ is angular velocity dependent on the pulsatory frequency (60beats/min = 1Hz)
- α is the Womersley parameter

Womersley parameter is used to express the relative importance of inertial effects in comparison to viscous flow and can be calculated as:

$$\alpha^2 = \frac{r_i^2 \cdot \omega \cdot \rho}{\eta} \tag{35}$$

with η being dynamic viscosity $[Pa \cdot s]$. The effects of several different Womersley numbers are displayed in Figure 21. As α approaches zero, flow shows a time varying parabolic velocity profile with pressure gradient and velocity in phase. Lower values of α also mean that the dominant element are viscous forces. This is why velocity profiles become parabolic and thus similar to the Poiseuille's formulations, meaning that with small blood vessels, theory of pulsatory flow does not have to be considered. As α increases (higher frequencies or larger diameters), the effects of viscosity are confined to a layer close to the wall (called the Stokes layer) while the profile in the middle is flat [44].

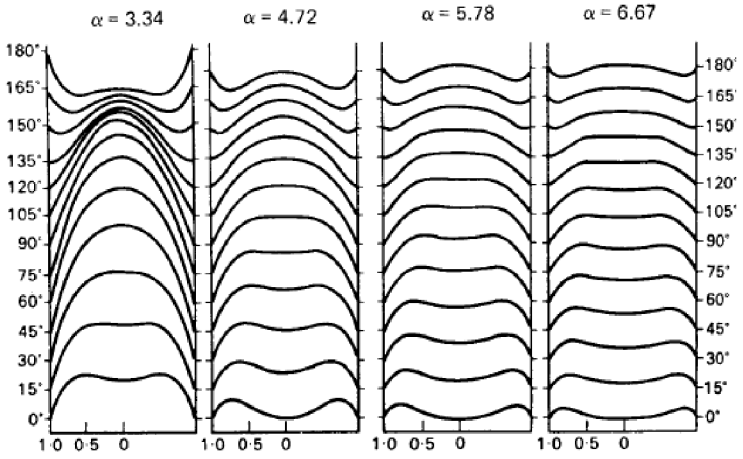

Figure 21 - velocity profiles for different Womersley numbers. Taken from [44]

2.8 Current State of Knowledge with Atherosclerotic Plaque Computational Modeling

This chapter gives a brief overview of the current state of computational modeling of the carotid artery with an atherosclerotic plaque. We will limit this overview to the following analysis types:

- Fully coupled fluid-structure interface analysis (FSI)
- One-way fluid-structure interface analysis (FSI)
- Structural analysis (pressure load applied on the artery wall)

Yuan Huang, et. al. [46] compare the resulting mechanical stresses in a carotid artery with an atherosclerotic plaque for a 2D structure-only, 3D structure-only, one-way, and fully coupled fluid-structure interaction analyses. They analyze 8 human carotid atherosclerotic plaques based on geometry reconstructed from in vivo computerized tomography and multi-sequence magnetic resonance images. The results show that the differences between structure-only and fully coupled FSI analyses produce small yet statistically significant stress differences, when the slices around bifurcation are excluded. They show that 2D structure-only models tend to slightly overestimate the stresses, compared to a fully coupled FSI analysis, while the other analyses provide comparable values. The material model used for these simulations is a modified Mooney-Rivlin formulation (hyperelastic, isotropic, incompressible) for the vessel, while blood is modelled as laminar, Newtonian, viscous, and incompressible. If, however, the investigated area is around the bifurcation, 2D model highly overestimates the stresses, see Figure 22.

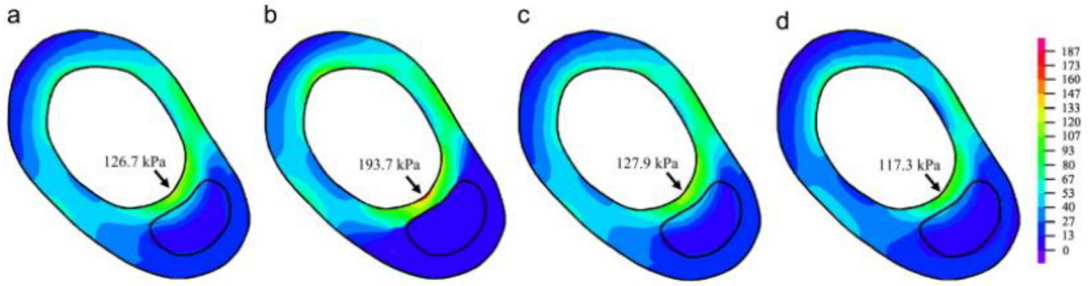

Figure 22 - Comparison of plaque wall stress on a transverse slice. Stress-P1 predicted by 3D fully coupled FSI (a), 2D structure-only (b), 3D one-way FSI (c) and 3D structure-only (d) models. Units are in kPa. Taken from [46]

Jianmin Yuan, et. al. [47] use a 3D FSI analysis to assess the impact of material property validation in predicting maximum principal stresses. Since there are some limitations to the data retrieved from in vivo, there is a need to assess whether variability in tissue material property measures (more specifically of media, fibrous cap, and lipid) impacts the overall calculation of the critical mechanical conditions within an atherosclerotic plaque. Samples were collected from 21 symptomatic patients, cut into rings along the axial direction and specific plaque parts were further isolated. These samples were then tested to assess their stress-strain curves. Author's conclusion is that these stress-strain curves vary widely with some of them being stiffer than others. This data is then subject to a fully coupled FSI analysis, using the Mooney-Rivlin hyperelastic model and Newtonian, viscous, and incompressible blood, to compare the resulting stresses for all possible data combinations. 3D geometry from this study is displayed in Figure 23.

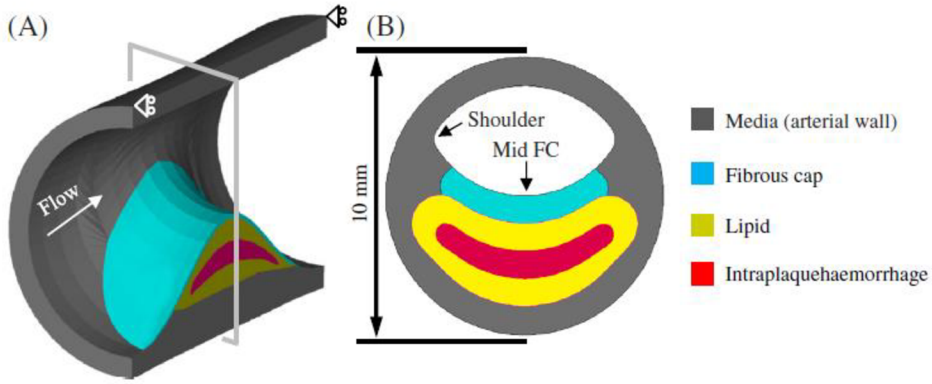

Figure 23 - 3D geometry of the idealized plaque model composed of fibrous cap, lipid and intraplaque hemorrhage. Taken from [47]

César Alegre-Martínez, et. al. [48] use a fully coupled FSI analysis to assess the impact of several parameters on the axial distribution of plaque stress in the carotid artery. The parameters in question are lipid core stiffness, lipid core length, and fibrous cap stiffness. The solid material model used in this study is non-linear hyperelastic, more specifically model Neo-Hookean, and blood is modelled as a steady flow of a Newtonian, incompressible fluid. Some of the results obtained in this study are displayed in Figure 24.

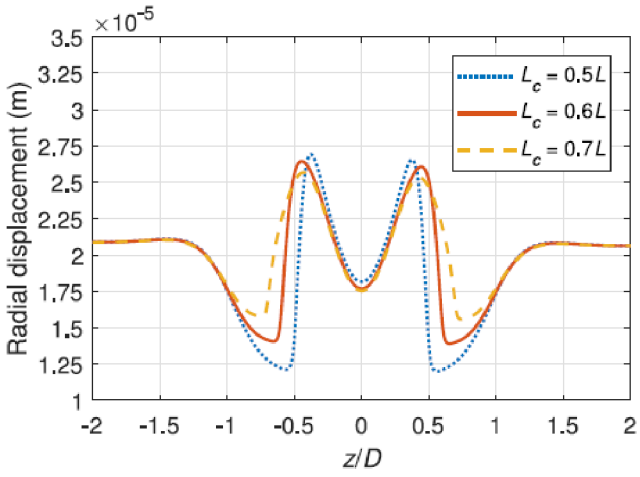

Figure 24 - Influence of the lipid core length on the axial distribution of radial displacements. Taken from [48]

Danny Bluestein, et. al. [49] study the influence of microcalcifications in the lipid core on vulnerable plaque mechanics using FSI analysis. The purpose of this study is to show whether the role of calcification in atherosclerotic plaque is beneficial or whether it has deleterious effects on plaque vulnerability. Solid is modelled using the Mooney-Rivlin hyperelastic model and fluid is assumed to be a Newtonian fluid. Modelled cases show higher stress peaks in models containing calcification.

Hao Gao, et. al. [50] perform a fully coupled FSI analysis on a patient specific CCA model obtained using a high-resolution multispectral MRI. Due to the rupture of this artery, as a cause of a transient ischaemic attack (TIA), these obtained are then reconstructed to comprehensively describe original geometry. The arterial wall is assumed to be isotropic, incompressible, and is described using 5-parameter Mooney-Rivlin formulation. Blood is then considered an incompressible, Newtonian fluid. Reconstructed geometry of the subject is displayed in Figure 25.

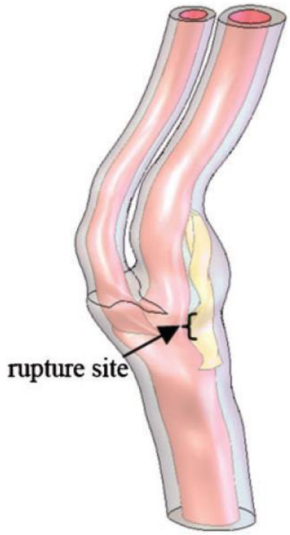

Figure 25 - reconstructed geometry of the subject with an indicated rupture site. Taken from [50]

Hao Gao and Quan Long [51] study the effects of lipid core volume and fibrous cap thickness on the stress distribution in carotid arterial plaques. The use a 3D model reconstructed from histology sections, which is then subject to a one-way FSI analysis with varying lipid volume and fibrous cap thickness. Solid is modelled as isotropic and incompressible, using the 5-parameter Mooney-Rivlin formulation, while blood is modelled as an incompressible, Newtonian fluid. Some of the studied cases are shown in Figure 26.

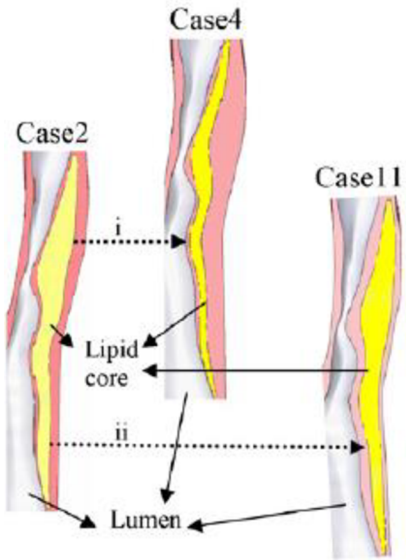

Figure 26 - schematic reconstruction of different study cases. Taken from [51]

Hao Gao, et. al. [52] use multi-contract MRI to obtain 4 different patient-specific models of CCA with differently shaped atherosclerotic plaques, upon which an FSI analysis in performed. The main characteristic of interest in this study is wall shear stress (WSS) which is one of the factors evaluated when assessing rupture risk possibility. Solid is modelled as isotropic and incompressible, using the 5-parameter Mooney-Rivlin formulation, while blood is modelled as isotropic, Newtonian fluid. Geometry reconstructions of used models are displayed in Figure 27.

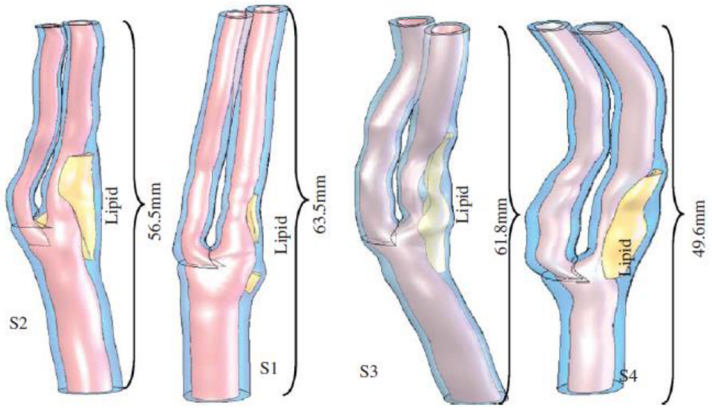

Figure 27 - geometry reconstruction of CCA for 4 patients. Taken from [52]

Joseph R. Leach, et. al. [53] perform an FSI analysis on a CCA plaque model obtained from multidetector computed tomography angiography (MDCTA). It is a patient specific study of an elderly man, aiming to predict stress distribution on a pre-rupture imaging. Solid in modelled as isotropic and incompressible, using the 5-parameter Mooney-Rivlin formulation, while blood is modelled as an incompressible, Newtonian fluid. Model representation is displayed in Figure 28.

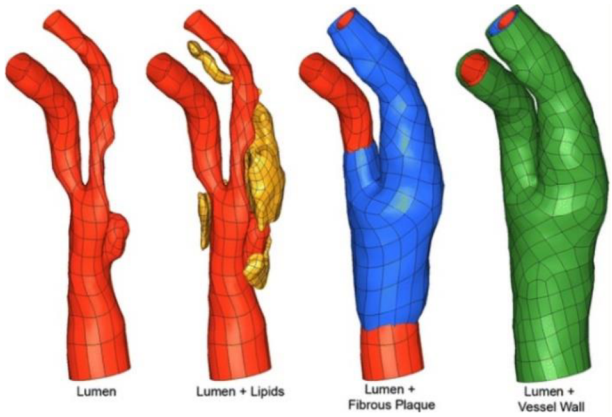

Figure 28 - Bounding surface of key vessel components. Taken from [53]

Ondřej Lisický, et. al. [54] perform a 3D structural analysis of the carotid artery (CCA) bifurcation with an atherosclerotic plaque. The aim of this study is to determine the effect of stiffness of several different structure components (lipid core, vessel wall, fibrous cap) on the resulting peak plaque and peak cap stresses. The model for this study is a patient-specific and obtained via magnetic resonance imaging (MRI). The materials are modelled as isotropic and hyperelastic, using the Yeoh model of different orders, with media being modelled separately as a fiber-reinforced anisotropic layer. The results of this study show that stiffness of different vessel-wall layers has a significant impact on the resulting stresses.

3 Simulation

3.1 Solid Model

3.1.1 Idealized Geometry Model

Since this thesis deals with an idealized geometry, rather than with patient-specific geometry, some referential values have to be established for this model. If we take a look at the vessel wall itself, it has three layers, all of which vary in thickness, depending on several different factors, including for example age and sex. This is why values from [54] and [55] were considered suitable for this thesis. As far as the diameter of the artery, thesis was inspired by the values from [56]. As for the plaque itself, referential dimensions were evaluated based on [57] .

After determining all the necessary dimensions, the model itself was created in *Design Modeler*, which is a proprietary software from *Ansys Inc*. It is divided into two parts; one consisting of intima, fibrous cap, and lipid core, and the other consisting of media and adventitia. Model is displayed in Figure 29, with dimensions listed in Table 1.

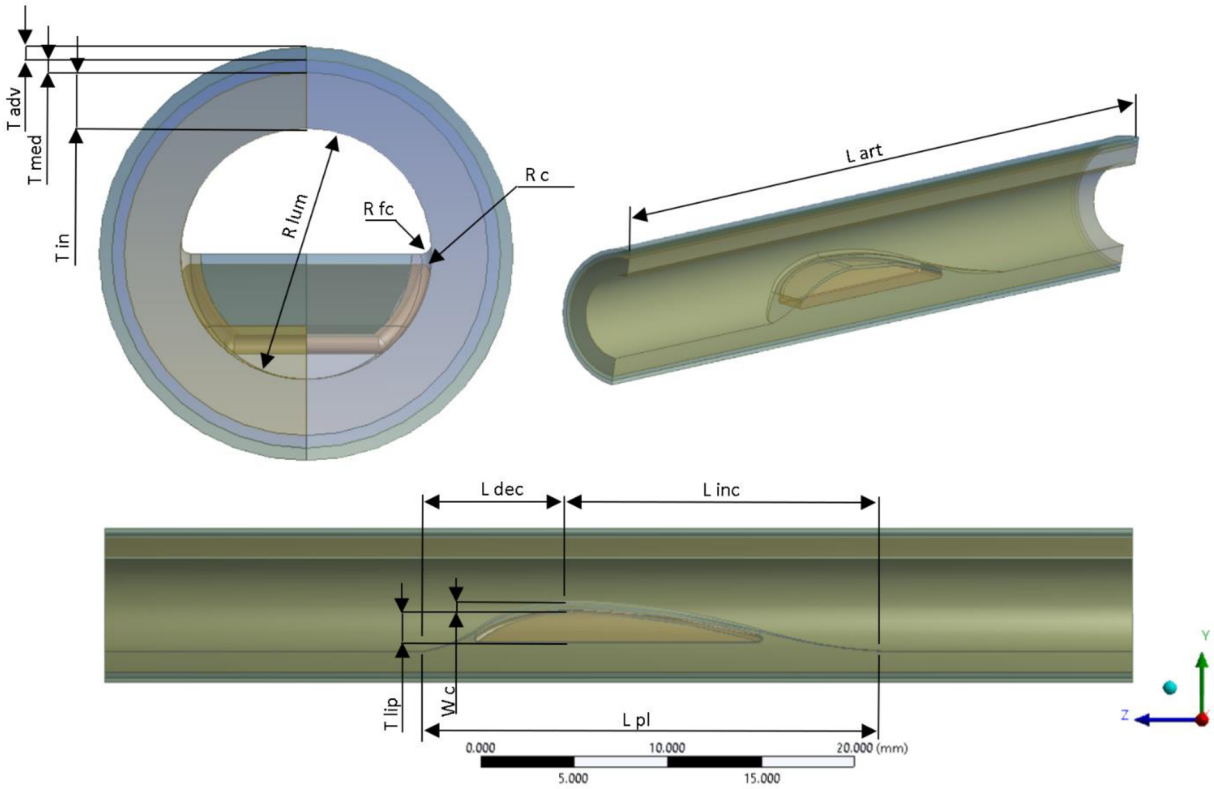

Figure 29 - Initial geometry

Table 1 - Solid model dimensions

Part	Symbol	Units	Value
Intima thickness	T_{in}	$[mm]$	1.12
Media thickness	T_{med}	$[mm]$	0.25
Adventitia thickness	T_{adv}	$[mm]$	0.25
Fibrous cap thickness	W_c	$[mm]$	0.2
Lipid core thickness (max)	T_{lip}	$[mm]$	1.8
Radius of lipid core edges	R_c	$[mm]$	0.2
Radius of lumen without stenosis	R_{lum}	$[mm]$	2.5
Radius of fibrous cap shoulder	R_{fc}	$[mm]$	0.2
Artery length	L_{art}	$[mm]$	55
Plaque length	L_{pl}	$[mm]$	25
Length of increasing/decreasing part	L_{inc}/L_{dec}	$[mm]$	17/8
Stenosis	-	$[\%]$	50

3.1.2 Material Model

As mentioned in chapter 2.4, biological materials do not behave ordinarily which is why we have to work with special material models when dealing with them. For this thesis, artery is modelled as isotropic, incompressible, and hyperelastic, using the Yeoh model, following the formula:

$$W = C_{10}(\bar{I}_1 - 3) + C_{20}(\bar{I}_1 - 3)^2 + C_{30}(\bar{I}_1 - 3)^3. \quad (36)$$

Specific material parameters for individual artery components are then taken from [54] and are shown in Table 2. Material parameters were obtained using a cyclic, quasi-static extension-inflation tests at different axial stretches, and are performed on preconditioned tube specimens [58] [59].

Table 2 - Material data for solid model

Tissue	Type	Material constants $[kPa]$		
Intima + fibrous cap	isotropic	$c_{10} = 50$	$c_{20} = 20$	-
Media	isotropic	$c_{10} = 122.3$	$c_{20} = 0$	$c_{30} = 337.7$
Adventitia	isotropic	$c_{10} = 88.7$	$c_{20} = 0$	$c_{30} = 45301.4$
Lipid core	isotropic	$c_{10} = 5$	-	-

This table shows that intima and fibrous cap use the same material model. This is dependent on the material model used and is also patient-specific. Additionally, since FSI analysis is a transient analysis, density has to be assigned to all layers, so that the mass matrix can be formed. The value used is $\rho = 1120 kg/m^3$. Proportional damping is also applied, with the values being: $Mass - Matrix\ Damping\ multiplier = 100$ and $k - Matrix\ Damping\ multiplier = 0.0001$.

3.1.3 Mechanical Setup

After the model and material data are created, structural analysis setup can be initiated. The connection of individual components is displayed in Figure 30.

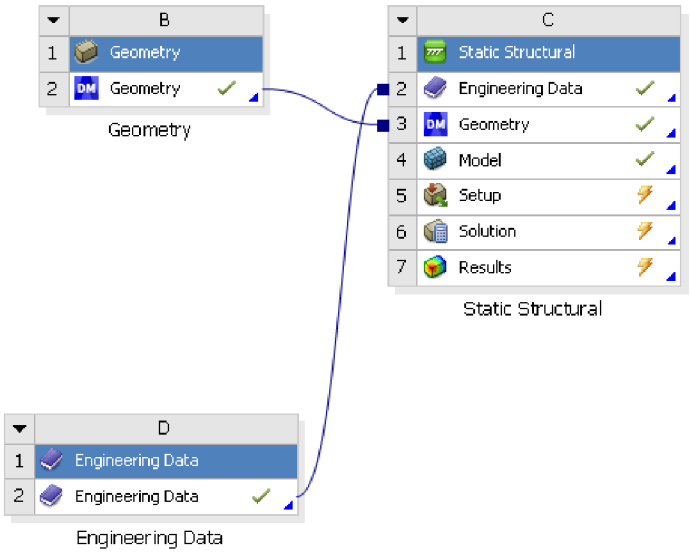

Figure 30 - Workbench layout for structural analysis

Solid model is divided into two parts – one consisting of intima, fibrous cap, and lipid core, and the other consisting of media and adventitia. These two parts are then connected using the bonded contact, as per [54]. Due to the nature of arteries, both ends are then allowed only to move in the radial direction (x direction in a cylindrical coordinate system), as displayed in Figure 31. To achieve better visibility, solid models are further mostly displayed in a plane cut.

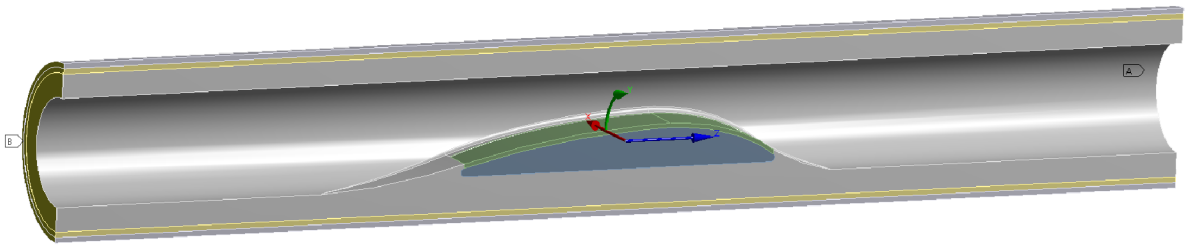

Figure 31 - Boundary conditions of the solid model

Prior to proceeding with the FSI analysis, convergence of the solid (as well as fluid, discussed later) model has to be achieved. This is why a structural analysis with a constant pressure applied to all inner surfaces is performed. Proceeding to FSI analysis, this boundary condition will be changed to a *Fluid-Structure Interface* condition. The value of pressure is chosen as approx. the highest value present in ICA measurement displayed in Figure 15, which will further be used in the FSI analysis, and its value is:

$$p = 15\,000\ Pa$$

Another alternative to creating a cylindrical coordinate system and assigning both ends with allowed radial displacement is a cylindrical support used on the entire outer wall of the artery (assigning radial displacement to the entire outer surface). Both options were analyzed and provided no significant differences, but the first option resulted in more realistic deformed shape. This is why the first option is used throughout this thesis. Cylindrical support setup is displayed in Figure 32.

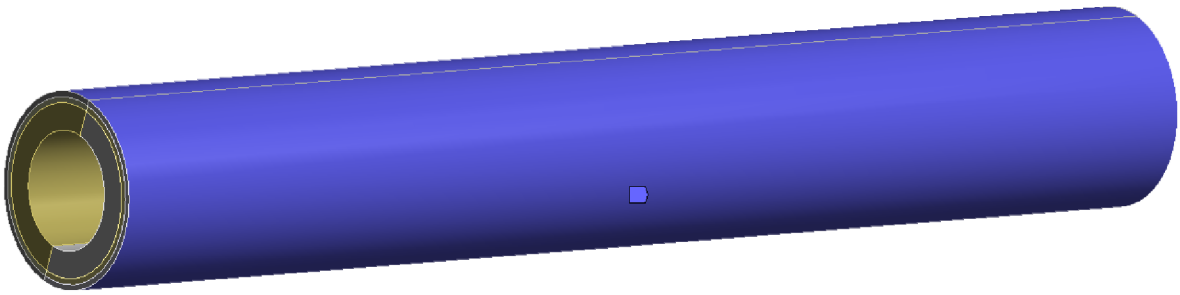

Figure 32 - Cylindrical support

One more boundary condition to be considered is axial pretension. This boundary condition is omitted, as it makes the model highly unstable and difficult to converge. Also, axial pretension generally decreases with age and atherosclerosis is typical with older people. Some analyses of this type also require an elastic support to be assigned, mainly to increase stiffness and to help with initial convergence problems. This boundary condition is also omitted in this thesis. Since we are working with nonlinear hyperelastic materials, large deformations have to be turned on in analysis settings.

Solid is meshed in the proprietary *Ansys Workbench Mechanical* environment. Element type used for this model is the quadratic hexahedral element SOLID186. This element is a higher-order 3D solid element that exhibits quadratic displacement behavior. It is defined by 20 nodes, each of which has three degrees of freedom [60]. Due to the complexity of the model, it also consists of a few tetrahedral SOLID187 elements. Both element types are displayed in Figure 33.

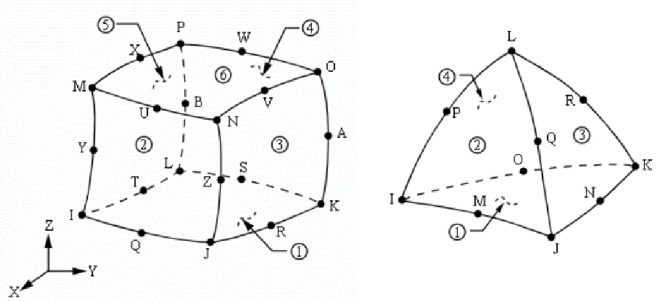

Figure 33 - SOLID186 (left) and SOLID187 (right) elements [60]

3.1.4 Result Independence on Mesh

To achieve sufficient mesh density in the model, result independence on mesh check is performed on 3 different models, with finer mesh being focused mainly on stress-concentration regions. Mesh count and resulting maximal principal stresses are displayed in Table 3. Comparison of results and critical areas is then displayed in Figure 34.

Table 3 - Structural mesh comparison

Model	Element count	Maximum principal stress $[MPa]$	Difference to previous $[\%]$
Coarse mesh	31 503	0.0663	-
Finer mesh	43 073	0.0698	5.3
Finest mesh	55 356	0.0724	3.7

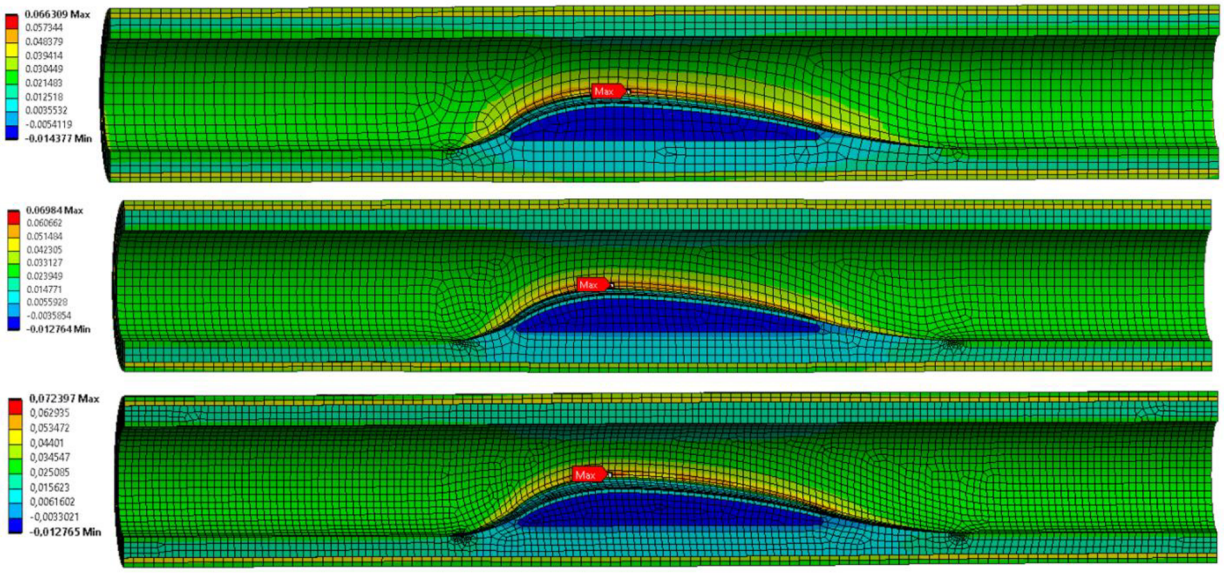

Figure 34 – Obtained maximum principal stress. From top to bottom: coarse mesh, finer mesh, finest mesh. Results are in [MPa].

Since the differences between maximum principal stresses and critical locations are below 5% for the last two mesh densities, mesh was not further refined, and the last mesh is further used throughout all additional solid models. Default mesh sizes are then: 0.5mm for media and adventitia, 0,35mm for fibrous tissue and lipid core, and 0.1mm at the ends of the plaque, mainly due to convergence issues. Media and adventitia are then meshed using the Sweep method, whereas lipid core, intima, and fibrous cap are meshed using the Hex Dominant method.

3.2 Fluid Model

This chapter describes the process of performing an isolated fluid analysis. However, the subsequent FSI analysis has some specific requirements to run successfully. As these requirements take part mostly in the fluent setup, they are also described in this chapter.

3.2.1 Idealized Geometry Model

Analogically to solid, fluid model is created in the *Ansys* proprietary *Design Modeler* environment. Once solid part was created, full fluid cylinder was simply subtracted from it and its final representation is displayed in Figure 35.

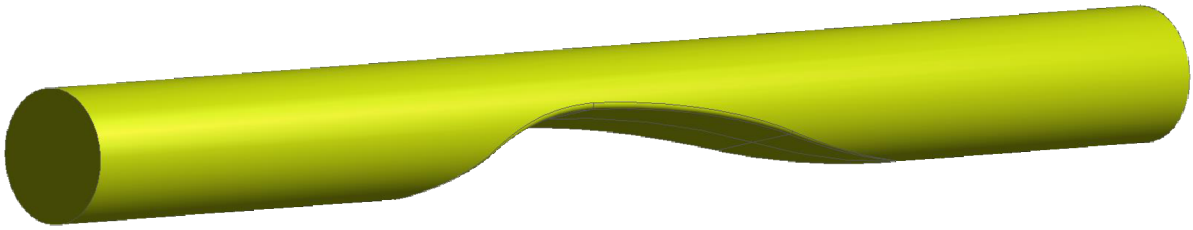

Figure 35 - blood geometry model for a 50% stenosis

3.2.2 Fluid Meshing in ICEM CFD

Meshing of the fluid model is performed in the *ICEM CFD* software. Even though Ansys Fluent also disposes with a meshing environment, *ICEM CFD* provides with better capabilities regarding element types and inflation options, which are both crucial parameters for this analysis. After importing the model, parts *INLET*, *OUTLET*, and *WALL* are created, along with a body *BLOOD*, so that these components could be further referenced in analysis setup. Imported model, along with the created components, is displayed in Figure 36.

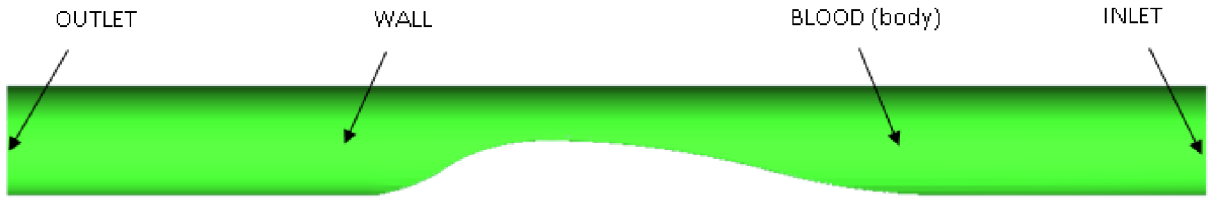

Figure 36 - Fluid model in ICEM CFD with individual components

Before fluid mesh can be computed, model has to be divided into blocks, since the geometry is too complex to be meshed automatically. These blocks have the shape of deformed rectangles and have to be created in a manner, so that they roughly represent the initial geometry. After they are created, their edges are internally connected to the geometry and mesh is afterwards created as a projection of elements from these rectangles to a given geometry subregion. This block o-grid is displayed in Figure 37.

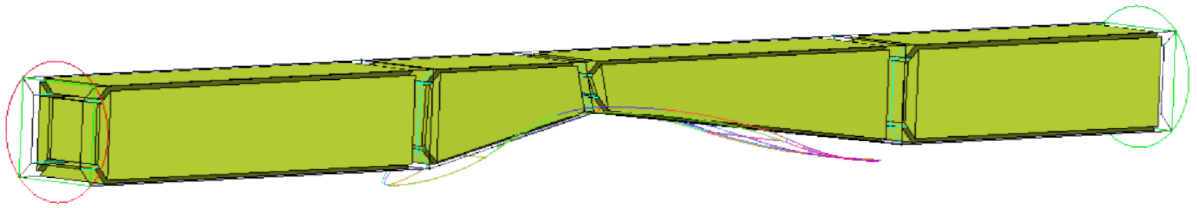

Figure 37 - o-grid blocks in ICEM CFD

Once blocking is finished, meshing process can be initialized. Individual block edges are assigned a certain number of nodes, with edges, going from the blood surface inwards, also being assigned an inflation parameter of 1.2, with the first layer being approx. 1/100 of the diameter. This is used so that high changes in gradient can be captured in fluid analysis. The number of inflation elements used in this analysis was chosen as 6. Element type used for this model is the quadratic hexahedral element and the total number of elements is approx. 85 000. Initial computed mesh in the entire model and in two perpendicular planes is displayed in Figure 38.

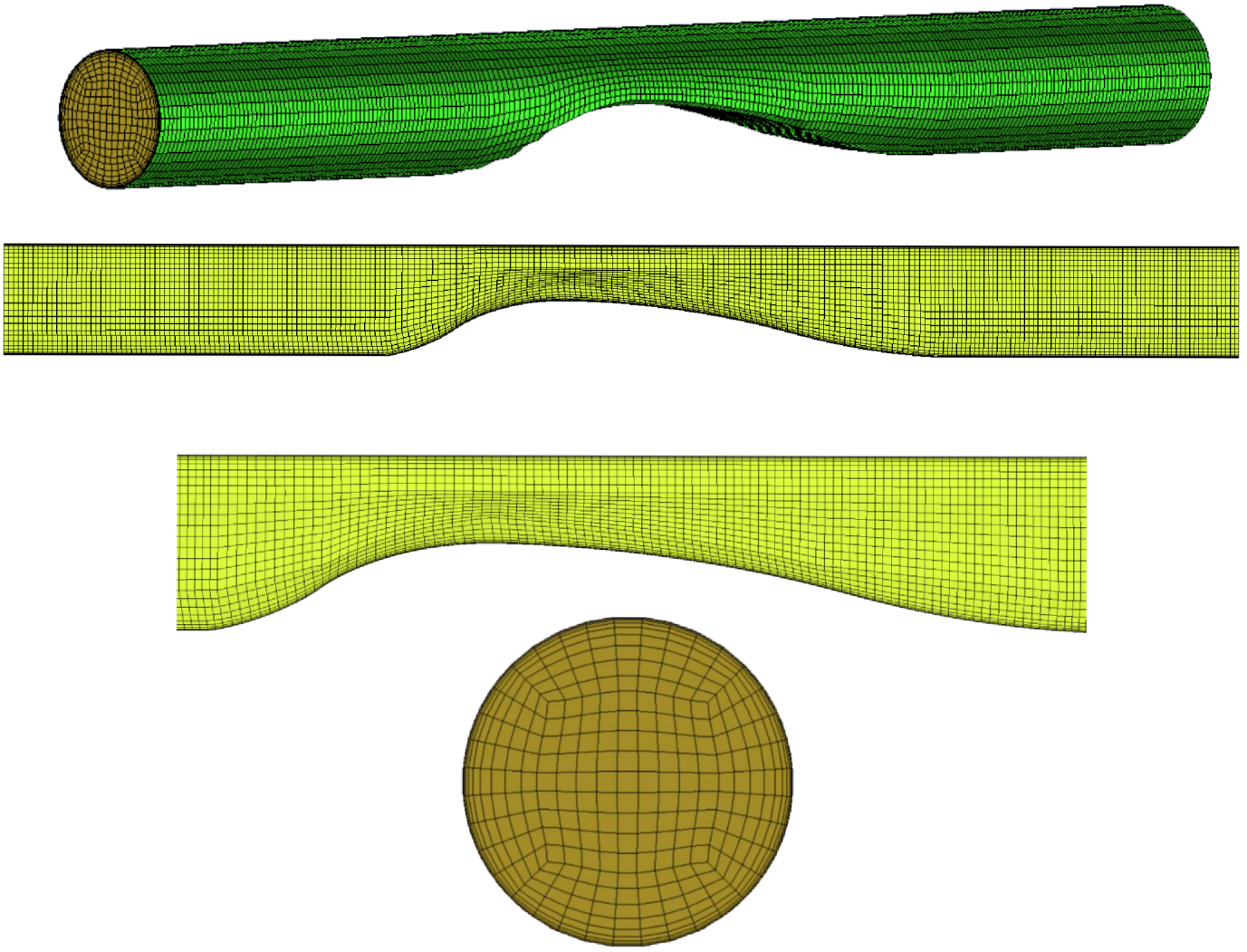

Figure 38 - Fluid mesh obtained from ICEM CFD, from different perspectives. From top to bottom: whole body, section cut of the whole body, closeup on the section cut, cross section

3.2.3 Fluent Setup

After meshing is completed, *ICEM CFD* system component is then copied into *Setup* of the *Fluid Flow* component. In here, boundary conditions and solver methods can be applied. The connection of individual components in displayed in Figure 39.

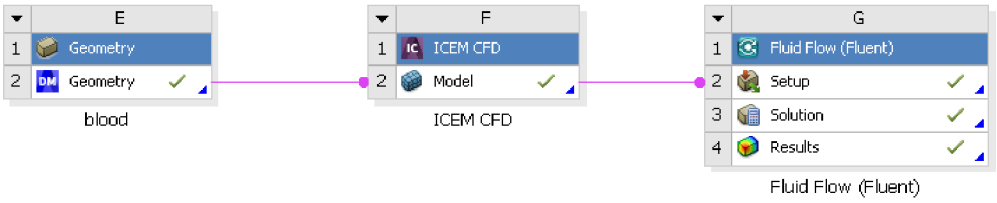

Figure 39 - Workbench layout for fluid analysis

Boundary conditions of the fluent analysis are represented by two waveforms, taken from [32], and represent blood mass flow and blood pressure. After several iterations, it was decided to assign pressure to the *INLET* part and mass flow to the *OUTLET* part, mainly because of better convergence. Used waveforms are displayed in Figure 40. Presented flow rate waveforms describe both IC (internal carotid) and EC (external carotid); this thesis further only uses the IC waveform.

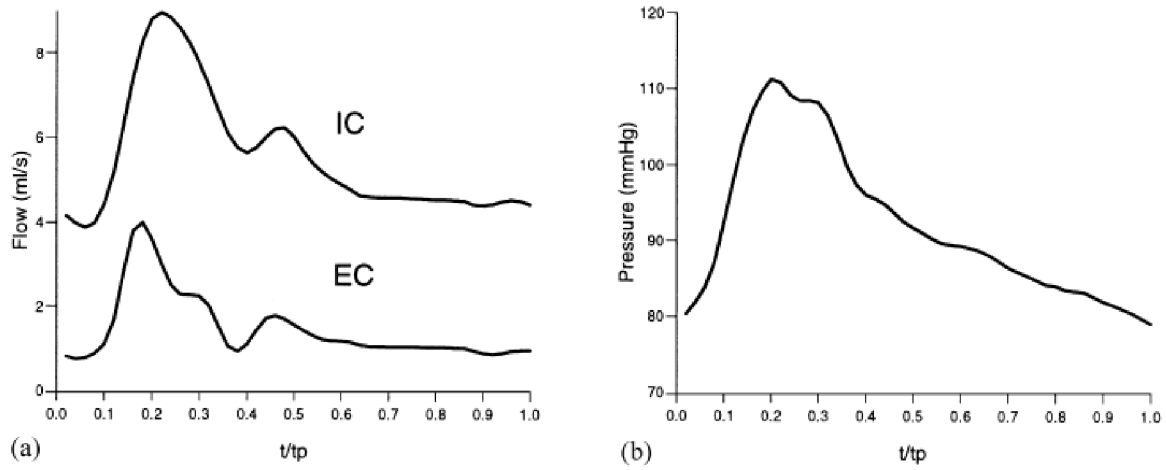

Figure 40 - Flow and pressure waveforms in the Carotid artery. Taken from [32]

In order to obtain the specific values of both characteristics, these waveforms were first imported to *WebPlotDigitizer* (WPD), which is a freeware software used to digitize data from pictures [61]. After an image is imported, we adjust the X-Y axes, so that the program knows the range of each coordinate. After that, a mask is created over a given curve, density of data points is specified, and the program calculates the coordinates of each point. This dataset can then be downloaded as a .CSV file to further work with. Example of this process for the pressure wavelength, along with digitization specifics, is displayed in Figure 41. This figure also shows that the time step chosen for this analysis is $\Delta t = 0.01s$. This value is the result an iterative process, considering the representative value of obtained data and the computational power available. Smaller time step would improve the quality of the results but is not feasible with the hardware used, specified later in this thesis.

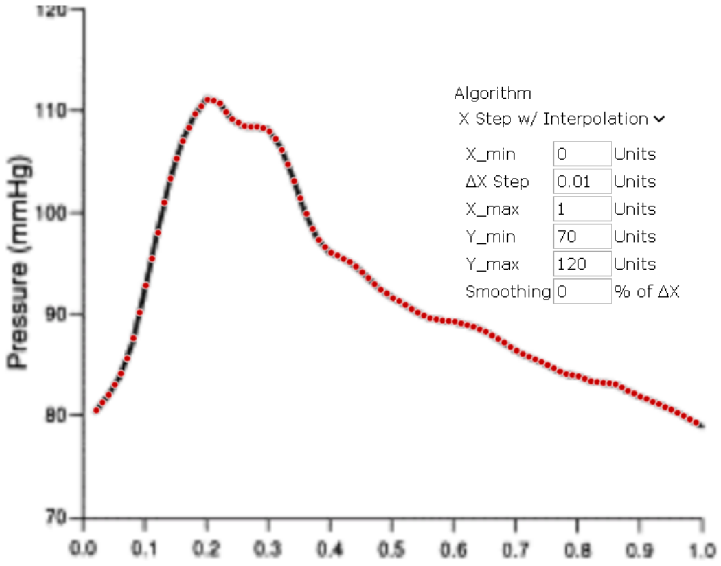

Figure 41 - Data digitization in WebPlotDigitizer

When focusing on pressure, data in Figure 40 is in $[mmHg]$, meaning we have to convert it to a unit suitable for a fluid analysis in Ansys, which is $[kPa]$. As mentioned in subchapter 2.5.2, this conversion formula is:

$$1mmHg = 0.133kPa$$

and is applied on all datapoints obtained from WPD. Concerning flow rate, data in Figure 40 is in $[ml/s]$ and applied mass flow has to be in $[kg/s]$. To convert this unit, we have to multiply flow rate by 10^{-6} to get to $[m^3/s]$ and then multiply this by blood density to get to $[kg/s]$. Since the density of blood is $\rho = 1060\ kg/m^3$ [36], the final conversion formula is:

$$1[ml/s] = 10^{-6} \cdot 1060[kg/s]$$

It has been observed that the number of waveforms entering the FSI analysis can generally impact the resulting values. This is why we use two consecutive waveforms for both, pressure, and mass flow, to enter fluid analysis. Using even more time periods would be ideal (some studies even use more than 3 periods), but this thesis is limited by the computational power available, and more than two periods would pose a significant increase in the time needed to perform these analyses; more on this issue in the following subchapters.

As mentioned earlier, pressure waveform is used on the *INLET* surface of blood. The exact dataset is displayed in Figure 42. We can see that in the first second, pressure is steadily increasing from the initial value of $10^{-8}kPa$. This is because had the analysis started at a higher value, it would lead to serious disruptions in the solid domain during the FSI analysis, causing the calculation to fail. The transition from manually assigned values to the data obtained from literature is highlighted with a red line at $t = 1s$. The value of initial pressure has to generally be very low, and is most commonly zero or very close to zero.

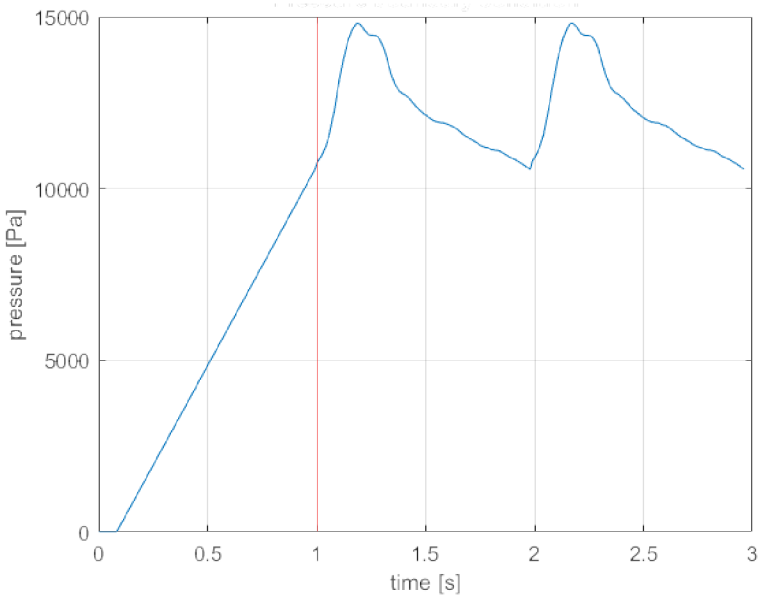

Figure 42 – Inlet pressure boundary condition

High increase of pressure in the first second of FSI analysis causes the artery to expand rapidly in its diameter. If not prevented, this expansion would induce a suction in other parts of the artery. To counter this effect, a suitable sufficient initial value of mass flow has to be assigned before applying the dataset obtained from literature. The value of initial mass flow is highly case-specific and has to be obtained as a result of an iterative process. The value used in this thesis is $\dot{m} = 0.0406 kg/s$ for the first $0.3s$ of the analysis. After this time, the value steadily decreases to meet the mass flow waveform at $t = 1s$. The final mass flow dataset is displayed in Figure 43.

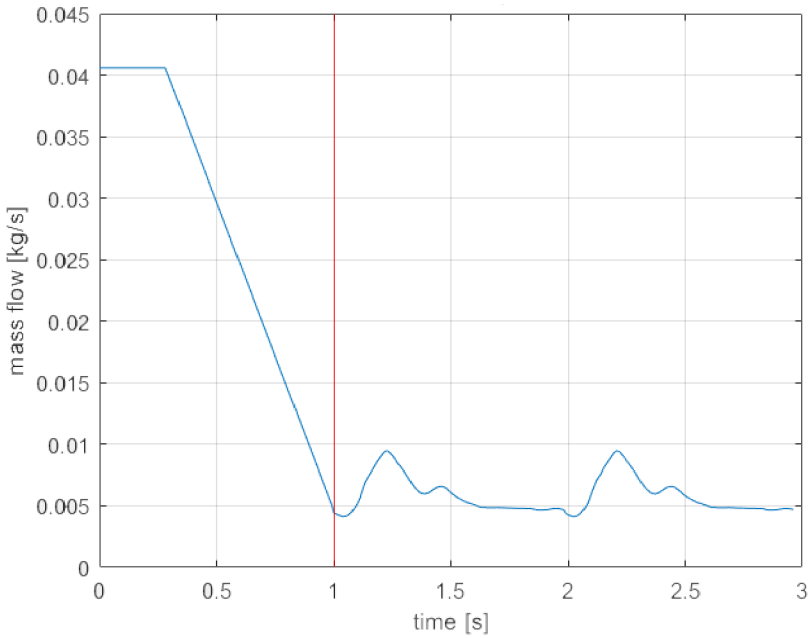

Figure 43 – Outlet mass flow boundary condition

Apart from assigning pressure (inlet) and mass flow (outlet) boundary conditions, blood surface is set as a *Stationary Wall* with a *No Slip* condition. During FSI analysis, this surface is assigned as a *System Coupling* zone for data transfer.

As far as solution method for the fluid analysis is concerned, used formulations are most often a result of an iterative process. Higher order formulations can generally increase the precision of results but can also highly disturb convergence. The scheme used for most of the analyses in this thesis is displayed in Figure 44. Apart from the formulations displayed below, calculations are run using the *Second Order Implicit Transient Formulation*. All calculations are initialized using *Hybrid Initialization* and the analysis type is set as *Transient*.

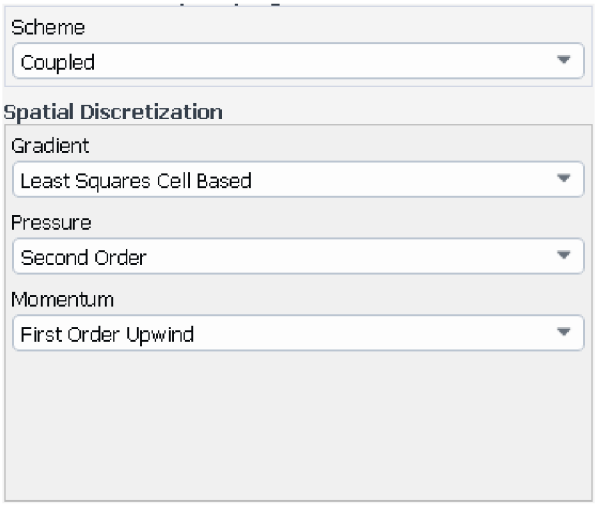

Figure 44 - Fluent solution methods

3.2.4 Material Model

Blood is modelled as a laminar, non-Newtonian, incompressible fluid. As mentioned in chapter 2.6.2.5, material model of blood used in this thesis is the Carreau-Yasuda model, more specifically one of its versions, the Bird-Carreau model, along with a specified blood density. This model differs from the original with the value of power law index being set as $a = 2$. The general Carreau-Yasuda model formula can then be written as:

$$\eta(\dot{\gamma}) = \eta_\infty + (\eta_0 - \eta_\infty) \cdot [1 + (\lambda\dot{\gamma})^2]^{\frac{n-1}{2}} \tag{37}$$

Specific values of this model were then taken from [62] and shown in Table 4.

Table 4 - Carreau-Yasuda model parameters

Variable	Unit	Value
η_∞	$[Pa \cdot s]$	0.0035
η_0	$[Pa \cdot s]$	0.056
λ	$[s]$	3.313
n	$[-]$	0.3568
ρ	$[kg \cdot m^{-3}]$	1060

3.2.5 Result Independence on Mesh

Analogically to the solid model, result independence on mesh check is performed in order to eliminate inaccuracies as a result of poor mesh quality. 3 different fluent analyses are calculated with 3 different mesh densities and a chosen variable is observed to find out how much do the result differ. Individual mesh counts are displayed in Table 5. Figure 45 shows the 3 different calculated cases and Figure 46 the location in which the velocity profiles were compared.

Table 5 - Fluid mesh comparison

Case	Elements over diameter	Elements in total
1	21	approx. 65 000
2	27	approx. 85 000
3	42	approx. 130 000

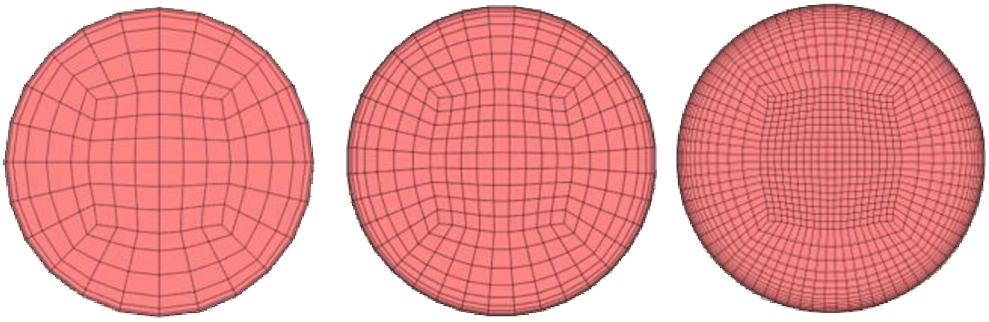

Figure 45 - Mesh size comparison; case 1-3 from left to right

Figure 46 - Location of compared values for convergence study, shown as an orange line, the location of which is about half a millimeter above the narrowest point of the stenosis and parallel to highlighted surfaces

As displayed in Figure 47, the difference in velocity profiles in a given location (see Figure 46) is negligible (below 5%). For the purposes of this thesis, the number of elements over diameter is hereinafter set as 27.

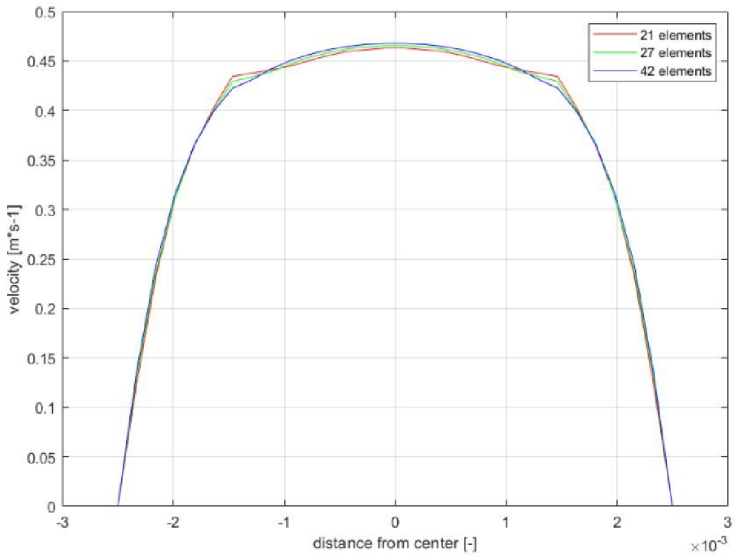

Figure 47 - Velocity profile comparison of different mesh densities in a specified location

3.3 Fluid-Structure Interaction Analysis

Chapters 3.1 and 3.2 discuss two isolated objects – solid and fluid model. They are solved using different computational methods (*Finite Element Method* [FEM] in solid versus *Finite Volume Method* [FVM] in fluid) and do not influence each other in any way. If, however, we truly want to understand the impact of a pulsatory blood pulse on the arterial wall, a different kind of approach has to be used; a method which connects the fluid solver (*Computational Fluid Dynamics* [CFD]) with the structural solver. The method in question is called *Fluid-Structure Interaction* (FSI) analysis.

We can generally distinguish between three FSI types:

- Rigid body FSI analysis – we assume no deformations in the solid domain (rigid bodies). This analysis can be done for fixed rigid bodies; no data transfer is needed.
- One-way FSI analysis – resulting forces in the fluid domain are used as a boundary condition for structural analysis. This approach assumes very small deformations in the structure, so that it does not influence the fluid flow.
- Fully coupled FSI analysis – as the solid domain deforms (result of loading by the forces from the fluid domain), these deformations are sent back to the fluid domain and cause it to deform and reshape as well; suitable for large structural deformations [60].

We further limit ourselves to the last 2 types. While theoretically more precise, fully coupled FSI analysis often requires much more computational power and is not always feasible. This is why this thesis aims do to both, one-way and fully coupled analysis, to try and assess the pros and cons of both.

If we take a look at FSI in greater detail, we can also distinguish between explicit and implicit approach. Dissimilarly to explicit/implicit FEM algorithm, the difference in these two FSI approaches is in how important the dependency of solid and fluid is. If the dependency is significant, which is our case, implicit approach is used, which presumes that domains and their data transfer might not converge during one iteration, and thus solves them iteratively [63]. This algorithm is also the one embedded into Ansys Workbench.

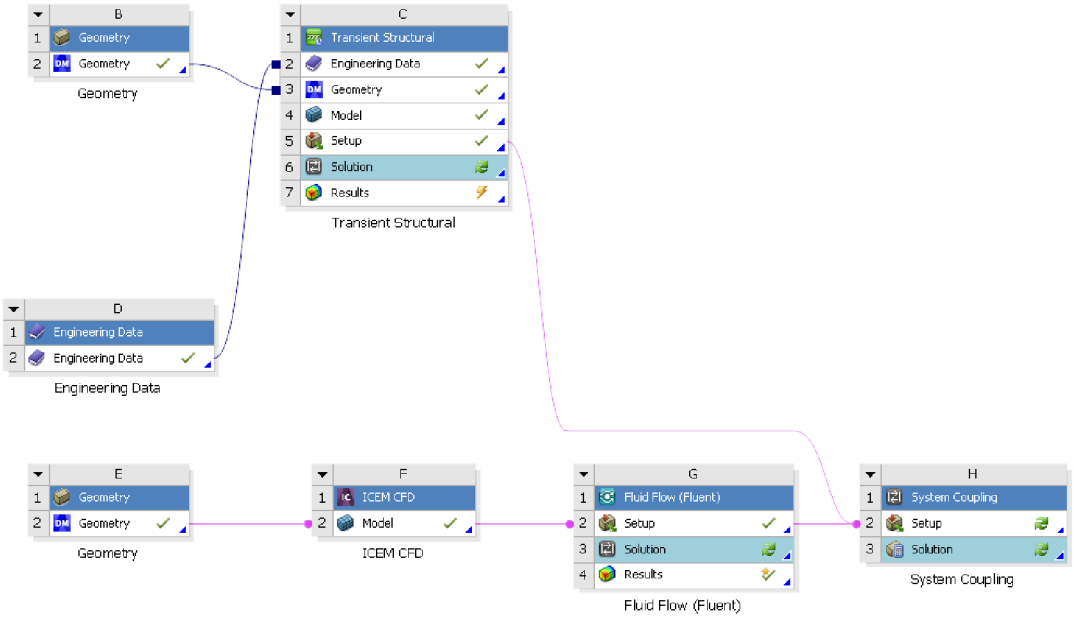

Figure 48 - Workbench layout for FSI analysis

Figure 48 shows the connections for all necessary component systems participating in FSI analysis. Once we connect both *Transient Structural* and *Fluid Flow (Fluent)* to *System Coupling*, and update both of the setups (this process transfers all the necessary information into the *System Coupling* setup), we can proceed into the setup of the FSI analysis itself. Here, we define *End Time* and *Time Step* of the simulation. It is crucial that the end time value corresponds with the value assigned in *Transient Structural* component, and that the time step value corresponds with the value assigned in *Fluid Flow (Fluent)* component; otherwise, simulation will not run correctly. In our analysis, these values are: $End\ Time = 2.961s$ and $Time\ Step = 0.01s$. We also create two data transfers; from Fluent to Mechanical and vice versa. In case of a one-way FSI analysis, data transfer from Mechanical to Fluent is suppressed and coupling only occurs from *WALL* (fluid surface) to *Fluid-Structure Interface* (inner artery wall). One additional alteration is in the *Coupling Engine*; as this particular analysis is highly unstable, we use the 1.0 version of this engine, which allows us to first calculate Fluent and then Mechanical, so as to help with convergence issues during the initial time steps. *Maximum Iterations* value is set to 10.

3.3.1 Fully Coupled Analysis Setup

As mentioned in the previous chapter, data transfer from solid to fluid is suppressed during one-way FSI analysis. If we therefore want to run a fully coupled simulation, we have to unsuppress this transfer. Since the deformation of solid now directly influences fluid, *Dynamic Mesh* has to be enabled in the fluid setup, so that it can reshape appropriately.

The method chosen for reshaping in this thesis is *Smoothing*. For large deformations, this method is usually used alongside *Remeshing*. Remeshing, however, is not supported for hexahedron elements used in this thesis for the fluid domain which is why it is omitted [60]. Method is then applied to the *INLET* and *OUTLET* part of blood, both also assigned with the *Deforming* type.

Smoothing method moves interior nodes to absorb the motion of a moving and/or deforming boundary. This means that the number of nodes and their connectivity does not change throughout the simulation. It is available both in 2D and 3D, and offers three different smoothing sub-methods: *Spring smoothing, Diffusion smoothing,* and *Linearly elastic solid smoothing*. This thesis is using *Diffusion smoothing*. Defined parameters of *Dynamic Mesh* are displayed in Figure 49.

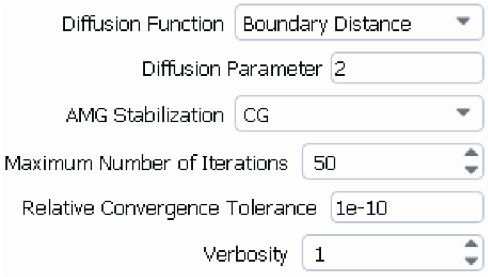

Figure 49 - Dynamic mesh setup

Specific values shown in Figure 49 are the result of an iterative process and cannot be applied generally. The most case-specific parameter is probably the *Diffusion parameter* which tells the solver how should the elements close to the wall deform; value of 2 specifies that the elements closest to the wall should be preserved and displacements should be diffused out to the far-field mesh [60].

Another parameter adjusted in *Dynamic Mesh* setup is *Solution Stabilization*. This coefficient-based value helps prevent criterion values from oscillating, so that the analysis converges better. The range of specifiable values spreads from 0.01 to 100000 and can be necessary to alter for every slight adjustment in the model. For the referential analysis, this coefficient was iteratively tuned to achieve convergence of solutions and to ensure that the behavior is not overdamped. Finally, value of 0.1 was found to be suitable, and is applied on *Inlet*, *Outlet*, and *Wall* components.

3.4 Results

Before we proceed to the analysis of results, we must first define what particular characteristics and at which time step we want to evaluate and compare. If we take a look at the artery wall, we can compare maximum generated stresses and corresponding critical locations, as well as total deformation of the wall; all these in a structural, one-way FSI, and fully coupled FSI analysis. In case of blood, we will mainly focus on wall shear stress (WSS), time-averaged wall shear stress (TAWSS), and oscillatory shear index (OSI). All these characteristics are further defined in corresponding subchapters.

Apart from TAWSS and OSI, all variables are calculated individually for all time steps. Analyses in this thesis contain almost three hundred time steps, which is why we must define the most critical time point to evaluate the results; this point of interest will be the systolic pressure peak (see Figure 42). Since we are calculating two cardiac cycles, we must also distinguish between the two periods and the critical value of these two. For this comparison, we use the resulting maximum principal stress in the artery wall obtained from a one-way FSI analysis. This comparison is used as referential and is afterwards used for all the other results. Obtained stress results are displayed in Table 6.

Table 6 - Maximum principal stresses for both cardiac cycles

Cardiac cycle	Maximum principal stress $[kPa]$	Time $[s]$	Difference $[\%]$
1.	57.90	1.17	1.46
2.	58.76	2.17	-

Maximum principal stress was found at $2.17s$ (second cardiac cycle). Comparing this value to the first cycle ($1.17s$), we see a difference of 1.46%. Since the difference is insignificant, we can assume that the number of cardiac cycles used in this thesis is sufficient. Second cardiac cycle is also therefore used for all other relevant characteristics. Corresponding results are displayed in Figure 50.

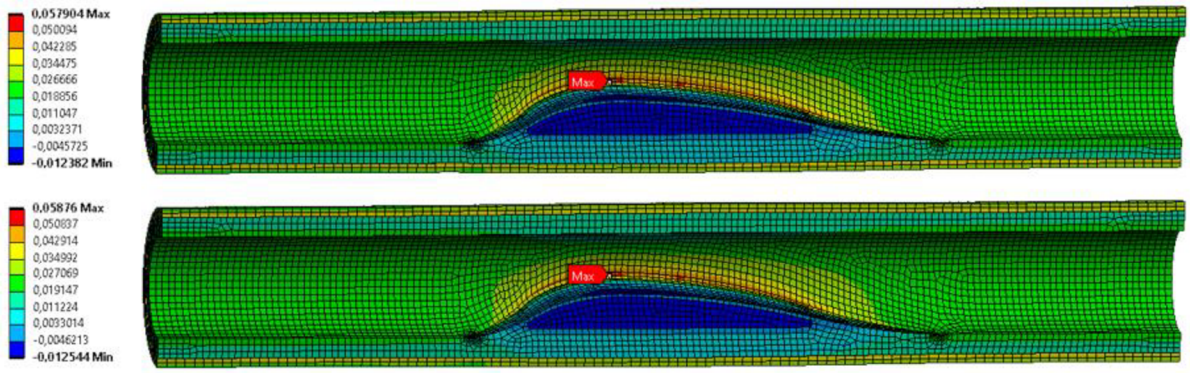

Figure 50 – Maximum principal stress comparison: 1.17s (top), 2.17s (bottom). Results are in [MPa].

The following subchapters contain the results and comparisons of all evaluated characteristics for individual analysis types.

3.4.1 Maximum Principal Stress

One of the risks connected to atherosclerosis is the possibility of a rupture in the artery wall. This is why we evaluate and compare maximum principal stresses and corresponding critical locations, and try to determine whether a simple structural analysis is sufficient for this type of prediction. Comparison of maximum principal stresses for structural, one-way FSI, and fully coupled FSI analysis is displayed in Figure 51, with the corresponding results displayed in Table 7. These, and all the following, results are displayed in a plane cut for better visibility. Results obtained from the other half of the model are almost identical to the ones displayed.

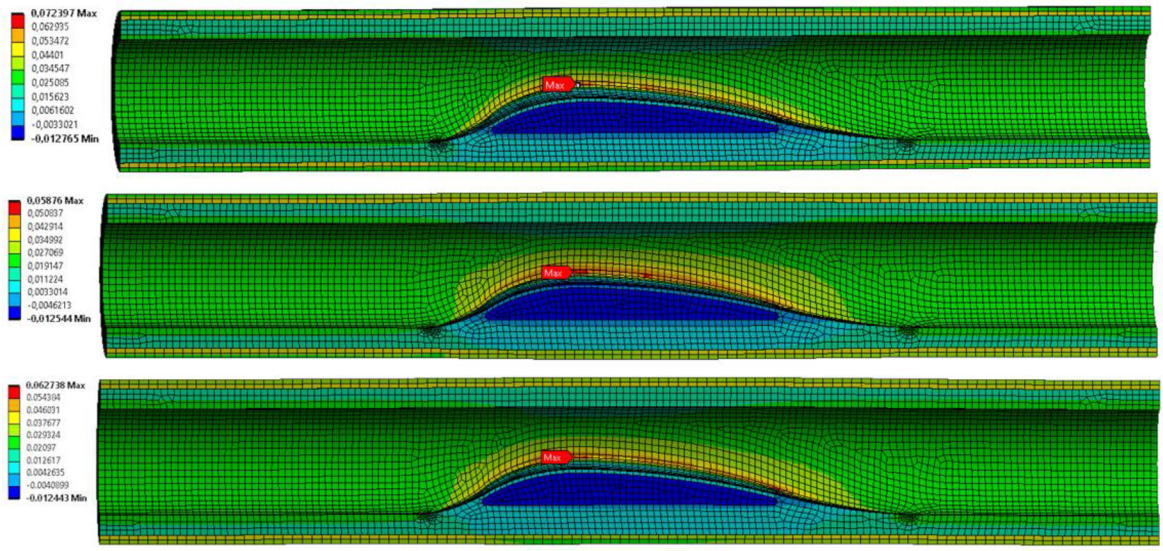

Figure 51 - Maximum principal stress comparison. From top to bottom: structural analysis, one-way FSI analysis, fully coupled FSI analysis. Results are in [MPa].

Table 7 - Maximum principal stresses for different analysis types

Analysis type	Maximum principal stress $[kPa]$	Difference $[\%]$
Structural	72.4	15.5
One-way FSI	58.8	- 6.2
Fully coupled FSI	62.7	-

If we assume that a fully coupled FSI analysis provides the most precise results and use it as referential, we can see that a simple structural analysis with a constant applied pressure overestimates the maximum principal stress by 15.5%, while a one-way FSI analysis, on the other hand, underestimates this value by 6.2%. As far as the critical location is concerned, all analyses predict the same result. Critical stress values are often considered as those higher than $300kPa$ which means that none of these cases should be critical for a rupture risk [54]. However, as this thesis contains multiple simplifications, discussed later, rupture risk is not the main criterion observed, rather than the difference between different analyses itself.

3.4.2 Total Deformation

As discussed in subchapter 3.1.3, ends of the artery wall are allowed to move only in the radial direction. This means that the model should be able to inflate and deflate correspondingly to the applied pressure. Maximal deformation is then expected to occur in the narrowest part of stenosis, as the lipid core present is highly compliant. Comparison of total deformations for individual analyses is displayed in Figure 52, with the corresponding results displayed in Table 8.

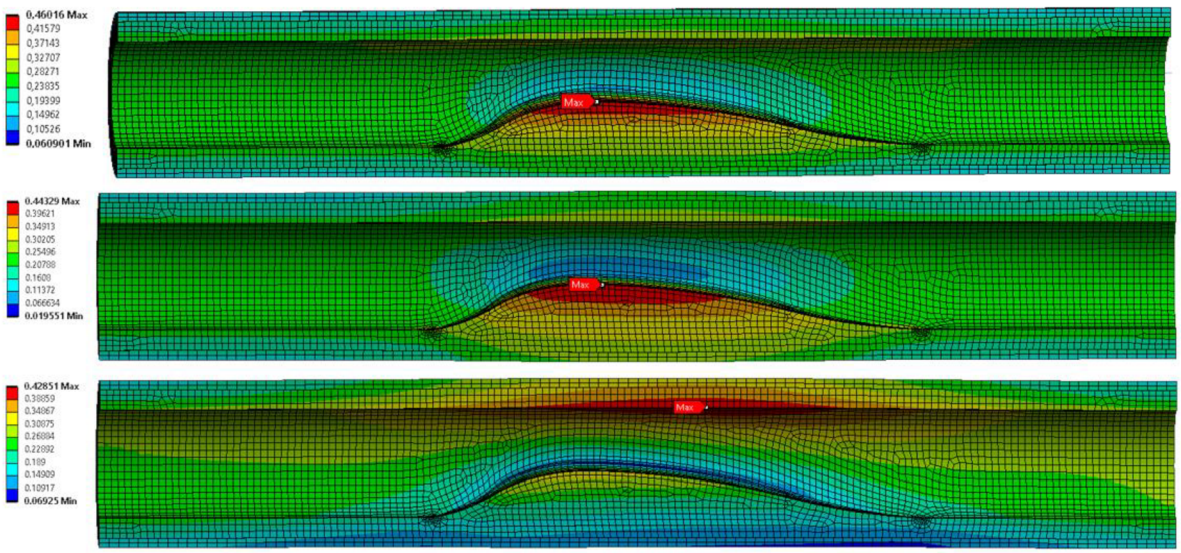

Figure 52 - Maximum structural deformation comparison. From top to bottom: structural analysis, one-way FSI analysis, fully coupled FSI analysis. Results are in [mm].

Table 8 - Total deformation for different analysis types

Analysis type	Total deformation $[mm]$	Difference $[\%]$
Structural	0.46	6.9
One-way FSI	0.44	2.3
Fully coupled FSI	0.43	-

Again, fully coupled FSI analysis is used as referential, for it bears the highest complexity. Although the difference in results is lower than with maximum principal stress (2.3% for one-way FSI and 6.9% for structural analysis), we observe a difference in the critical area in a fully coupled FSI analysis compared to the rest. During a fully coupled FSI analysis, fluid mesh is dynamic, rather than static or non-existent with the rest of the analyses, and is reshaped accordingly to the displacement values obtained from a corresponding data transfer which will most likely influence the nature of blood flow. This is why such difference can be observed. To verify that the majority of displacement occurs only in the radial direction, we also evaluate radial deformation (X axis in the cylindrical coordinate system displayed below). This displacement for a fully coupled FSI analysis is displayed in Figure 53.

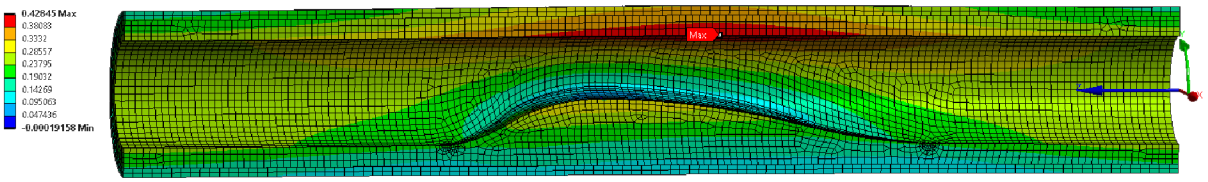

Figure 53 - Radial displacement from a fully coupled FSI analysis. Results are in [mm].

3.4.3 Wall Shear Stress

Wall shear stress is the drag exerted by flowing blood on the vessel wall and it is mainly dependent on the flow speed in a given area. As far as atherosclerosis is concerned, this characteristic is used to predict the initialization and subsequent growth of the atherosclerotic plaque. If the WSS value is in the long term lower than $0.4Pa$, it leads to a disruption in the endothelial layer, allowing substances like cholesterol, fats, and cellular waste to accumulate there [64] [65].

In we want to calculate WSS, the following formula applies:

$$|WSS| = |n_i \cdot \tau_{ij}| \tag{38}$$

where τ_{ij} is the viscous stress tensor $[Pa]$ and n_i is the surface normal vector $[-]$ [65]. Comparison of WSS in range up to $0.4Pa$ for different analysis types for a given time step (systolic pressure in the second period) is displayed in Figure 54.

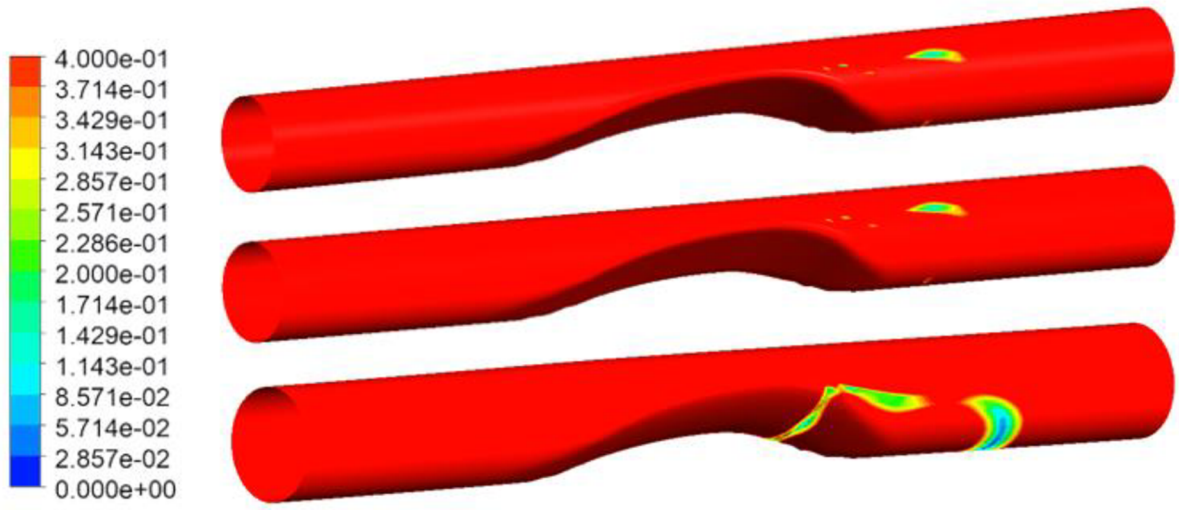

Figure 54 - WSS comparison for different analysis types. From top to bottom: fluid flow analysis, one-way FSI analysis, fully coupled FSI analysis. Results are in [Pa].

If we look at the comparison above, we can see that the results obtained from fluid flow and one-way FSI analyses are close to, if not, identical. We can assume that the reason for this is that during both of these analyses, fluid mesh remains consistent and does not change in any way, nor is it influenced by the solid structure in any way. During a fully coupled FSI analysis, however, fluid mesh is dynamic, and changes correspondingly to how the structural mesh is deformed. This is why results obtained from a fully coupled FSI analysis are the most realistic. As far as critical values are concerned, this phenomenon is further discussed when comparing TAWSS values, since we are more interested in the long term values, rather than the WSS values from a certain time point. Only one side of the model is displayed for all of the results, because the other side shows identical values.

3.4.4 Time-Averaged Wall Shear Stress

Previous subchapter specifies that as far as wall shear stress is concerned, we are more interested in a time-averaged value of this characteristic, rather than the immediate value. This is why we also calculate time-averaged wall shear stress (TAWSS). It represents the magnitude of WSS vector averaged over a certain time period, and can be calculated as:

$$TAWSS = \frac{1}{T} \cdot \int_0^T |WSS| dt \tag{39}$$

where T is the cardiac cycle period [65].

Although newer versions of Ansys are capable of calculating this characteristic using the *Data Sampling* option in Fluent (starting from version 19.1., to be specific), this option does not allow us to calculate oscillatory shear index (OSI), discussed in the following subchapter. Since we have to extract data from Fluent to calculate this characteristic either way, both TAWSS and OSI are calculated separately in Matlab, using data extraction. To briefly describe this process, WSS values for all points in the model are extracted for all time steps during the second period of the cardiac cycle. These values are then imported to Matlab and used to calculate both, TAWSS and OSI, using the formulas defined in this thesis. Lastly, these results are then imported to Ansys proprietary CFD Post software for display. Obtained results of TAWSS for all compared analysis types in range up to $0.4Pa$ are displayed in Figure 56.

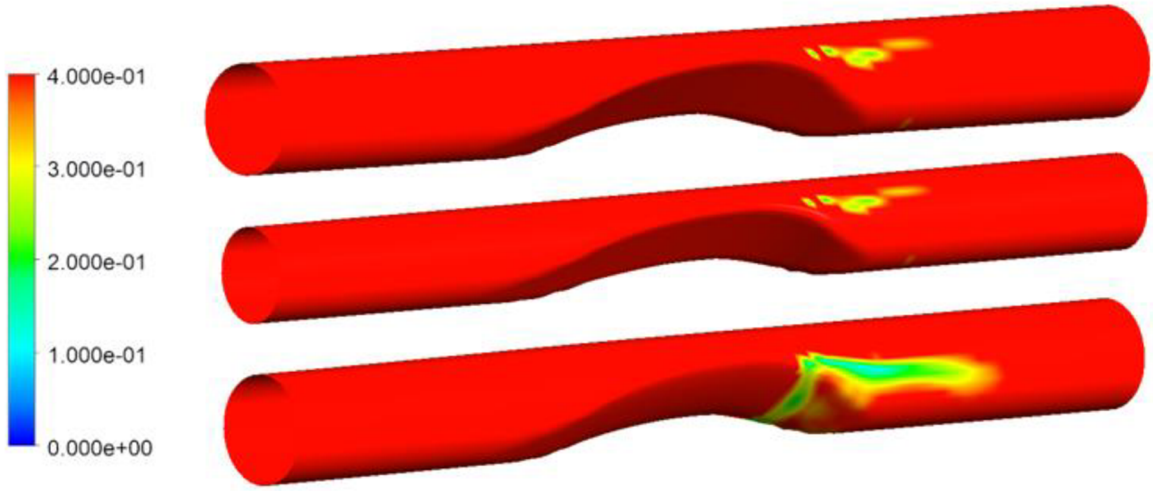

Figure 56 - TAWSS comparison for different analysis types. From top to bottom: fluid flow analysis, one-way FSI analysis, fully coupled FSI analysis. Results are in [Pa].

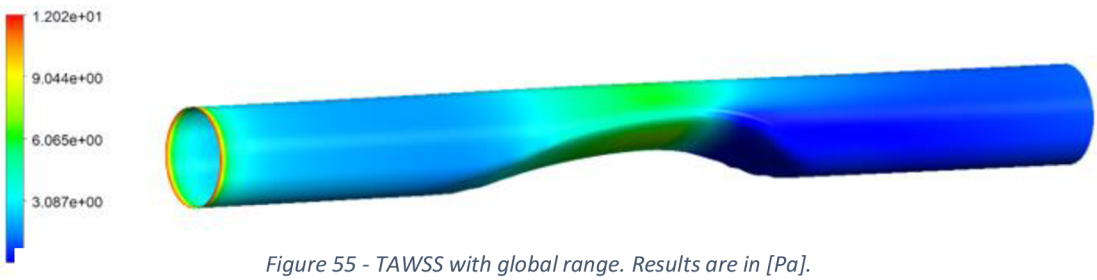

Figure 55 - TAWSS with global range. Results are in [Pa].

We also include a picture of obtained TAWSS with global range scaling, displayed in Figure 55. It demonstrates how wall shear stress gradually decreases and reaches its minimum right after the atherosclerotic plaque. Similarly to the results displayed in Figure 54, TAWSS values in Figure 56 are again identical for fluid flow and one-way FSI analyses. Although the results from these two analyses show some resemblance to a fully coupled FSI analysis, the differences are significant, and only a fully coupled FSI analysis should therefore be used when predicting critical TAWSS locations. Since the colormap used is set to display results from 0 to $0.4Pa$, we can clearly observe critical areas in our model. These are most likely to accumulate foreign substances and allow the atherosclerotic plaque to grow further. As TAWSS is a characteristic that is averaged over several time steps, a comparison of WSS for three different pressure values, and TAWSS from a fully coupled FSI analysis, in range up to $0.4Pa$, is also included. This comparison is displayed in Figure 57.

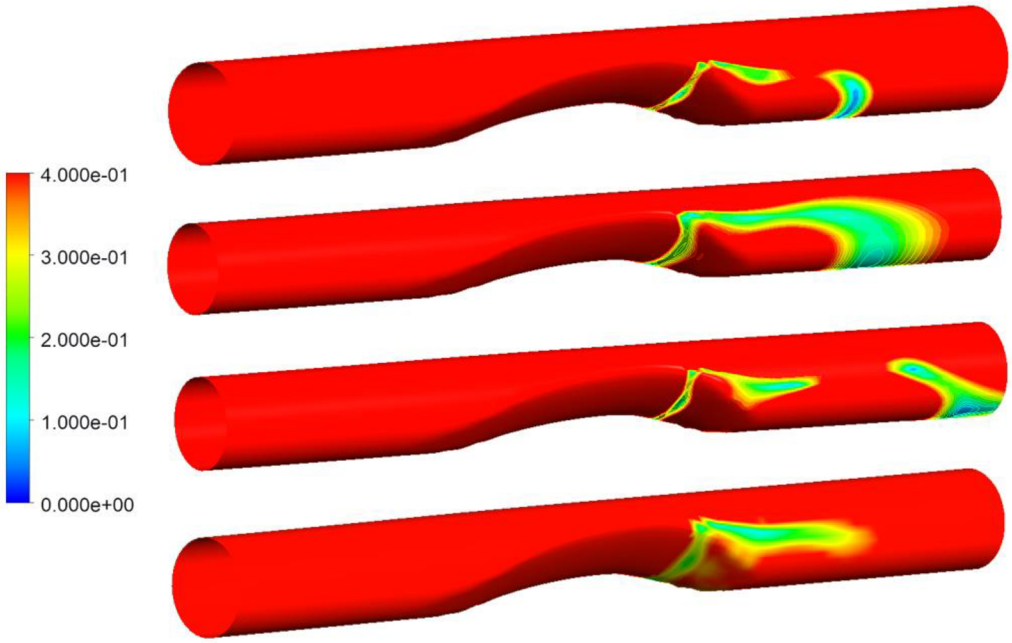

Figure 57 - Comparison of WSS and TAWSS. From top to bottom: WSS for systolic pressure, WSS for diastolic pressure, WSS for a given pressure between systolic and diastolic, TAWSS. Results are in [Pa].

3.4.5 Oscillatory Shear index

Oscillatory shear index (OSI) is a scalar variable that is used to evaluate the oscillatory nature of vascular flows. It can be calculated as:

$$OSI = \frac{1}{2} - \left(1 - \frac{\left| \int_0^T WSS dt \right|}{\int_0^T |WSS| dt} \right) \tag{40}$$

and it is a non-dimensional variable. OSI varies between 0 and 0.5, with 0 characterizing regions of unidirectional flow and 0.5 characterizing fully oscillatory flow regions [65]. When calculating this variable, corresponding data is processed in the same manner as TAWSS. Obtained results for all analysis types in range up to 0.5 are displayed in Figure 58.

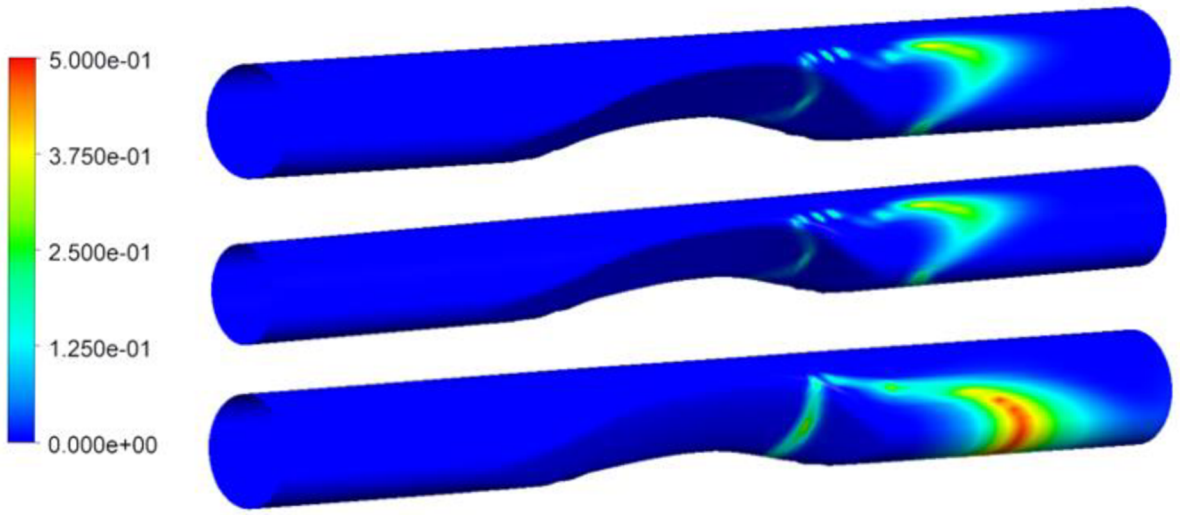

Figure 58 - OSI comparison for different analysis types. From top to bottom: fluid flow analysis, one-way FSI analysis, fully coupled FSI analysis. Results are in [-].

As seen with WSS and TAWSS, fluid flow and one-way FSI analysis provide us with identical results, while the differences between these and a fully coupled FSI analysis are again significant. By definition, higher OSI values can be seen in areas with oscillating WSS values. They are also often accompanied by low TAWSS values, and together they serve as indicators for atherosclerotic plaque growth [66].

3.4.6 Additional Evaluated Characteristics

On top of the aforementioned variables, pressure maps and velocity vectors are also evaluated for a fully coupled analysis. We evaluate these so as to understand the nature of pressure and velocity distribution throughout the artery. Since the used boundary conditions are not stationary, we evaluate the highest and lowest peaks of the applied pressure boundary condition (systolic and diastolic pressure). Resulting pressure maps on the artery wall are displayed in Figure 59, and velocity vectors for three plane cuts, along with the corresponding velocity streamlines, are displayed in Figure 60.

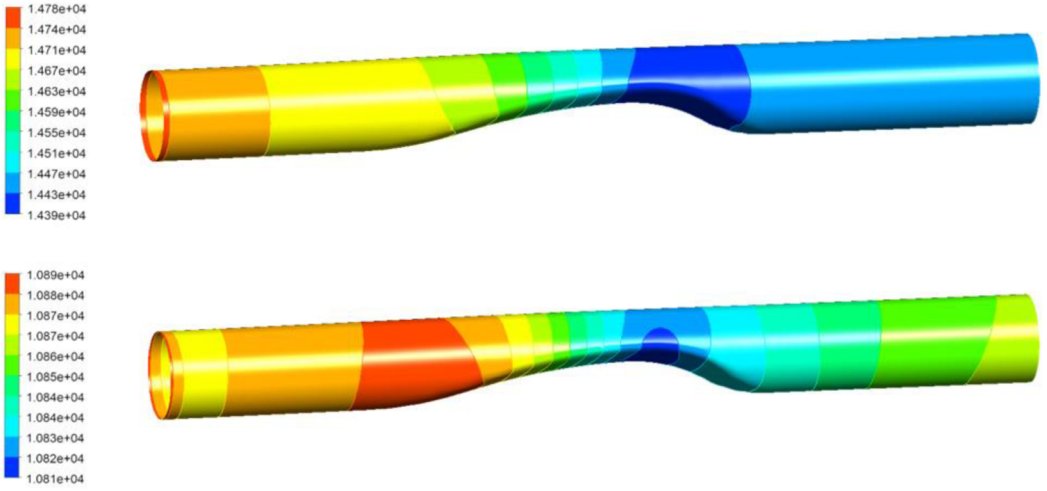

Figure 59 - Pressure profiles on the artery wall. From top: systolic pressure, diastolic pressure. Results are in [Pa].

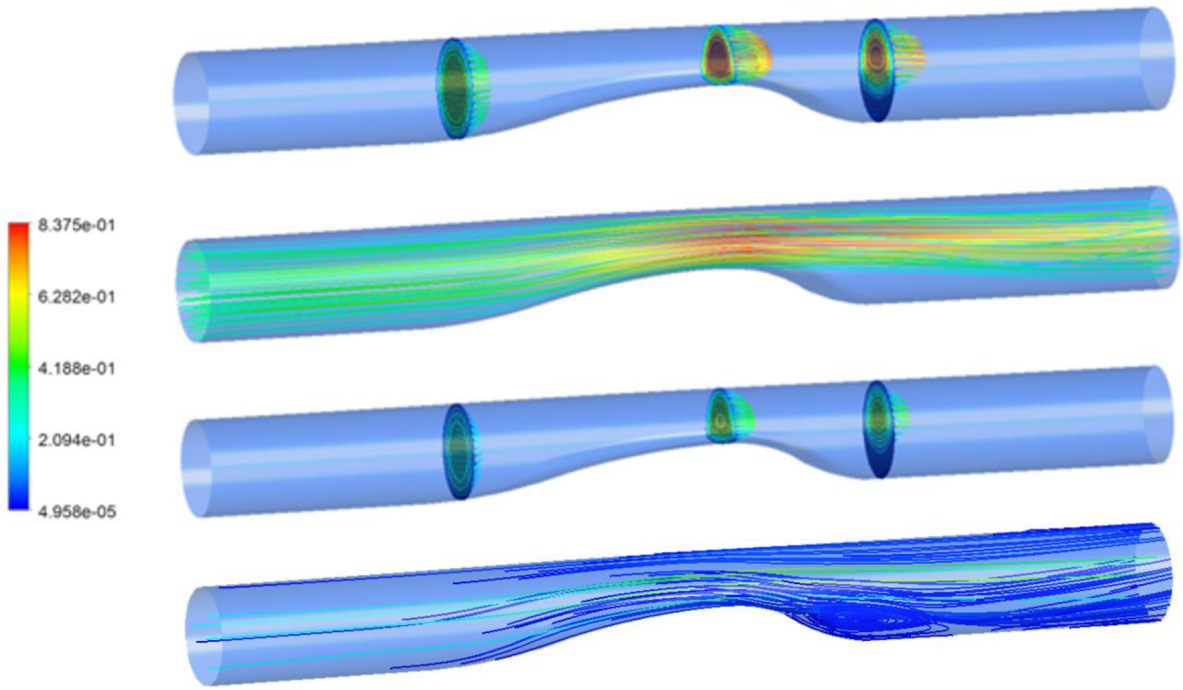

Figure 60 - Velocity vector profiles for three plane cuts – before, in, and after an atherosclerotic plaque, with corresponding velocity streamlines. From top to bottom: systolic phase (first two), diastolic phase (last two). Results are in [m/s].

3.5 Model Parametrization

Due to complexity of the analysis chosen for this thesis, only 2 additional models are created. The parameter chosen for alteration is the maximum lipid core thickness (and corresponding stenosis percentage), with all the remaining parameters, mentioned in subchapter 3.1.1, remaining the same. Different cases are displayed in Table 9.

Table 9 - Model parametrization

Case	Max. lipid core thickness $[mm]$	Stenosis $[\%]$
1 (referential)	2.3	50
2	1.3	30
3	2.8	60

The process for both cases is analogical to the referential. Mesh, boundary conditions, and analysis setups are aiming to be as close to the referential model as possible, so that all three cases are comparable. Due to the model complexity, however, several changes have to made in order to converge both parametric cases. Since hyperelastic materials are rather compliant, mesh density has to be slightly altered for the structural analysis to converge. Global mesh parameters are, nevertheless, mostly the same to those mentioned in subchapters 3.1.4 and 3.2.5. Resulting mesh count for all cases is displayed in Table 10.

Table 10 - Number of elements for all cases

Case	Structural mesh count	Fluid mesh count
1	≈55 000	≈85 000
2	≈65 000	≈85 000
3	≈70 000	≈70 000

Another difference is in boundary conditions present in the fluid flow analysis. Although we are still calculating two cardiac cycles (see Figure 40), adjustments have to be made in the first second of the *Mass Flow* boundary condition. As mentioned in subchapter 3.2.3, the first second of this boundary condition is primarily used to achieve convergence in the initial time steps and its starting value is highly case-specific. After several iterations, the following starting values were obtained for Case 2, respectively Case 3: $\dot{m} = 0.0206kg/s$ and $\dot{m} = 0.0106kg/s$. Pressure boundary condition remains the same as in Case 1. Both adjusted boundary conditions are displayed in Figure 61.

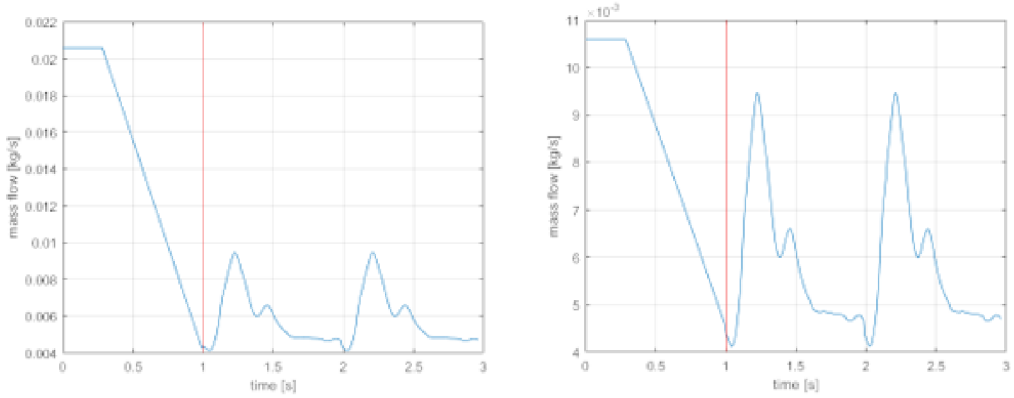

Figure 61 - Mass flow boundary condition. From left to right: Case 2, Case 3.

3.5.1 Comparison of Cases

This subchapter compares the resulting values of maximum principal stress, total deformation, TAWSS, and OSI for all three calculated cases. Though all analysis types (structural/fluid, one-way FSI, and fully coupled FSI analysis) were calculated, only the comparison of a fully coupled analysis is included, as it is the most realistic one and used as referential in this thesis.

3.5.1.1 Maximum Principal Stress and Total Deformation

Maximum principal stress obtained for all calculated cases are displayed in Figure 62 with the corresponding values shown in Table 11.

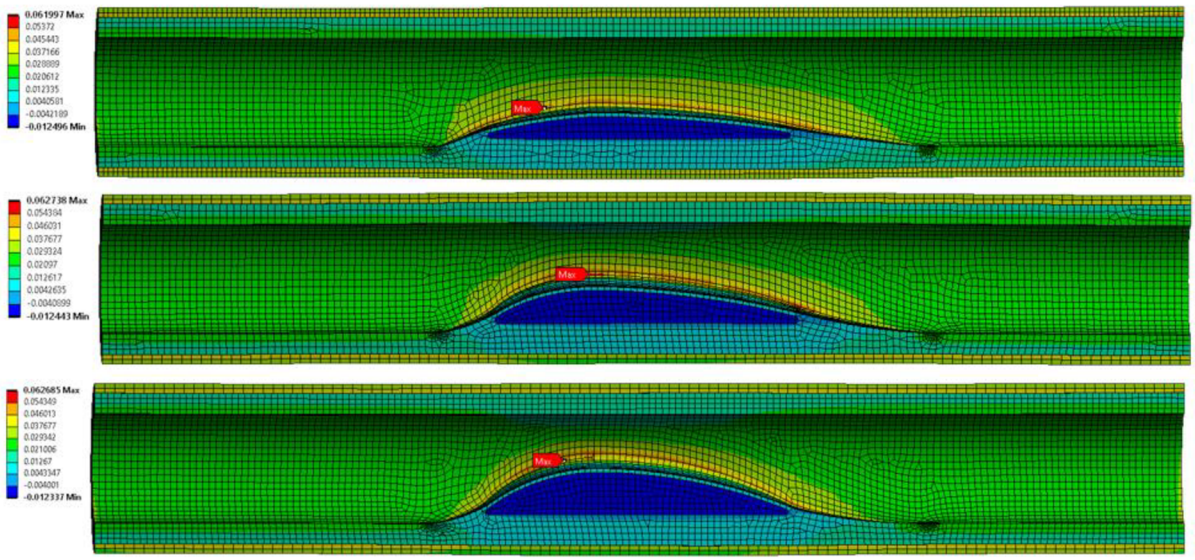

Figure 62 - Maximum principal stress from a fully coupled FSI analysis. From top to bottom: 30%, 50%, 60% stenosis. Results are in [MPa].

Table 11 - Maximum principal stresses for all cases

Stenosis	Maximum principal stress $[kPa]$	Difference $[\%]$
30%	62.00	- 1.3
50%	62.74	0.1
60%	62.69	-

We can see that the results obtained from all three calculated cases are close to identical, with the critical stress locations slightly varying, meaning that the stenosis percentage should play almost no role in maximal generated stresses, contradicting previous research in this area, for example [57]. We could assume that as the atherosclerotic plaque grows, the entire plaque geometry changes correspondingly (for example the fibrous cap radius). As the model in this thesis is already highly idealized and the only parameter altered is the maximum lipid core height (and corresponding stenosis percentage), we can assume that one of the reasons for this result set and the accompanying conclusions is precisely this oversimplification. Also, although a couple of mesh densities were compared, it was only for one case and in a certain range; refining mesh even more could improve these results, but would pose a significant increase in the computational power needed to perform FSI analyses, making it unfeasible for the computer available. Overall, to properly evaluate the impact of a growing atherosclerotic plaque on the generated stresses, further calculations and what-if analyses would have to be performed.

Figure 63 contains the resulting total deformation for all three analyzed cases, with specific values displayed in Table 12.

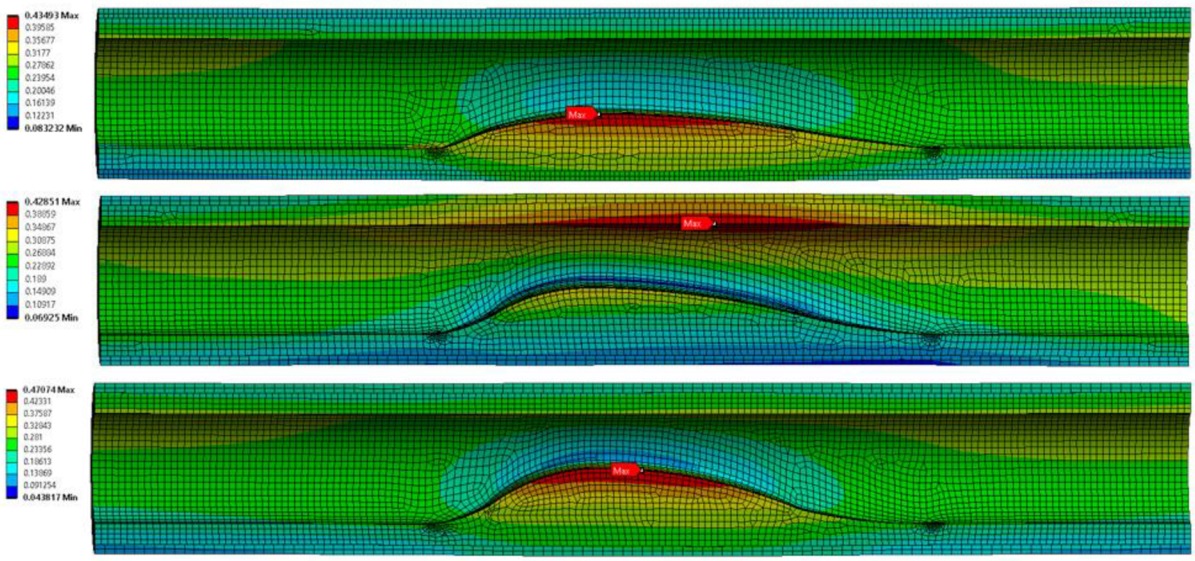

Figure 63 - Total deformation from a fully coupled FSI analysis. From top to bottom: 30%, 50%, 60% stenosis. Results are in [mm].

Table 12 - Total deformation for all cases

Stenosis	Maximum deformation $[mm]$	Difference $[\%]$
30%	0.435	- 7.45
50%	0.429	- 8.73
60%	0.47	-

Similarly to maximum principal stress, all three cases resulted in conformable deformation values. The only difference is that in case of a 50% stenosis, maximal deformation did not occur in the lipid core, rather than in the artery wall, located approximately in the same area. Though we would expect all cases to have maximum deformation in nearly the same location (in the lipid core, as it is the most pliant), this characteristic appears to be case-specific. Once again, more similar analyses would have to be performed to validate this result, but are not a part of this thesis, due to high time consumption.

3.5.1.2 Time-Averaged Wall Shear Stress and Oscillatory Index

As stated earlier, both TAWSS and OSI are some of the main indicators of atherosclerotic plaque growth, and are the most common characteristics evaluated in this area of interest. This is why a comparison of these characteristics for all calculated cases in range up to $0.4\ Pa$ for TAWSS and in range up to 0.5 for OSI is included, see Figure 64 and Figure 65.

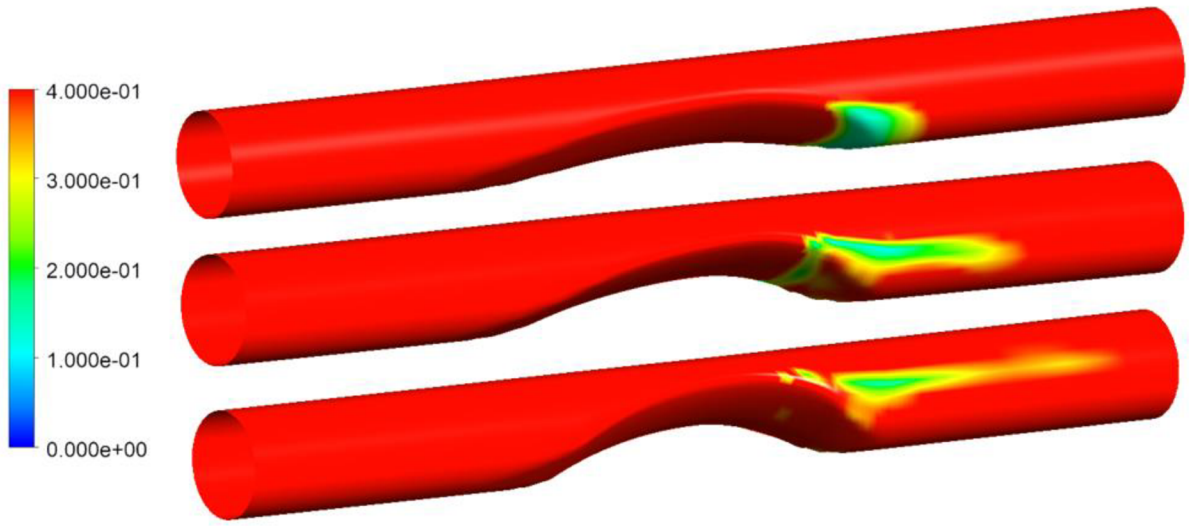

Figure 64 - TAWSS from a fully coupled FSI analysis. From top to bottom: 30%, 50%, 60% stenosis. Results are in [Pa].

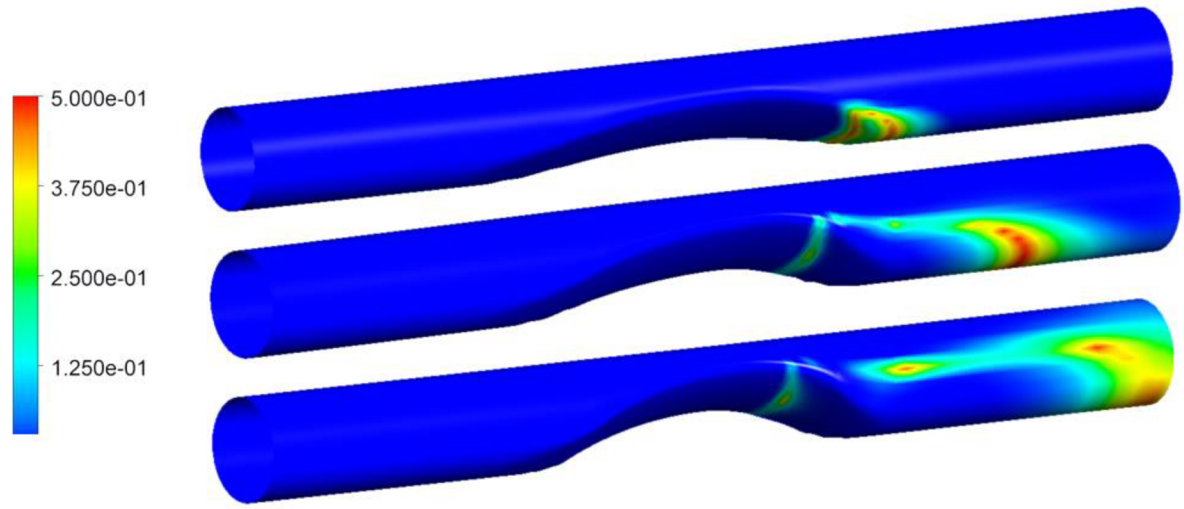

Figure 65 - OSI from a fully coupled FSI analysis. From top to bottom: 30%, 50%, 60% stenosis. Results are in [-].

Results displayed above show that both, low TAWSS values and values close to 0.5 for OSI, are always located after the atherosclerotic plaque, and that both characteristics always have some resemblance within one calculated case. As far as OSI is concerned, the bigger the plaque is, the further from it can high OSI values be seen. This relates to the fact that larger narrowing of the artery results in increased velocity of blood flow further from the plaque. Figure 60 displays vortexes which are forming after the plaque and are common during the diastolic cardiac phase; this phenomenon is also likely related to higher OSI regions. We can also see that in case of a 60% stenosis, highest OSI values are present nearly at the end of the model (*OUTLET* part) which suggests that an increase in length of this after-plaque region would be suitable to properly evaluate the development of this characteristic.

3.6 Computational Times and Used Software

This chapter gives a brief overview of how computationally demanding the analyses performed in this thesis are (processor and RAM memory are the two crucial PC components). FSI analyses are generally highly computationally demanding, even more with all the nonlinearities presented in this thesis. Therefore, two different computers were consequently used for calculations, as the first one provided was only sufficient for structural, fluid, and one-way FSI analysis, and failed when calculating fully coupled FSI analysis. Values in table Table 13, solved on a second computer, are highlighted with a star symbol. The parameters of used computers then were:

- AMD Ryzen 5100X Quad-Core Processor (3.50GHz), 16 GB RAM, NVIDIA GeForce GTX 1050 Ti
- Intel Core i7-5820 Six-Core Processor (3.30GHz), 64 GB RAM, NVIDIA GeForce GTX 260

Below is a table of the computational times needed to perform discussed analyses.

Table 13 - Computation times for all analyses

	Computational time $[h]$		
Analysis Type	Case 1	Case 2	Case 3
Structural Analysis	1.5	1.5	2
Fluid Analysis	1	1	1.5
One-way FSI Analysis	125	130	150
Fully coupled FSI Analysis	70*	80*	105*

Below is also listed all the software used for this thesis:

- *Ansys* – FEM software, used for all simulations in this thesis
- *Matlab* – programming platform designed for engineering purposes, used for the calculations of TAWSS and OSI
- *Excel* – data analysis software, used for data extraction regarding TAWSS and OSI
- *Word* – word processor, used for the text of this thesis
- *Photoshop* – raster graphics editor developed by Adobe Inc., used for image processing

3.7 Discussion

This chapter discusses the results obtained in this thesis, their limitations, and possible improvements for further research in this area.

Firstly, a model of artery with an atherosclerotic plaque is created, following the dimensions from literature, along with a corresponding model of blood. Solid is modelled as isotropic and incompressible, using the Yeoh constitutive model, and blood is modelled as a non-Newtonian, incompressible fluid, using the Carreau-Yasuda model. All material data are taken from literature. Artery is allowed to move only radially, using a cylindrical coordinate system, and assigning both ends with a displacement boundary condition. Boundary conditions of blood are a pressure waveform on inlet, and a mass flow waveform on outlet, with the data taken from literature; both fluid model ends are assigned with two consecutive cardiac cycles (200 time steps in 2 seconds). Values in the first second of both boundary conditions are assigned manually to help with initial convergence problems during an FSI analysis. Models are initially separately subject to a structural (with static pressure applied on the inner wall), respectively fluid analysis, to achieve convergence, prior to entering a coupled FSI analysis. Result independence on mesh is checked on both models for three different cases and the best suitable mesh density is used.

A part of this thesis focuses on the comparison of a structural/fluid analysis and one-way FSI analysis to a more computationally demanding fully coupled FSI analysis. The characteristics of interest are maximum principal stress on the artery wall, total deformation of the artery wall, time-averaged wall shear stress, and oscillatory index. When analyzing maximum principal stress, we see that structural analysis overestimates the value obtained by a fully coupled FSI analysis by 15.5%, whereas one-way FSI analysis underestimates it by 6.2%. This shows that the pulsatile nature of blood flow has a significant influence on the stresses generated on the artery wall. Though differences in total deformation are not as substantial (6.9%, respectively 2.3%), locations of maximal deformation can also vary for different analysis types. When comparing TAWSS and OSI, both fluid and one-way FSI analysis show the same results, which are significantly different compared to the ones obtained from a fully coupled FSI analysis. This shows that the deformation of artery wall and consequent deformation of blood both play a vital role in what the resulting critical areas look like.

Another part deals with model parametrization, as for one, the geometry of an atherosclerotic plaque evolves over time, and is highly patient-specific. Due to high complexity of FSI analyses, only three cases are dealt with in this thesis, and the only altered parameter is maximum thickness of the lipid core. All analyzed cases are only compared for a fully coupled FSI analysis, as it is the most complex analysis type used in this thesis. Comparison of maximum principal stress on the artery wall shows no significant difference in value and only a slight difference in critical location, contradicting previous research in this area. As the atherosclerotic plaque grows, maximum thickness of the lipid core is most likely not the only parameter that is changing during this process, which is why several other parameters should be included in this parametrization to properly assess the impact of plaque growth on the generated stresses. Also, even though a result independence on mesh is checked in this thesis, the final mesh could further be refined to find expected differences. However, every slight refinement of the mesh adds to the time needed to perform coupled analyses, thus making it highly time consuming to perform more precise simulations. Two out of the three analyzed cases show highest deformation in the lipid core region, as it is the most compliant part of the artery. One of the cases, however, shows highest deformations deformation in the artery wall, approximately in the narrowest section of the artery model. This suggests that the geometry also has an impact on how deformations

are distributed. In case of TAWSS and OSI, all cases display critical locations right after the atherosclerotic plaque, making this area the most critical for further plaque growth. As the stenosis percentage increases, highest OSI values are present further downstream from the plaque, as a result of greater blood vortexes forming after the plaque and higher blood velocity further from the plaque. Slight increase of the artery length in this region would be suitable, as highest OSI values for a 60% stenosis are already located at the very end of the model, making them possibly affected by boundary conditions.

The approach used in this thesis has numerous limitations. Firstly, we are working with idealized geometry, rather than with patient-specific models. Although all dimensions are based on literature, real arteries and atherosclerotic plaques are not symmetrical and uniform, meaning that the results ought to vary for more realistic geometries. The material model used in this thesis is isotropic and incompressible. Several papers, discussed in this thesis, model the media layer as anisotropic, since it contains the most collagen and elastin fibers in different orientations, which are primarily responsible for the mechanical properties of arteria. This thesis neglects this anizotropic behavior. Also, material data vary across different sources and are often presented in a certain range, depending for example on the level of calcification in the lipid core. This thesis uses only one set of these data with the specific values being chosen mostly in a way so that we would achieve convergence. We can therefore expect adjustments in this area to have an impact on the overall artery behavior. Another limitation is the number of cardiac cycles used as boundary conditions for the FSI analysis. Although the difference of maximum principal stresses between the two cycles used is only 1.46%, we cannot be sure that increasing this number would not alter the results in a different manner, for example regarding TAWSS or OSI. Another limitation to be considered is the nature of FSI analyses themselves. Working with FSI analysis data files is generally difficult, since for one, they take several days to finish, and they also take up a lot of space; the total allocated memory for storing the data for this thesis exceeded 300GB, making it highly time consuming to transfer and post process the results. This is why more analyzed cases are not introduced in this thesis.

All the aforementioned limitations serve as a guideline for future improvements of this model. This thesis merely gives an idea of how complex such simulations are, how much can certain analyses be simplified to obtain representative results, and what are the impacts of altering a specific parameter in the geometry.

Conclusion

The purpose of this thesis was to simulate the interaction of a pulsatory blood flow with a flexible artery tube containing an atherosclerotic plaque. This research area bears great importance, as if we can realistically simulate all the processes related to atherosclerosis and other cardiovascular diseases, we can successfully predict these conditions and most likely even prevent them.

In the first chapter, a research study is conducted, consisting of an introduction to the cardiovascular system, blood vessels, associated diseases, and constitutive modelling of biological tissues, blood, its rheology, and function within the body, classification of fluids, and a brief introduction to fluid flow theory. Then, an overview of the current state of computational modelling of atherosclerotic arteria is presented, focused on FSI analyses of the carotid artery. Experimental part focuses on the creation of a simplified model of the internal carotid artery containing an atherosclerotic plaque and a corresponding model of blood. Artery is modelled as isotropic and incompressible, using the Yeoh model. Blood is modelled as a non-Newtonian, incompressible fluid, using the Carreau-Yasuda formulation. Both of these models are then subject to several analysis types, starting from a structural/fluid analysis, proceeding to one-way FSI analysis, and finally to a fully coupled FSI analysis, which considers both, pulsatory nature of blood flow and hyperelastic behavior of the artery wall. Model is also later subject to a simplified parametrization with the altered parameter being maximum thickness of the lipid core and the corresponding stenosis percentage.

Results show that structural analysis with constant applied pressure overestimates the results obtained from a fully coupled FSI analysis, whereas one-way FSI analysis underestimate these results, which suggests that pulsatory nature of blood flow has to be accounted for when comparing resulting stresses on the artery wall. Critical TAWSS and OSI locations are for all cases located right after the atherosclerotic plaque and correspond with expected behavior. Critical areas, however, differ for a fully coupled FSI analysis compared to the rest. This suggests that only a fully coupled FSI analysis can properly predict these locations. Increase in stenosis percentage shows no significant difference in generated maximum principal stresses on the artery wall, which can primarily be explained by an excessive simplification of the model. This increase, however, results in differences in TAWSS and OSI.

This thesis gives an introduction to how such analyses can be performed, what are the limitations of the models used, and how can the models be improved in the future. FSI analyses are generally highly computationally demanding, but as the computational power available increases, we will gradually be able to perform more complex simulations and thus more realistic predictions.

References

[1] P. Janíček, Systémová metodologie: brána do řešení problémů, Brno: Akademické nakladatelství CERM, 2014.

[2] M. P. M. Wayne W. LaMorte, "Cardiovascular system," 8 October 2016. [Online]. Available: https://sphweb.bumc.bu.edu/otlt/mph-modules/ph/ph709_heart/ph709_heart2.html.

[3] P. D. H. Feneis, Anatomický obrazový slovník, Praha: Avicenum, 1981.

[4] D. F. prof. MUDr. Miloš Štejfa, Kardiologie, 3. přepracované vydání, Praha: GRADA, 2007.

[5] M. J. H. Doc. MUDr. Martin Vokurka, Velký lékařský slovník, 8. aktualizované vydání, Praha: MAXDORF, 2008.

[6] H. Staff, „Electrical System of the Heart," University of Michigan, [Online]. Available: https://www.uofmhealth.org/health-library/te7147abc.

[7] -, „Anatomy and Physiology," California State University, 2020. [Online]. Available: https://med.libretexts.org/Bookshelves/Anatomy_and_Physiology/Book%3A_Anatomy_and_Physiology_(Boundless).

[8] J. D. H. C. A. Taylor, „Open problems in computational vascular biomechanics: Hemodynamics and arterial wall mechanics. Computer Methods in Applied Mechanics and Engineering," sv. 198, č. 45, 15 02 2009.

[9] R. D. M. G. R. Čihák, Anatomie 3, Praha: Grada Publishing, 2004.

[10] J. H. M. F. O'Rourke, „Mechanical Factors in Arterial Aging. A Clinical Perspective," sv. 50, č. 01, 2007.

[11] J. Burša, „Biomechanika srdečně-cévní soustavy," [Online]. Available: http://www.umt.fme.vutbr.cz/cs/studium/studijni-materialy.html. [Přístup získán 03 03 2021].

[12] e. a. Lucie Bacakova, „The Role of Vascular Smooth Muscle Cells in the Physiology and Pathophysiology of Blood Vessels," v *Muscle Cell and Tissue*, Tokyo Institute of Technology, -, 2018.

[13] e. a. Mary K. O'Connell, „The three-dimensional micro- and nanostructure of the aortic medial lamellar unit measured using 3D confocal and electron microscopy imaging," 2008. [Online]. Available: https://doi.org/10.1016/j.matbio.2007.10.008. [Přístup získán 03 03 2021].

[14] A. A. Mark Buttin, „Age-related changes in the mechanical properties of arteries," v *Mechanical Properties of Aging Soft Tissues (pp.37-74)*, Springer, 2015.

[15] M. F. James Beckerman, „Picture of the Carotid Artery," 17 05 2019. [Online]. Available: https://www.webmd.com/heart/picture-of-the-carotid-artery. [Přístup získán 05 03 2021].

[16] -, „The crucial, controversial carotid artery Part 1: The artery in health and disease,“ Harvard Medical School, 08 2011. [Online]. Available: https://www.health.harvard.edu/heart-health/the-crucial-controversial-carotid-artery-part-i-the-artery-in-health-and-disease. [Přístup získán 03 05 2021].

[17] M. Suzanne R. Steinbaum, „Vascular diseases,“ 21 10 2019. [Online]. Available: https://www.webmd.com/heart-disease/vascular-disease. [Přístup získán 50 03 2021].

[18] e. a. Sourabh Aggarwal, „Abdominal aortic aneurysm: A comprehensive review,“ *Clinical Cardiology: Review,* 2011.

[19] e. a. Setor K. Kunutsor, „Physical activity and risk of venous thromboembolism: systematic review and meta-analysis of prospective cohort studies,“ sv. 35, č. 5, 05 2020.

[20] e. a. Karon Abe, „Venous thromboembolism as a cause of severe maternal morbidity and mortality in the United States,“ 09 03 2019. [Online]. Available: https://pubmed.ncbi.nlm.nih.gov/30935751/. [Přístup získán 06 03 2021].

[21] e. a. Myeong-Ja-Yun, „A Study on Prevalence and Risk Factors for Varicose Veins in Nurses at a University Hospital,“ sv. 9, č. 1, 03 2018.

[22] e. a. Kshitij Arun Manerikar, „A study of etiology of secondary varicose veins,“ 09 2018. [Online]. Available: https://www.researchgate.net/publication/322179209_A_study_of_etiology_of_secondary_varicose_veins. [Přístup získán 06 03 2021].

[23] e. a. Joel Rodriguez-Saldana, „A Pathological Study of the Epidemiology of Atherosclerosis in Mexico City,“ Sv. %1 z %2-, č. -, 26 02 2014.

[24] A. J. Lusis, „Atherosclerosis,“ National Institutes of Health, 14 09 2000. [Online]. Available: https://www.ncbi.nlm.nih.gov/pmc/articles/PMC2826222/. [Přístup získán 06 03 2021].

[25] M. C. B. J. W. J. S. C. Bergheanu, „Pathophysiology and treatment of atherosclerosis,“ National Institutes of Health, 04 2017. [Online]. Available: https://www.ncbi.nlm.nih.gov/pmc/articles/PMC5355390/. [Přístup získán 06 03 2021].

[26] e. a. Mahmoud Rafieian-Kopaei, „Atherosclerosis: Process, Indicators, Risk Factors and New Hopes,“ sv. 5, č. 8, 08 2014.

[27] M. V. R. Č. e. a. Tomáš Fait, Preventivní Medicína, Praha: Maxdorf, 2008.

[28] J. P. Jiří Burša, „Nelineární problémy mechaniky těles,“ [Online]. Available: http://www.umt.fme.vutbr.cz/cs/studium/studijni-materialy.html. [Přístup získán 11 03 2021].

[29] e. a. Jiří Burša, „Výpočtové modely materiálů - skripta určená pro předmět Konstitutivní vztahy materiálů,“ 2019. [Online]. Available: http://www.umt.fme.vutbr.cz/cs/studium/studijni-materialy.html. [Přístup získán 14 03 2021].

[30] J. B. Kamil Novák, „Constitutive model Neo-Hooke - basic formulations and applications,“ Brno University of Technology, 2019. [Online]. Available: http://www.umt.fme.vutbr.cz/cs/studium/studijni-materialy.html. [Přístup získán 14 03 2021].

[31] M. Arumugam, „Formula for converting mmHg to kPa as the unit for measurement of pressure when using newer tourniquet machines that measure pressure using the SI,“ sv. 13, č. 4, 11 2009.

[32] e. a. S. Z. Zhao, „Blood flow and vessel mechanics in a physiologically realistic model of a human carotid arterial bifurcation,“ č. 33, 2000.

[33] J. F. R. R. P. Chhabra, Non-Newtonian Flow and Applied Rheology: Engineering Applications (2. edition), 2008.

[34] F. Š. V. J. Ondřej Debreczeni, Hydromechanika - Výuková opora předmětu Hydromechanika, Brno: Brno University of Technology, 2003.

[35] T. Sochi, „Non-Newtonian Rheology in Blood Circulation,“ 2013. [Online]. Available: https://www.researchgate.net/publication/237082570_Non-Newtonian_Rheology_in_Blood_Circulation. [Přístup získán 19 03 2021].

[36] D. Schwarz, Analysis of Effect of Bifurcation Geometry on Wall Stress in Human Aorta - FSI, Ostrava: VSB - Technical University of Ostrava, 2020.

[37] F. B. M. Capurro, „Evaluating the mechanical properties of biomaterials (p. 270-323),“ v *Biomaterials for Bone Regeneration*, 2014.

[38] J. Kohút, Comparison of Pulasting Flow of Newtonian and non-Newtonian Fluid in Complex Geometry, Brno: Brno University of Technology, 2020.

[39] G. B. Thurston, „The elastic yield stress of human blood,“ National Center for Biotechnology Information, 1993. [Online]. Available: https://pubmed.ncbi.nlm.nih.gov/8329640/. [Přístup získán 19 03 2021].

[40] M. Coufalík, Vortex pump as a possible heart replacement, Brno: Energy Institute, Brno University of Technology, 2017.

[41] T. Sochi, „Modelling the Flow of Yield-Stress Fluids in Porous Media,“ sv. 85, č. 2, 2010.

[42] e. a. Rashid Mahmood, „A comprehensive finite element examination of Carreau Yasuda fluid model in a lid driven cavity and channel with obstacle by way of kinetic energy and drag and lift coefficient measurements,“ sv. 9, č. 2, 2020.

[43] M. Ö. C. Emrah Özahl, „A Brief Overview on Laminar to Turbulent Transition in Time-Dependent Pipe Flows,“ Gaziantep, 2008.

[44] D.-G. Paeng, „Cyclic and radial variation of ultrasonic backscatter from flowing porcine blood,“ Jeju National University, 02 2002. [Online]. Available:

https://www.researchgate.net/publication/234542625_Cyclic_and_radial_variation_of_ultrasonic_backscatter_from_flowing_porcine_blood. [Přístup získán 21 03 2021].

[45] J. R. Womersley, „Method for the calculation of velocity, rate of flow and viscous drag in arteries when the pressure gradient is known,“ sv. 127, č. 3, 28 03 1955.

[46] Z. T. e. a. Yuan Huang, „The influence of computational strategy on prediction of mechanical stress in carotid atherosclerotic plaques: Comparison of 2D structure-only, 3D structure-only, one-way and fully coupled fluid-structure interaction analyses,“ sv. 47, č. 6 (p. 1465-1471), 2014.

[47] e. a. Jianmin Yuan, „Influence of material property variability on the mechanical behaviour of carotid atherosclerotic plaques: A 3D fluid-structure interaction analysis: Material Property Variability and Plaque Mechanical Behaviours,“ 2015.

[48] e. a. César Alegre-Martínez, „On the axial distribution of plaque stress: Influence of stenosis severity, lipid core stiffness, lipid core length and fibrous cap stiffness,“ 2019.

[49] e. a. Danny Bluestein, „Influence of microcalcifications on vulnerable plaque mechanics using FSI modeling,“ sv. 41, 2008.

[50] e. a. H. Gao, „ Stress analysis of carotid atheroma in a transient ischaemic attack patient using the MRI-based fluid-structure interaction method,“ sv. 82, č. Special Issue, 2009.

[51] Q. L. Hao Gao, „Effects of varied lipid core volume and fibrous cap thickness on stress distribution in carotid arterial plaques,“ sv. 41, č. 14, 2008.

[52] e. a. Hao Gao, „Carotid arterial plaque stress analysis using fluid-structure interactive simulation based on in-vivo magnetic resonance images of four pacients,“ sv. 42, č. 10, 2009.

[53] e. a. Joseph R. Leach, „Carotid Atheroma Rupture Observed In Vivo and FSI-Predicted Stress Distribution Based on Pre-rupture Imaging,“ sv. 38, č. 8, 2010.

[54] e. a. Ondřej Lisický, „Consideration of stiffness of wall layers is decisive for patient-specific analysis of carotid artery with atheroma,“ sv. 15, č. 9, 2020.

[55] e. a. Daniel H. O'Leary, „Carotid Artery Intima and Media Thickness as a Risk Factor for Myocardial Infarction and Stroke in Older Adults,“ sv. 340, č. 1, 1999.

[56] e. a. Jaroslaw Krejza, „Carotid Artery Diameter in Men and Women and the Relation to Body and Neck Size,“ sv. 37, č. 4, 2006.

[57] e. a. Stanislav Polzer, „Moderate thickness of lipid core in shoulder region of atherosclerotic plaque determines vulnerable plaque - A parametric study,“ sv. 69, 2019.

[58] e. a. Gerhard Sommer, „Biaxial mechanical properties of intact and layer-dissected human carotid arteries at physiological and supraphysiological loadings,“ *Am J Physiol Heart Circ Physiol,* sv. 298, č. 3, 2010.

[59] G. A. H. Gerhard Sommer, „3D constitutive modeling of the biaxial mechanical response of intact and layer-dissected human carotid arteries,“ *J Mech Behav Biomed Mater,* sv. 5, č. 1, 2012.

[60] -, „Ansys v19.3 Documentation,“ Ansys Inc., 2019. [Online]. Available: https://www.ansys.com/. [Přístup získán 01 04 2021].

[61] -, „Web Plot Digitizer,“ Ankit Rohatgi, 28 11 2020. [Online]. Available: https://automeris.io/WebPlotDigitizer/. [Přístup získán 01 03 2021].

[62] A. K. D. P. K. D. V. Kannojiya, „Proposal of hemodynamically improved design of an axial flow blood pump for LVAD,“ sv. 58, č. 2, 2020.

[63] D. Tichoň, „Analysis of Pulse Wave Propagation in Aorta,“ Brno University of Technology, 2020. [Online]. Available: https://www.vutbr.cz/studenti/zav-prace/detail/124910. [Přístup získán 11 04 2021].

[64] e. a. A. M. Malek, „Hemodynamic shear stress and its role in atherosclerosis,“ sv. 282, č. 21, 1999.

[65] e. a. David M. Martin, „Computational fluid dynamics analysis of balloon-expandable coronary stents: Influence of stent and vessel deformation,“ sv. 36, č. 8, 2014.

[66] H. Y. e. a. Zhiyan Chen, „Vascular Remodelling Relates to an Elevated Oscillatory Shear Index and Relative Residence Time in Spontaneously Hypertensive Rats,“ sv. 7, č. 2007, 2017.

[67] T. A. o. t. B. P. Industry, „The heart,“ ABPI, 2012. [Online]. Available: https://www.abpischools.org.uk/topic/heartandcirculation/4.

[68] L. P. C. Hospital, „Anatomy and Function of the Electrical System,“ Stanford, [Online]. Available: https://www.stanfordchildrens.org/en/topic/default?id=anatomy-and-function-of-the-electrical-system-90-P01762.

[69] D. R. Droual, „Cardiovascular System: Vessels and Circulation,“ [Online]. Available: http://droualb.faculty.mjc.edu/Lecture%20Notes/Unit%204/cardiovascular-blood%20vessels%20with%20figures.htm.

[70] O. Lisický, „Effect of Spine on Stresses in Abdominal Aortic Aneurysm,“ Brno University of Technology, 2018. [Online]. Available: https://www.vutbr.cz/studenti/zav-prace/detail/105745. [Přístup získán 11 03 2021].

[71] e. a. Lin Yang, „A Parallel System for Clustering ECG Streams Based on MapReduce,“ The Hong Kong Unviersity fo Science, 12 2013. [Online]. Available: https://www.researchgate.net/publication/269302437_PESC_A_parallel_system_for_clustering_ECG_streams_based_on_MapReduce. [Přístup získán 16 03 2021].

[72] M. Liji Thomas, „Blood Plasma Comopnents and Function,“ [Online]. Available: https://www.news-medical.net/health/Blood-Plasma-Components-and-Function.aspx. [Přístup získán 16 03 2021].

[73] -, „Atherosclerotic plaque,“ Encyclopaedia Britannica, Inc., 2010. [Online]. Available: https://www.britannica.com/science/atherosclerotic-plaque. [Přístup získán 06 03 2021].

[74] -, „Brain Aneurysms,“ [Online]. Available: https://memphisvascular.com/patient-education/brain-aneurysms/. [Přístup získán 05 03 2021].

[75] -, „Laminar vs. Turbulent Flow,“ CFD Support, [Online]. Available: https://www.cfdsupport.com/OpenFOAM-Training-by-CFD-Support/node334.html. [Přístup získán 19 03 2021].

List of Symbols

Symbol	Definition	Unit
$\partial x, \partial y, \partial z$	Elementary deformed elements	$[m]$
$\partial X, \partial Y, \partial Z$	Elementary undeformed elements	$[m]$
$\lambda_{x,y,z}$	Proportionate elongations	$[-]$
F_{ij}	Deformation tensor	$[-]$
J	Third invariant of the deformation tensor	$[-]$
C	Cauchy-Green deformation tensor (right)	$[-]$
I_1	First invariant of the Cauchy-Green deformation tensor	$[-]$
I_2	Second invariant of the Cauchy-Green deformation tensor	$[-]$
I_3	Third invariant of the Cauchy-Green deformation tensor	$[-]$
$\bar{\lambda}_p$	Modified principal elongation	$[-]$
$\bar{I}_{1,2,3}$	Modified invariants of the Cauchy-Green deformation tensor	$[-]$
σ_i	Cauchy stress tensor	$[Pa]$
dF_i	True elementary force	$[N]$
τ_i	I. Piola-Kirchhoff stress tensor	$[Pa]$
dF_{0i}	Elementary force	$[N]$
S_i	II. Piola-Kirchhoff stress tensor	$[Pa]$
W	Strain energy function	$[Pa]$
N	Number of molecule chains in a volume unit	$[-]$
k	Boltzmann's constant	$[J \cdot K^{-1}]$
T	Thermodynamic temperature	$[K]$
G	Shear modulus	$[Pa]$
c_{ij}	Mooney-Rivlin model material parameters	$[Pa]$
λ_L	Limit elongation of a given molecule chain	$[-]$
C_{i0}	Yeoh model material parameters	$[Pa]$
F_t	Tangential force	$[N]$
τ	Shear stress	$[Pa]$
S	Surface	$[m^2]$
$\dot{\gamma}_{yx}$	Shear rate	$[s^{-1}]$
η	Newtonian viscosity	$[Pa \cdot s]$
D_e	Deborah number	$[-]$
λ_r	Relaxation time	$[s]$
λ_c	Characteristic time	$[s]$
E	Young's modulus	$[Pa]$
η_∞	Viscosity in high shear	$[Pa \cdot s]$
η_0	Viscosity in low shear	$[Pa \cdot s]$
λ	Time constant	$[s]$
n	Power law index	$[-]$
a	Exponent	$[-]$
Re	Reynolds number	$[-]$
v_s	Flow speed	$[m \cdot s^{-1}]$
D	Diameter	$[m]$
ρ	Density	$[kg \cdot m^{-3}]$
Q	Volumetric flow	$[kg \cdot s^{-1}]$
ΔP	Pressure change	$[Pa]$
r_i	Radius	$[m]$
l	Length	$[m]$

$Re[\dots]$	Real part of a complex number	$[-]$
i	Imaginary unit	$[-]$
y	Distance from the center	$[m]$
$\Delta P/l$	Pressure gradient	$[Pa \cdot m^{-1}]$
J_0	First kind Bessel function of the order zero	$[-]$
J_1	First kind Bessel function of the order one	$[-]$
ω	Angular velocity	$[rad \cdot s^{-1}]$
α	Womersley parameter	$[-]$
WSS	Wall shear stress	$[Pa]$
$TAWSS$	Time-averaged wall shear stress	$[Pa]$
OSI	Oscillatory shear index	$[-]$
T	Cardiac cycle period	$[-]$
n_i	Surface normal vector	$[-]$
τ_{ij}	Viscous stress tensor	$[Pa]$

List of Abbreviations

Abbreviation	Meaning
CVA	Cerebrovascular accident
SA	Sinoartial node
AV	Atrioventricular node
ECG	Electrocardiography
SMC	Smooth muscle cells
CCA	Common carotid artery
ICA	Internal carotid artery
ECA	External carotid artery
VTE	Venous thromboembolism
DVT	Deep vein thrombosis
PE	Pulmonary embolism
EC	Endothelial cells
LDL-C	Low-density lipoprotein cholesterol
FSI	Fluid-structure interaction
2D	2-dimensional
3D	3-dimensional
TIA	Transient ischaemic attack
WSS	Wall shear stress
MDCTA	Multidetector computed tomography angiography
MRI	Magnetic resonance imaging
WPD	WebPlotDigitizer
FEM	Finite element method
FVM	Finite volume method
CFD	Computational fluid dynamics
TAWSS	Time-averaged wall shear stress
OSI	Oscillatory shear index

List of Figures

List of Tables